The Paton Welding Journal

12
2021

The content of the journal includes articles received from authors from around the world in the field of welding, metallurgy, material science and selectively includes translations into English of articles from the following journals, published by PWI in Ukrainian:
• Automatic Welding (https://patonpublishinghouse.com/eng/journals/as);
• Technical Diagnostics & Nondestructive Testing (https://patonpublishinghouse.com/eng/journals/tdnk);
• Electrometallurgy Today (https://patonpublishinghouse.com/eng/journals/sem).

CONTENTS

ORIGINAL ARTICLES

INFORMATION

*Translated Article(s) from «Automatic Welding», No. 12, 2021.

**Translated Article(s) from «Electrometallurgy Today», No. 3. 2021.

***Translated Article(s) from «Technical Diagnostics & Nondestructive Testing», No. 4, 2021.

INFLUENCE OF A FORCED MODE OF PULSED-ARC WELDING ON THE STRUCTURE AND PROPERTIES OF JOINTS OF STEEL OF THE STRENGTH CLASS C440

A.V. Zavdoveev[1], **V.D. Poznyakov**[1], **M. Rogante**[2], **S.L. Zhdanov**[1], **T.G. Solomiichuk**[1], **O.A. Shyshkevych**[1]

[1]E.O. Paton Electric Welding Institute of the NASU
11 Kazymyr Malevych Str., 03150, Kyiv, Ukraine
[2]Rogante Engineering Office
62012 Civitanova Marche, Italy

ABSTRACT

In the work the influence of a pulsed-arc forced welding on the structure formation and properties of welds and HAZ metal as compared to standard pulsed-arc welding was studied. On the example of a high-strength S460M steel, it was shown that a pulsed-arc forced welding can effectively regulate the structural formation. Change in the welding thermal cycle, namely, accelerated heating and delayed cooling leads to the formation of the optimal structure in the weld and HAZ, which allows obtaining high strength and resistance to brittle fracture. Advantages of a pulsed-arc forced welding allow welding without edge preparation, which significantly improves the efficiency of the process as a whole.

KEY WORDS: pulsed-arc welding, high-strength steel, weld and HAZ metal, thermodeformation cycle, structure, properties of welded joints

INTRODUCTION

In recent years, a continuous increase in the share of welded structures made of steels with enhanced strength is observed. Quality requirements in many industries, such as shipbuilding, civil engineering, hydropower, etc., dictate new rules regarding the development of welding technologies for metal structures while maintaining a high complex of operation properties [1–5]. A simultaneous increase in both mechanical properties as well as ductility can be achieved by adding microalloying elements to steels. The released dispersion carbides and carbonitrides of microalloying elements reduce the grain size either by blocking the migration of austenite grain boundaries or by delaying its recrystallization. As a result, the carbon content can be reduced in microalloyed steels and thus their weldability can be improved, in contrast to the situation with high-strength grades of steel C–Mn.

A further increase in the yield strength of structural steels can be achieved by a special method of rolling, which includes thermomechanical treatment. This requires systematic control of both temperature as well as degree of deformation during metal formation.

Thermomechanical treatment requires fulfilment of the rolling process in such a way that individual stages of steel deformation take place at specified temperatures. Here two main effects are used:

● effect of fine-grained structure on improving mechanical properties and increase in impact strength;

● limitation or delay of recrystallization, which is achieved by introduced microalloying elements (Nb, Ti).

Thermomechanically treated steels with a high level of strength and relatively low carbon equivalent greatly simplify the solution to the problem of improving quality and reliability of metal structures. However, this raises new issues in terms of technologies for welding such steels. Namely, a carbon equivalent alone is no longer enough to study the weldability of thermomechanically treated steels. In the first turn this is predetermined by the peculiarities of the structural state of such steels, which is not taken into account by the carbon equivalent at all. Technical and economic aspects, arising from the possibility of manufacturing products from these steels and their use in energy efficient industries, as well as their suitability for the construction of different structures, including those, operating in extreme climatic conditions, are of great importance for materials science. The problems related to this group of steels require solutions in order to improve the technologies used for the manufacture of metal structures from these steels applying welding methods. One of the promising ways to solve the problems of welding thermomechanically treated steels is the use of pulsed-arc welding (PAW), which allows controlling the modes and welding thermal cycles in a wide range [6–11]. In the previous investigations, the use of PAW to thermomechanically strengthened S460M steel [12] showed the perspective of using this method. However, there is a need to further improvement of the technological process of welding thermomechanically strengthened steels, namely to reduction in the harmful effects of welding thermal cycle on the heat-affected-zone and increase
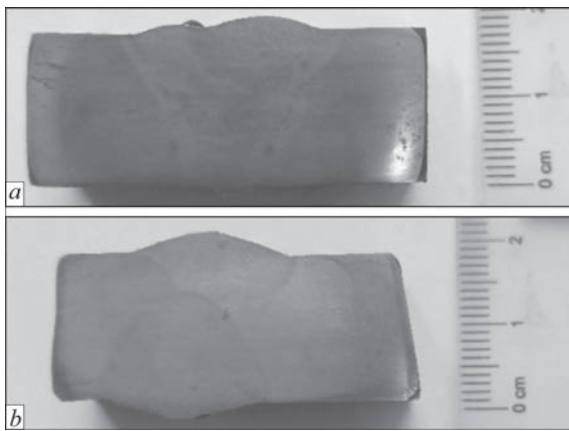
Figure 1. Macrosections of specimens of butt joints made by PAW (*a*) and PAW on a forced mode (*b*)

in the process efficiency. To solve these problems, in the presented work it is proposed to use PAW on a forced mode, which differs significantly from a standard one. Therefore, for the successful use of PAW on a forced mode in the development of modern welding technologies, the study of the influence of the modes of this welding process on the formation of the structure and properties of weld and HAZ metal as compared to stationary arc welding was carried out.

PROCEDURE OF INVESTIGATIONS

In the presented work, thermomechanically strengthened S460M steel [12] (strength class C440) was used, manufactured in accordance with DSTU EN 10025-4:2007. The chemical composition of S460M steel, wt.%: 0.15 C; 0.23 Si; 1.3 Mn; 0.09 Cr; 0.019 Ni; 0.01 V; 0.05 Nb; 0.025 Al; 0.013 S and 0.017 P.

As a power source, the rectifier of inverter type ewm Phoenix Pulse 401 (of MULTIMATRIX Company) was used, which provides different pulse frequency at PAW [12]. To determine the welding and technological characteristics of the current source, a digital oscilloscope UTD2000CEX-II was used, which allows recording the volt-ampere characteristics of the power source in a wide range. To record oscillograms, a shunt 75ShSM with a resistance of

Figure 2. Equipment for record of welding thermal cycles

150 μOhm was used. This allowed recording welding currents of up to 500 A, while the voltage drop on the shunt was 75 mV.

For the basic comparative specimen, as in the previous studies [12], welding in shielding gases (Ar + 18 % CO_2) of S460M steel joints of 16 mm thickness with a V-shaped edge preparation by a solid cross-section wire G3Sil of 1.2 mm diameter was used (Figure 1, *a*). Root passes during welding of this steel were produced on a copper substrate. The mode of automated PAW was as follows: I_m = 220–240 A, U_a = 26–28 V, v_w = 14.21 m/h. In this case, where I_{pls} is the current in the pulse (450 A), I_p is the current in the pause (160 A), t_{pls} and t_p are the duration of the pulse and the pause, respectively. Test specimens using PAW on a forced mode were produced for butt joints without edge preparation: I_m = 320 A, U_a = 28 V, v_w = 8 m/h. It should be noted that in this case a high quality weld formation with a full penetration was provided (Figure 1, *b*), which is impossible in the case of using a traditional welding process.

To study the effect of PAW modes on welding thermal cycles, appropriate experiments were performed. To record WTC, steel plates with a thickness of 10 mm (Figure 2) were used, in which chromel-alumel thermocouples were drilled-in to a depth of 7.5–8.0 mm. This value of the drilling depth is based on the previous studies and is predetermined by the need in recording WTC in the HAZ region.

Metallographic examinations were performed using a scanning electron microscope Mira 3 LMU (Tescan). During the study, the secondary electron detector (designation SE on the electronic image) and the elastically reflected electron detector (designation BSE on the electron image) were used. To evaluate the elemental composition during the study, the detector-spectrometer Oxford X-Max 80 and the analytical software product INCA Energy* were used.

The microhardness of the individual structural components and the integral hardness of the metal were measured in a hardness tester M-400 of the LECO Company at a load of 100 g (*HV*). The specimens for metallographic examinations were prepared according to standard procedures using diamond pastes of a different dispersion, detection of microstructure was performed by chemical etching in a 4 % alcoholic solution of nitric acid.

For mechanical tests of weld and HAZ metal, the standard specimens were manufactured from welded joints. The specimens for static (short-term) tensile tests corresponded to the type II in accordance with GOST 6996–96. According to the results of the carried out tests, the effect of the welding method on the change
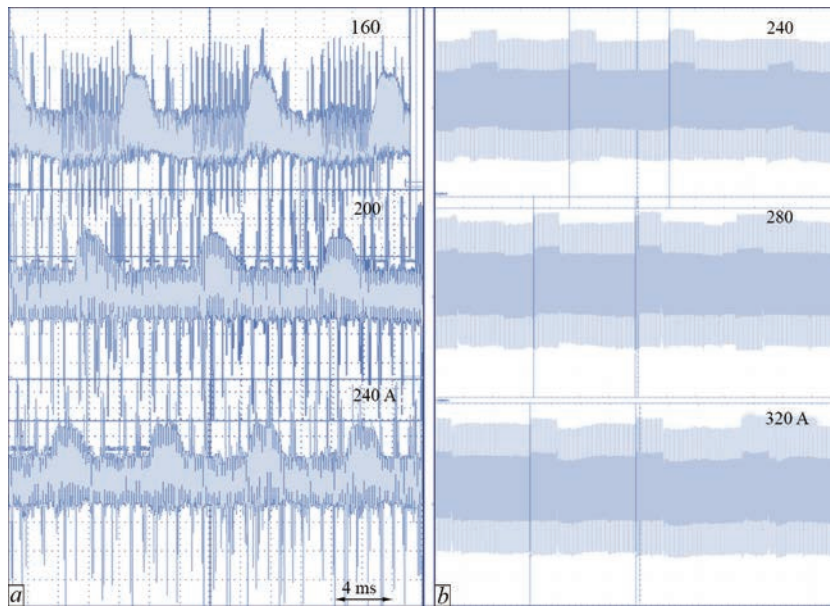
Figure 3. Oscillograms for inverter power source, standard pulsed-arc (*a*) and pulsed-arc forced mode (*b*) of welding

of the following indices of HAZ metal was evaluated: strength (σ_y and σ_t, MPa), ductility (δ_5 i ψ, %).

The ability of the metal to resist brittle fracture was determined using the approaches from fracture mechanics. The values of the criteria K_{1C} and δ_c were determined by standard procedures and formulas given in [12]. To determine the values of the critical stress intensity factor K_{1C} and critical opening of the crack δ_c, the specimens of a rectangular cross-section $10 \times 20 \times 90$ mm with a notch length of 7 mm and a fatigue crack with a length of 3 mm were used. These specimens were tested for three-point bending in the temperature range from 20 to –40 °C.

RESULTS AND THEIR DISCUSSION

INVESTIGATION OF WELDING AND TECHNOLOGICAL CHARACTERISTICS OF PAW

In addition to the normal welding mode, the ewm Phoenix Pulse 501 has a forced PAW mode. Features of this mode were studied, starting from oscillograms of change of welding current depending on time. Figure 3 shows oscillograms for PAW of standard and forced modes. Detailed analysis showed that the pulse repetition frequency corresponds to 58 kHz, and it corresponds to the standard PAW. The forced mode differs in the duty cycle of pulses. If in the standard pulsed-arc mode with a growth in the mean welding current the duty cycle increases, then in the forced mode the duty cycle is unchanged, instead, the parameters of the currents in the pulse and in the pause change. In the pulse the current is constant and equal to 500 A, and the pause current grows with an increase in the mean current. In addition, the shape of the pulse differs significantly, namely, if in PAW on the standard pulsed-arc mode the pulse has a parabolic shape, as was established in [12], then in the case of a forced mode, the shape of the pulse is rectangular. And the effective welding current is equal to the mean welding current, while during PAW in the standard mode, the effective welding current is by 25 % higher (Figure 4).
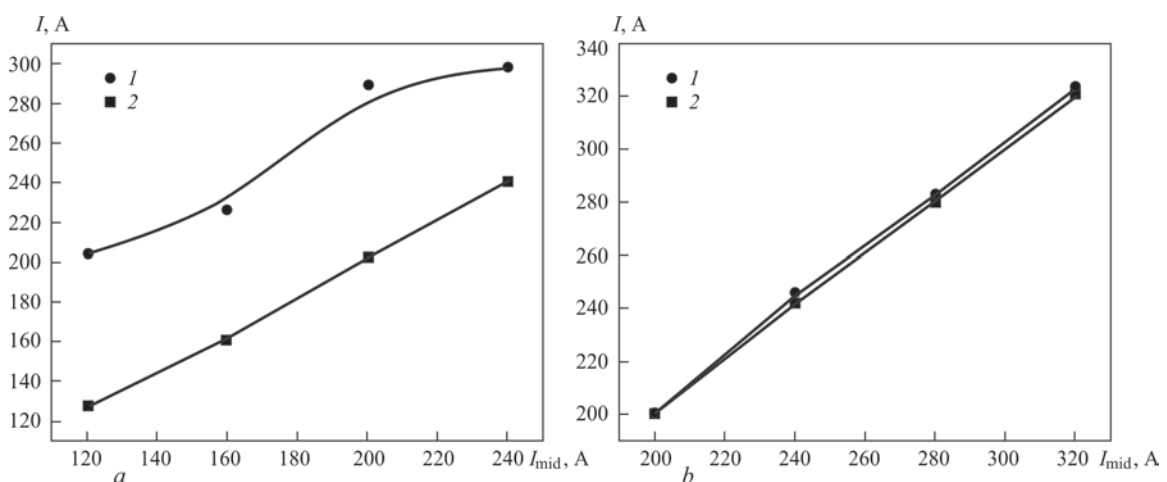
Figure 4. Dependence of effective (*1*) and mean (*2*) welding currents, standard pulsed-arc (*a*) and pulsed-arc forced mode (*b*) of welding
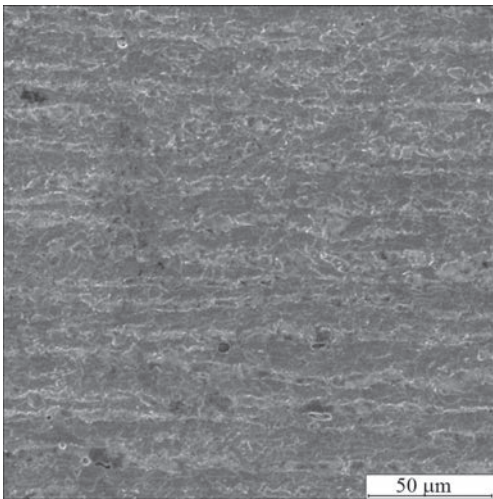
Figure 5. Microstructure of S460M steel

INVESTIGATION OF THE STRUCTURE
AND PROPERTIES OF THE BASE METAL

As a result of performing a controlled thermomechanical rolling in the temperature range of 900–700 °C with an accelerated cooling in the initial structure of S460M steel, a fine-grained banded ferrite-pearlite structure with a grain size of about 20 μm and hardness *HV* 195 is formed (Figure 5).

This structure of S460M steel of the abovementioned chemical composition provides the following level of mechanical properties: yield strength $\sigma_{0.2} = 452$ MPa, tensile strength $\sigma_t = 581$ MPa, elongation $\delta_5 = 26$ %, reduction in area $\psi = 58$ %.

Metallographic examinations of the structure (Figure 6) of welded joints of S460M steel, which were performed in the previous work [12], show that in PAW, the microstructure of the weld metal consists of refined plates of acicular ferrite (1–3 μm) and a reduced amount of polyhedral ferrite (5–10 %) and precipitates of polygonal ferrite (3–10 μm), located along the boundaries of primary austenitic grains. Such changes in the microstructure lead to an increase in hardness in the weld to 2420 MPa as compared to the base metal. In the region of a coarse HAZ grain, a bainite structure with a negligible share (up to 3–5 %) of martensite is observed. The hardness of this region of HAZ increases accordingly to 3250–3340 MPa. The structure of the HAZ region of a refined grain consists of a mixture of upper and lower bainite (2650–2810 MPa). In the region of a partial HAZ recrystallization, pearlite and ferrite are observed, which significantly reduces the Vickers hardness of metal to 2320–2400 MPa.
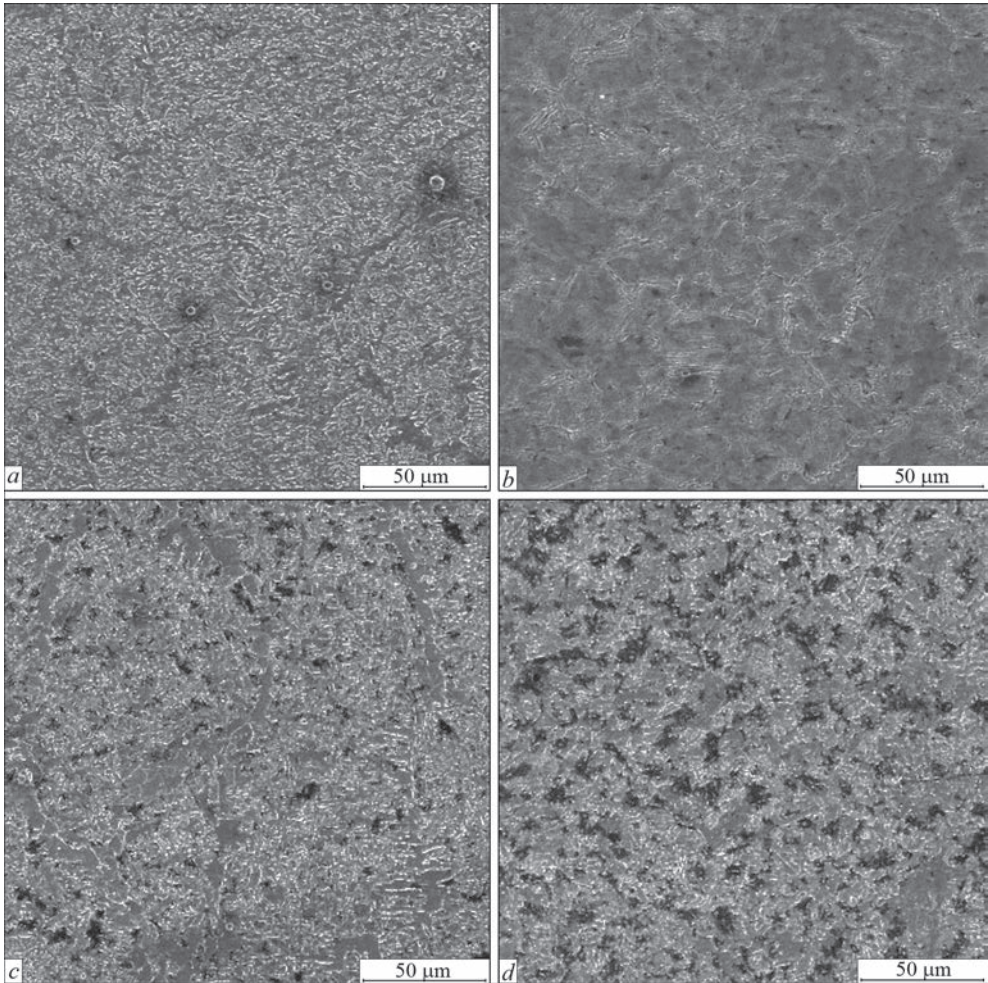
Figure 6. Microstructure of weld (*a*, *c*) and HAZ metal (*b*, *d*) of S460M steel, made by pulsed-arc (*a*, *b*) and pulsed-arc forced (*c*, *d*) welding
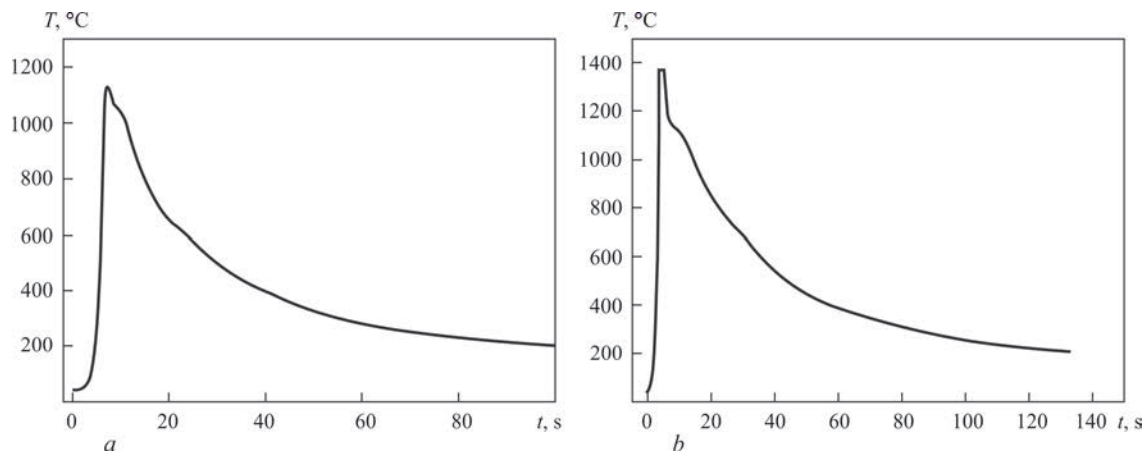
Figure 7. Welding thermal cycles for PAW (*a*) and PAW on a forced mode (*b*)

In PAW on a forced mode, the microstructure of the weld metal differs significantly from the microstructure of the weld metal produced by a standard PAW, namely: acicular ferrite with some larger plates is observed, and precipitates of polygonal ferrite became wider and their specific share increased. As a result, in the metal a decrease in microhardness to 2050 MPa occurs. In the region of a coarse HAZ grain, mainly acicular ferrite with an ordered second phase is observed. The hardness in this region of HAZ, respectively, is equal to 2400–2480 MPa. In the region of a partial recrystallization of HAZ, the formation of pearlite and ferrite is observed, which significantly reduces its hardness to 2160 MPa.

Such differences in the microstructure are predetermined by the peculiarities of WTC running in PAW (Figure 7). Due to the fact that in PAW the temperature of the metal is above 1000 °C, the cooling rate will be much higher, which leads to the formation of a martensitic component in the structure. In PAW the temperature of metal is below 1000 °C, the cooling rate of HAZ metal is lower than that of arc welding, which contributes to the diffusion processes during structural transformations.

In pulsed-arc welding processes, as is noted by the author of [11], WTC plays a key role during hardening of weld metal, as it affects the refinement of structural components by influencing crystallization processes in the welding pool.

The study of hardness (Figure 8) of welded joints revealed that at a forced PAW, its level in the weld metal is lower than 15 % of the hardness of the weld metal produced by a standard PAW. This is predetermined by the peculiarities of the structure formation. In HAZ metal, the hardness values in a pulsed-arc forced welding are also lower than in a standard PAW. This fact is an additional advantage of a forced PAW, as far as in the welded joint a uniform distribution of mechanical properties will be formed. It should be noted that at a forced PAW, the hardness in HAZ decreases to the level of the source metal more slowly.

From the data given in the Table 1 it is seen that under PAW conditions, higher values of strength of the weld metal are achieved as compared to the base metal. Ductility remains at a fairly high level. The values of strength of the weld metal are in a good agreement with the hardness in the weld metal region, namely, they do not exceed the values of the base metal by more than 20 %. When using forced PAW, taking into account that the values of hardness of HAZ metal are not more than 20–25 % from the base metal, it provides the equal strength of the welded joint.

To evaluate the sensitivity of metal regions in welded joints to the concentration of stresses in the conditions of plane deformation under static load, the force criterion is used, which is the critical stress intensity factor K_{1C}. When increasing the values of K_{1C}, the sensitivity of metal to stress concentration decreases. Deformation criteria of fracture are used to determine the crack resistance of fracture materials, which is accompanied by significant plastic deformations in the region near the tip of the crack and precedes its propagation. This criterion is called critical opening of the crack tip δ_c. If the opening of the edges is greater than δ_c, than adhesion stresses are equal to zero. It is used to evaluate the resistance of metal to brittle fracture
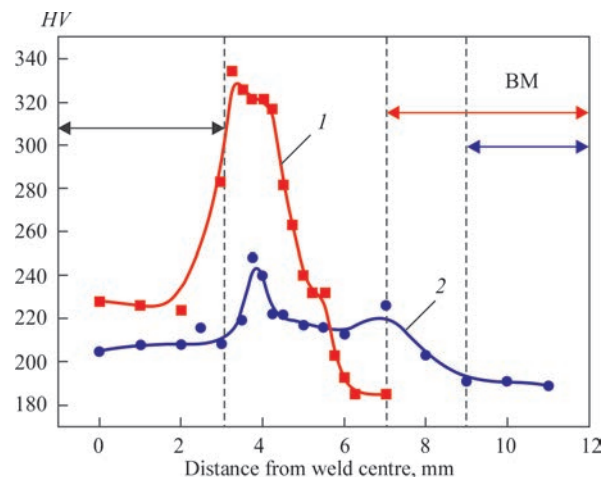
Figure 8. Hardness of welded joints of S460M steel in PAW (*1*) and PAW on a forced mode (*2*)

7

Table 1. Mechanical properties of weld metal of joints of S460M steel in different welding methods

Region	Welding method	σ_y, MPa	σ_t, MPa	δ	ψ
Weld	PAW	570	667	24	68
	PAW on a forced mode	590	675	23	55
BM		452	581	26	60

under the conditions of a large plastic deformation, when the crack at its tip reaches a critical sizes of the value δ_c and begins to propagate rapidly, using the energy released during its further growth. The indices of resistance of HAZ metal of welded joints produced by a standard (K_{1C} = 100 MPa√m, δ_c = 0.11 mm) and a forced (K_{1C} = 100 MPa√m, δ_c = 0.18 mm) PAW to brittle fracture, almost equal and are at a sufficiently high level, which is predetermined by the peculiarities of the structure formation.

CONCLUSIONS

Studies of the effect of standard and forced PAW on the structure and mechanical properties of thermomechanically treated S460M steel allowed finding the following advantages of the latter:

● as compared to the standard PAW, the forced one allows performing welding without edge preparation with producing a high-quality welded joint;

● 30 % lower values of microhardness in the heat-affected-zone of the welded joint as compared to the standard PAW is predetermined by the peculiarities of the welding thermal cycle;

● 15 % lower values of microhardness of weld metal as compared to the standard PAW and close to the values of the base metal, which is provided by the formation of a favourable microstructure;

● high level of resistance to brittle fracture of welded joints.

The mentioned features of a forced pulsed-arc welding allow providing high mechanical properties of welded joints of thermomechanically strengthened S460M steel, which is the main problem for this class of steel. It was demonstrated that the ability to perform forced PAW without edge preparation, in addition, can improve the process efficiency by 40 %.

REFERENCES

1. Lee, C.H., Shin, H.S., Park, K.T. (2012) Evaluation of high strength TMCP steel weld for use in cold regions. *J. Constr. Steel Res.*, **74**, 134–139. DOI: https://doi.org/10.1016/j.jcsr.2012.02.012.

2. Medina, S.F., Gómez, M., Gómez, P.P. (2010) Effects of V and Nb on static recrystallisation of austenite and precipitate size in microalloyed steels. *J. Mater. Sci.*, **45**, 5553–5557. DOI: https://doi.org/10.1007/s10853-010-4616-z.

3. Fossaert, C., Rees, G., Maurickx, T., Bhadeshia, H.K.D.H. (1995) The effect of niobium on the hardenability of microalloyed austenite. *Metall. Mater. Transact. A*,. **26**, 21–30. DOI: https://doi.org/10.1007/BF02669791.

4. Nazarov, A.V., Yakushev, E.V., Shabalov, I.P. et al. (2014) Comparison of weldability of high-strength pipe steels microalloyed with niobium, niobium and vanadium. *Metallurgist*, **7**, 911–917. DOI: https://doi.org/10.1007/s11015-014-9821-6.

5. Zavdoveev, A., Poznyakov, V., Baudin, T. et al. (2021) Welding thermal cycle impact on the microstructure and mechanical properties of thermo-mechanical control process steels. *Steel Research Int.*, 92(**6**), 2000645.

6. Needham, J.C., Carter, A.W. (1965) Material transfer characteristics with pulsed current. *Brit. Weld. J.*, **5**, 229–241.

7. Palani, P.K., Murugan, N. (2006) Selection of parameters of pulsed current gas metal arc welding. *J. of Materials Proc. Technology*, **172**, 1–10.

8. Tong, H., Ueyama, T. et al. (2001) Quality and productivity improvement in aluminium alloy thin sheet welding using alternating current pulsed metal inert gas welding system. *Sci. Technol. Weld. Join.*, 6(**4**), 203–208.

9. Poznyakov, V.D., Zavdoveev, A.V., Gajvoronsky, A.A. et al. (2018) Effect of pulsed-arc welding modes on the parameters of welded joints produced with Sv-08Kh20N9G7T wire. *The Paton Welding J.*, **9**, 7–12.

10. Amin, M., Ahmed, N. (1987) Synergic control in MIG welding 2-power current controllers for steady dc open arc operation. *Met. Construct.*, **6**, 331–340.

11. Rajasekaran, S. (1999) Weld bead characteristics in pulsed GMA welding of Al–Mg alloys. *Weld. J.*, 78 (**12**), 397–407.

12. Zavdoveev, A.V., Poznyakov, V.D., Rogante, M. et al. (2020) Features of structure formation and properties of joints of S460M steel made by pulsed-arc welding. *The Paton Welding J.*, **6**, 9-13. DOI: https://doi.org/10.37434/tpwj2020.06.02

ORCID

A.V. Zavdoveev: 0000-0003-2811-0765,
V.D. Poznyakov: 0000-0001-8581-3526,
M. Rogante: 0000-0002-6846-0826

CONFLICT OF INTEREST

The Authors declare no conflict of interest

CORRESPONDING AUTHOR

V.D. Poznyakov
E.O. Paton Electric Welding Institute of the NASU
11 Kazymyr Malevych Str., 03150, Kyiv, Ukraine
E-mail: paton39@ukr.net

SUGGESTED CITATION

A.V. Zavdoveev, V.D. Poznyakov, M. Rogante, S.L. Zhdanov, T.G. Solomiichuk, O.A. Shyshkevych (2021) Influence of a forced mode of pulsed-arc welding on the structure and properties of joints of steel of the strength class C440. *The Paton Welding J.*, **12**, 3–8.

JOURNAL HOME PAGE

https://pwj.com.ua/en

FEATURES OF LASER-PLASMA WELDING OF CORROSION-RESISTANT STEEL AISI 304 WITH LASER APPLICATION

V.M. Korzhyk[1,2], **V.Yu. Khaskin**[1,2], **A.A. Grynyuk**[2], **E.V. Illyashenko**[2], **A.V. Bernatskyi**[2], **S.I. Peleshenko**[3]

[1]China-Ukraine E.O. Paton Institute of Welding of the Guangdong Academy of Sciences, Guandong Key Laboratory of Advanced Welding Technologies, Guangzhou, China
[2]E.O. Paton Electric Welding Institute of the NASU
11 Kazymyr Malevych Str., 03150, Kyiv, Ukraine
[3]National Technical University of Ukraine «Igor Sikorsky Kyiv Polytechnic Institute»
37 Peremohy Ave., 03056, Kyiv, Ukraine

ABSTRACT

The paper confirms the presence of synergistic effect at laser-plasma welding, using fiber laser, by comparing the cross-sectional areas of penetrations, made in AISI 304 plate (δ = 4 mm) by laser, plasma, and hybrid processes at close power values of laser radiation and plasma arc (~2 kW each). It is determined that the manifestation of this effect depends on welding speed. At the speed of 2 m/min the hybrid penetration cross-sectional area can exceed the sum of areas of penetrations produced with the laser and plasma processes by up to 30 %, and for the speed of 4 m/min by ~20 %. Comparison of input energy of the laser and hybrid processes of stainless steel welding showed that the difference between them depends on the welded sheet thickness (or penetration depth). This value first decreases from ~100 % for sheets with δ = 2 mm to 50 % for sheets with δ = 6 mm, and at further increase of penetration depth it rises to 60 %. The nature of dependencies of the factor of area ratio φ, weld geometry K and penetration depth Φ on the speed of hybrid welding of AISI 304 steel allows recommending the range of speeds of 1.5–2.0 m/min, as a more acceptable one by the criteria of synergistic effect and penetration depth. It is found that at hybrid welding with application of fiber laser radiation, the plasma component promotes elimination of such defects of weld upper bead formation, characteristic for laser welding, as undercuts and a ridge, etc.

KEY WORDS: hybrid laser-plasma welding, fiber laser, stainless steel, synergistic effect, penetration depth, energy input

INTRODUCTION

Partial (up to 50 %) replacement of laser power by arc power in the hybrid laser-plasma process at preservation of relatively small width of the welds can make such a welding process quite attractive for a range of industrial tasks [1]. One of such tasks can be, for instance, welding of aluminium panels for railway carriages and boats, as well as stainless pipes for pipelines [2]. Due to a considerable lowering of equipment cost, it can successfully compete with laser welding, which is becoming ever wider applied now. Owing to increase of thermal locality and minimization of residual deformations, compared to the known arc welding processes, laser-plasma welding can be used for fabrication of structures from sheet materials up to 6 mm and greater thickness. Such a task is urgent, in particular, for welding stainless steels in fabrication of structures for chemical and food industries [3].

Hybrid processes of laser-arc welding attract specialists because of a range of such advantages as presence of the synergistic effect, which helps reducing the welding energy input, lowering of the requirements to edge preparation for welding, modification of the thermal cycle, which promotes elimination of hardening structures and improvement of the joint ductility, etc. [4]. At such a type of welding the arc is stabilized by the presence of focused laser radiation. However, different wave lengths of laser radiation initiate different mechanisms of arc stabilization, leading to a difference in the obtained results. This is related to a considerable dependence of total absorption rate κ_ω of laser radiation in arc plasma on its wave length λ.

In work [5] it was revealed that the stabilizing effect of the action of Nd:YAG-laser radiation is attributable to two phenomena: laser energy absorption by the arc plasma and change of arc plasma composition, caused by strong evaporation of the blank material. Both the phenomena lead to lowering of effective potential of plasma ionization and, thus, ensure higher conductivity and stability of the plasma channel. It stabilizes the arc column, promotes overcoming the disturbances caused by external forces, and improves formation of the weld root. In work [6] it is noted that at application of short wave ($\lambda \approx 1$ μm) radiation of solid-state (Nd:YAG) or fiber lasers in the hybrid process the laser beam absorption in arc plasma is negligible ($\kappa_\omega \approx 1$ m^{-1}). In this case, intensive evaporation of metal from the weld pool surface takes place un-
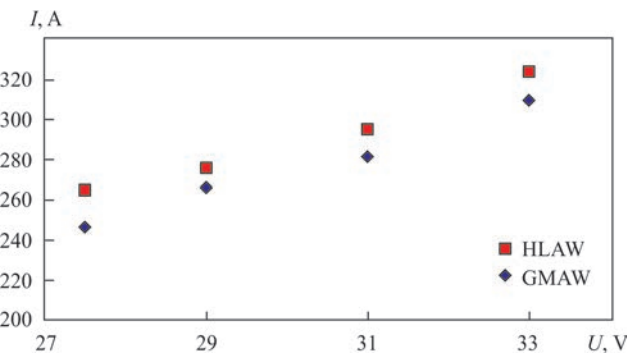
**Figure 1.** Dependence of welding current on applied voltage for feeding Mn4Ni2CrMo wire (1.2 mm diameter) in the case of hybrid (HLAW) and arc (GMAW) [8]

der the impact of highly-concentrated source of laser heating, which has a significant influence on the composition, heat, gas-dynamic and electromagnetic characteristics of the arc plasma and, consequently, leads to the change of its thermal and dynamic interaction with the metal being welded.

At application of CO_2-laser radiation ($\lambda = 10.6$ μm) in the hybrid processes both the interaction mechanisms are significant, namely: laser radiation absorption in arc column plasma ($\kappa_\omega \sim 100$ m^{-1} [6]) and metal evaporation from the melt surface under the impact of a focused laser beam. In work [7] it is shown that the interaction of a focused beam of CO_2-laser radiation with argon arc plasma with a refractory cathode leads to a certain reduction of radiation power, which reaches the surface of the anode (part being welded), as a result of partial absorption of laser radiation in the arc column plasma. Here, beam refraction in non-uniform arc plasma is negligible. Power applied to the metal being welded by the laser beam in hybrid (CO_2-laser + TIG) welding, can be both greater and smaller than the power introduced into the metal at laser welding, depending on the conditions of absorption of laser radiation, reaching the metal surface. For instance, formation of a vapour-gas channel in the weld pool promotes a more effective absorption of laser radiation, than the comparatively flat surface of the melt.

Increase of the fraction of effective (i.e. acting on the part) laser power in hybrid welding using CO_2-laser ($\lambda = 10.6$ μm) can be achieved due to a high content of helium in the welding (shielding) gas. It promotes avoiding plasma formation in the weld pool zone, absorbing the laser radiation. High-speed CCTV showed that radiation with wave length $\lambda \approx 1$ μm (Nd:YAG-, disc, fiber lasers) does not affect the electric arc similar to the case of CO_2-laser ($\lambda = 10.6$ μm) [8]. It allows application of standard gas mixtures (Ar/CO_2) and simplifies selection of parameters of the hybrid process arc component. So, in work [8] it is stated that standard GMAW parameters can be used in the hybrid process without essential correction. Figure 1 shows the effect of addition of 3 kW laser power to the standard consumable-electrode arc. In the experiment a bead was deposited on low-alloyed carbon steel plate at 1 m/min speed by Mn4Ni2CrMo wire (1.2 mm diameter), which was fed with the speed of 9 m/min at arc voltage of 27.5–33.0 V with shielding by 98%Ar+2%CO_2 gas mixture. High-speed video showed that in case of adding 3 KW fiber laser radiation, the arc looks somewhat shorter and a certain disturbance of gas shielding takes place. This disturbance is caused by release of vapor, coming out of the weld pool vapour-gas channel, and which consists both of addition of the metal vapour, and in mixing with oxygen in ambient air. Although the impact of this violation on the shielding gas properties is small, it lowers the welding current by 4–7 % during hybrid welding, compared to pure GMAW.

In work [9] it was determined that the change of arc voltage is associated with the type of laser radiation, used in hybrid welding. Application of CO_2-laser is accompanied by greater impact on the change of arc voltage, characterized by its drop (Figure 2). It was also established that increase of laser power greatly facilitates the change of voltage. At application of radiation of CO_2- and ND:YAG-lasers a practically same increase of the cross-sectional area of
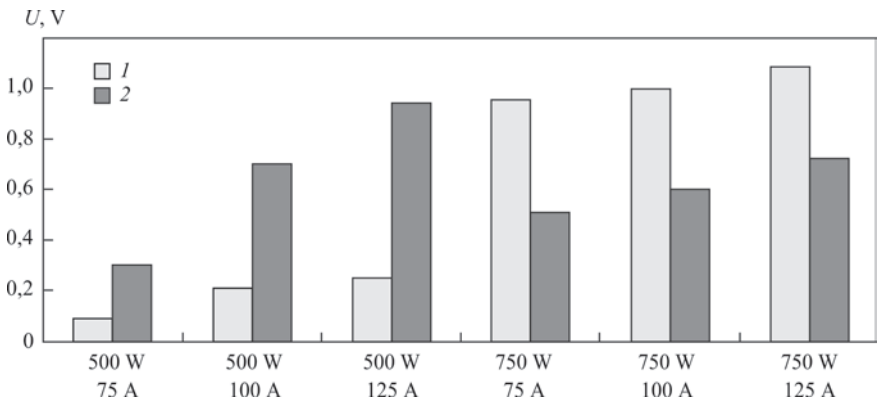
Figure 2. Difference in voltage at constant laser power [9]: *1* — CO_2-laser-TIG hybrid; *2* — Yb:YAG-laser-TIG hybrid
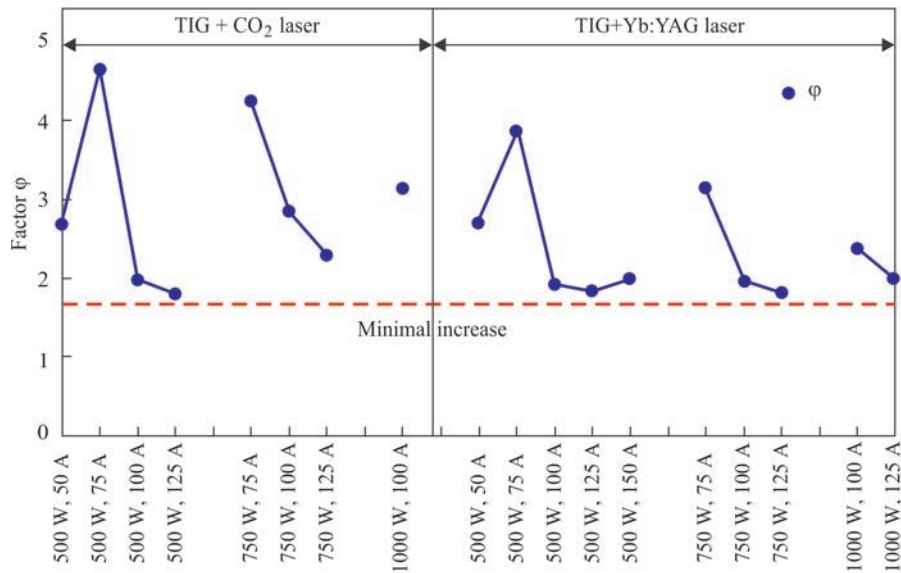
Figure 3. Factor $\varphi = \dfrac{A_{\mathrm{H}}}{A_{\mathrm{T}} + A_{\mathrm{L}}}$ as the ratio of cross-sectional area of hybrid penetration A_{H} to the sum of individual cross-sectional areas of TIG (A_{T}) and laser (A_{L}) penetrations [9]

penetration at hybrid welding is observed — at least by 1.8 times, compared to the sum of separate areas of the laser and arc (TIG) penetrations (Figure 3). Moreover, it is stated that laser radiation promotes better weld formation (Figure 4).

In recent years, fiber and disc lasers became accepted by industry. Application of CO_2-lasers is rather limited, predominantly for cutting (so-called slit lasers) [10]. Fiber and disc lasers also prevail in hybrid welding processes. Mostly MIG/GMAW, more seldom TIG torches are used as an arc source in such processes. In the opinion of the authors, however, application of a plasma source will allow improving the total efficiency of hybrid welding, due to constriction of the nonconsumable electrode arc. Moreover, the laser-plasma process will allow avoiding the need for edge preparation, which is applied in hybrid welding

of more than 5 mm thick steel sheets [11]. Therefore, a process combining welding by fiber laser radiation with plasma welding is of interest for research.

The objective of this work is investigation of the features of laser-plasma welding of up to 10 mm stainless steel, using fiber laser radiation in the mode of deep penetration of square edges.

In order to achieve this objective, the following problems were solved:

1) selection of the modes of laser, plasma and hybrid welding of stainless steel by the criteria of the quality of weld formation without edge preparation;

2) comparison of the cross-sectional areas of penetrations, made by the three studied processes, to determine the presence of the synergistic effect;

3) comparison of energy inputs of the laser and hybrid processes of stainless steel welding;
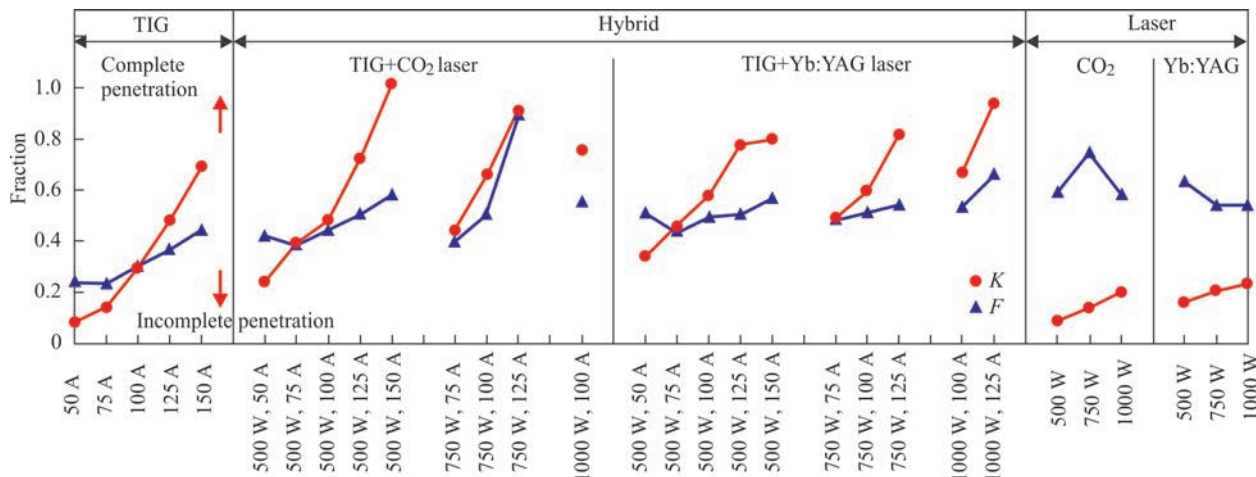
Figure 4. Change of the parameters of weld geometry K and penetration depth Φ depending on welding parameters ($K = D/W$, where D is the penetration depth; W is the weld width; $\Phi = D/T$, where D is the penetration depth; T is the blank thickness) [9]

Table 1. Chemical composition of AISI 304 steel sheets used in studies

Fe	C	Si	Mn	Cr	Ni	Ti	Cu	S	P
Base	≤0.8	≤0.8	≤0.2	17.0–19.0	9.0–11.0	≤0.5	≤0.3	≤0.02	≤0.035
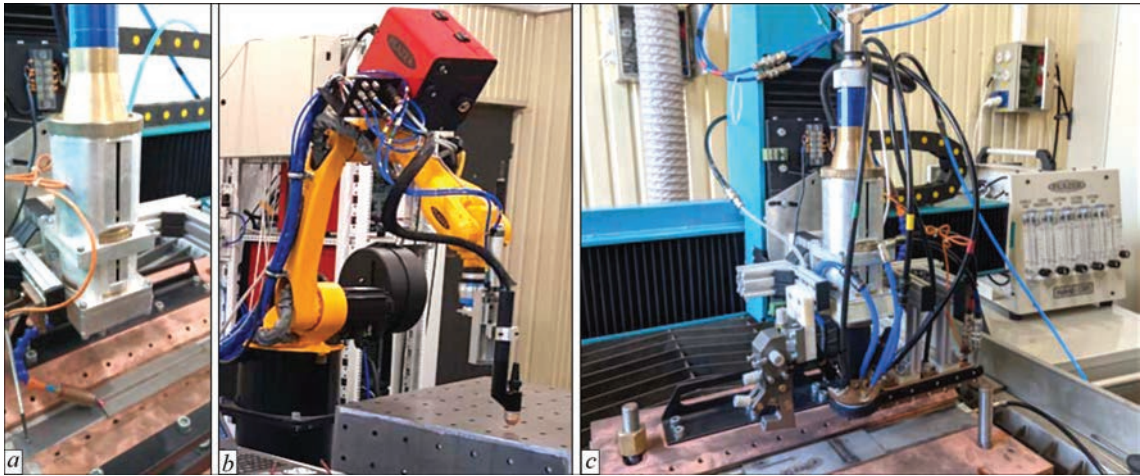
Figure 5. Appearance of laboratory stands for conducting technological studies on welding: *a* — laser; *b* — plasma; *c* — hybrid

4) optimization of hybrid welding mode by the parameters of the ratio of penetration areas and weld geometry;

5) determination of the difference in application of fiber laser radiation from application of the diode, Nd:YAG- and CO_2-lasers.

Sheets of $100 \times 50 \times \delta$ mm to $300 \times 100 \times \delta$ mm size from stainless steel AISI 304 of thickness $\delta = 2, 4, 6$ and 10 mm (Table 1) were used as the sample material. Welding was performed in argon shielding (flow rate of ~30 l/min). Argon was also used as plasma gas.

A laboratory stand was built to perform the experiments, which was fitted with the heads for laser, plasma and hybrid welding (Figure 5). At the first stage of studies, investigations were performed to compare the influence of lateral and coaxial methods of shielding gas feeding on the produced penetration depth in welding by fiber laser radiation. These investigations showed comparatively close results, which is indicative of a low level of radiation losses in the plasma flame, forming above the weld pool.

More over, at the same stage of the study the main technological parameters of butt welding of AISI 304 steel samples by laser and plasma processes were established. The welding speeds and heat source powers, at which sound formation of butt welded joints is observed, were determined experimentally (Table 2). It was also established that in laser welding of up to 6 mm thick sheets application of filler wire to improve formation of the upper bead and weld root is not mandatory. However, with increase of welded sheet thickness the upper bead formation can become worse, because of undercut appearance.

Table 2. Comparison of the effectiveness of different processes of AISI 304 steel welding by energy input criterion (E, J/mm)

No	Welding process/ number of passes	Sheet thickness δ, mm	Power P ($P_{las} + P_{pl}$), kW	Current I, A	Arc voltage U, V	Welding speed, V, m/min	$E_{las} + E_{pl}$, J/mm	E_{Σ}, J/mm
1	Laser/1	2	0.8	–	–	1.0	36	36
2	Plasma/1	2	2.2	80	28	0.3	336	336
3	Hybrid/1	2	0.8 + 2.2	80	28	1.5	24 + 68	92
4	Laser/1	4	1.6	–	–	1.0	72	72
5	Hybrid/1	4	1.6 + 2.2	80	28	1.5	48 + 66	114
6	Hybrid/1	4	1.5 + 2.9	95	30	1.5	45 + 87	132
7	Hybrid/1	4	1.8 + 2.0	83	25	1.5	54 + 60	114
8	Laser/1	6	1.8	–	–	0.8	104	104
9	Hybrid/1	6	1.8 + 2.0	80	25	1.2	71 + 82	153
10	Laser/2	10	1.8	–	–	0.75	108·2	108·2
11	Hybrid/2	10	1.8 + 2.0	80	25	1.0	(81+90)·2	171·2

At the second stage of the study, experiments on hybrid welding were performed in the range of speeds of 0.25–4.0 m/min at up to 2 kW laser power and up to 100 A welding current. A directly proportional influence of laser radiation power on the penetration depth and of plasma power on its width was established. In addition, plasma component of the hybrid process promoted better formation of upper bead of the welds and eliminated the danger of undercut appearance in welding sheets of 4–10 mm thickness (Figure 6). It allows achieving sound weld formation in the entire range of the studied thicknesses without filler wire application.

At the third stage of the study, presence of a synergistic effect was found, which is usually characteristic for hybrid laser-plasma welding. For this purpose, the cross-sectional planes of penetrations, made in AISI 304 sheet ($\delta = 4$ mm) by the three studied processes at the speeds of 2 and 4 m/min were measured and compared (Figure 7). Here, the energy parameters of each of these processes were unchanged and equal to: radiation power $P = 1.6$ kW, welding current $I = 80$ A at arc voltage of 24 V. Cross-sectional area $S1$ of hybrid penetration was compared with the sum of planes $S2$ and $S3$ of the laser and plasma penetrations. In the case of welding at the speed of 4 m/min, the plasma process practically did not produce any penetration. It was established that at the speed of 2 m/min area $S1 = 3.121$ mm^2 of hybrid penetration exceeds the sum of planes $S2 + S3 = 2.383 + 0.046$ mm^2 by almost 30 %, and at the speed of 4 m/min (hybrid — 1.653 mm^2, laser — 1.32 mm^2, no penetration in plasma process) by ~20 %. This is indicative of the indubitable presence of the synergistic effect at hybrid welding.

For comparison of the effectiveness of the studied laser, plasma and hybrid welding processes the values
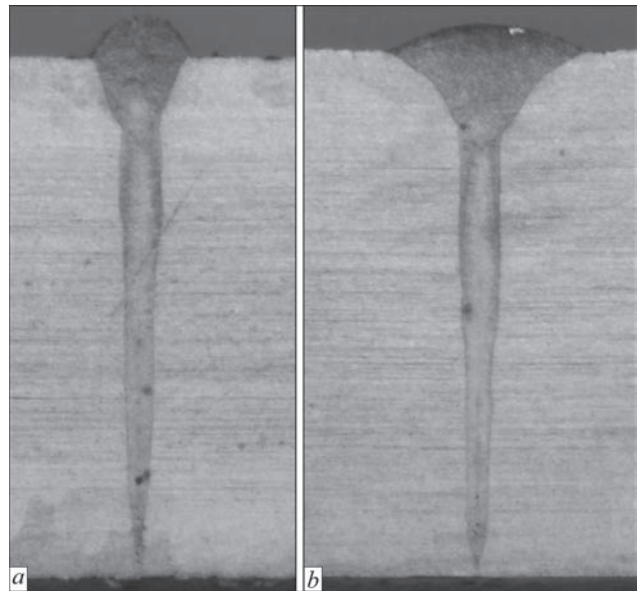
Figure 6. Transverse sections of penetrations in AISI 304 sheet ($\delta = 4$ mm) made by laser (*a*) and hybrid (*b*) processes at the speed of 4 m/min

of their energy inputs E_{las}, E_{pl}, and E_{Σ}, J/mm were used. These values were defined as the ratio of welding source power to welding speed, multiplied by the respective process efficiency. The efficiency values were taken from the recommendations in published sources. So, the efficiency of welding stainless steel by fiber laser radiation is equal to 75 % [12, 13]. The efficiency of plasma welding can be selected in a similar fashion [14]. It is anticipated that the efficiency of laser-plasma welding should equal to approximately 75 %. This is confirmed by investigations of the authors of [15]. The data, entered into Table 2, were derived, proceeding from the performed studies and given values of total efficiency of the above-mentioned processes.

Performed investigations showed that in welding 2 mm samples the process is predominantly heat con-
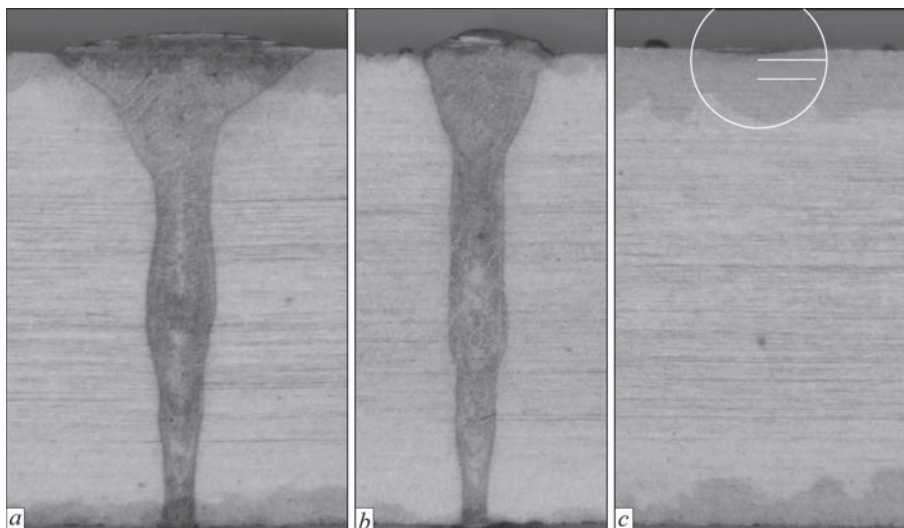
Figure 7. Comparison of cross-sectional areas of penetrations produced at the speed of 2 m/min in AISI 304 sheet ($\delta = 4$ mm) by hybrid (*a*), laser (*b*) and plasma (*c*) processes

13
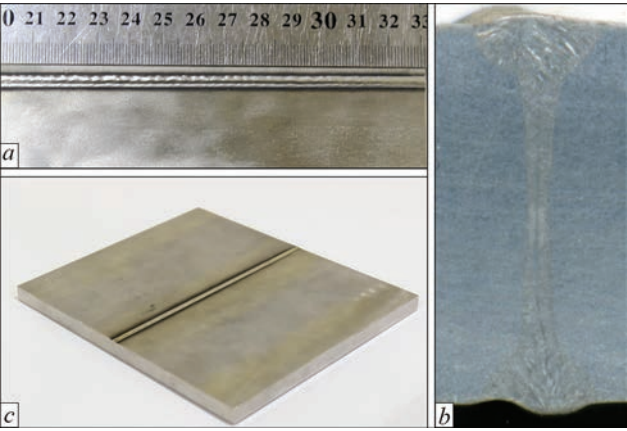
Figure 8. Two-pass hybrid welding of AISI 304 sheets (δ = = 10 mm): *a* — weld appearance; *b* — transverse section; *c* — welded joint appearance

ducting, and does not require the presence of filler materials. At increase of the sample thickness up to 4 mm and higher, weld formation goes into the keyhole mode. In order to increase the penetration depth, attempts were made to lower the welding speed. Penetration of AISI 304 sheet of thickness δ = 10 mm with radiation power of 2.0 kW allowed reaching a depth of the order of 7–8 mm at laser and 8 mm at the hybrid process in the case of 0.45 m/min speed. In both the cases, further lowering of welding speed from 0.45 to 0.25 m/min did not lead to deeper penetration. Therefore, in order to produce a butt joint of sheets of thickness δ = 10 mm, two-pass welding was used, which was made from two sides with weld root overlapping (Figure 8). Further static rupture tests of the welded samples showed that strength of the joints produced by hybrid welding is on the level of 95 % of base metal strength.
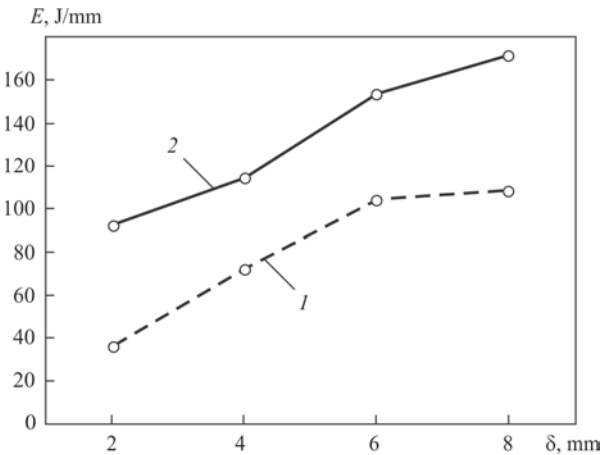
At the last fourth stage of studies comparison of input energies of the laser and hybrid processes of stainless steel welding was performed. It showed that the difference between them somewhat decreases with increase of the welded sample thickness. So, in weld-

Figure 9. Dependencies of welding energy input E on thickness δ of AISI 304 steel sample: *1* — laser welding; *2* — hybrid welding

ing AISI 304 of thickness δ = 2 mm the difference in energy input of the hybrid process is approximately two times higher than that of the laser process (Table 2, modes No.1 and No.3), for δ = 4 mm this difference is equal to approximately 60 % (Table 2, modes No.6 and No.7), and for δ = 6 mm it is on the level of 50 % (Table 2, modes No.10 and No.11). Further increase of penetration depth (for instance, to 8 mm) leads to increase of this difference to 60 % (Figure 9). This can be partially related to transition from the heat conductivity process of welding samples of thickness δ = 2 mm to the keyhole process, characteristic for greater thicknesses.

On the whole, investigation of laser-plasma welding leads to the conclusion that the impact of plasma is predominantly reduced to the following: heating of the surface of the metal being welded, remelting of the weld upper part, improvement of upper bead formation. In its turn, plasma heating of the surface of the metal being welded, promotes improvement of the absorption coefficient of laser radiation that improves the effective efficiency of welding [16]. The impact of fiber laser radiation in the hybrid laser-plasma process is reduced to ensuring a certain penetration depth and root bead formation. Investigations show that both at laser, and at laser-plasma welding fixed laser power allows reaching a fixed penetration depth. Here, speed lowering below a certain threshold, does not allow increasing this depth. To increase it, it is necessary to raise the laser power. Formation of the welded joint root bead in the hybrid process is somewhat improved, compared to the laser process, primarily due to increase of the energy input.

In the case of the hybrid process with mode parameters P = 1.8 kW, I = 80 A; U = 25 V at application of fiber laser, graphs of the dependencies of weld geometry parameters on welding speed V, recommended in work [9], were plotted (Figure 10). The shape of these dependencies allows stating that increase of welding speed from 1.5 to 2.0 m/min is rational. Further increase of speed somewhat impairs the synergistic effect from the hybrid process. However, at continuous raising of the speed to 4.0 m/min an increase of the weld geometry parameter K is observed, even though it is not as intensive, as before, and decrease of factor φ is not too rapid. It allows stating that in the considered case of laser-plasma welding, the range of speeds of 1.5–2.0 m/min is the most favourable.

Comparison of the above-given data with the earlier obtained results of laser-plasma welding using diode and CO_2-laser radiation (for instance, [17]) shows the following. Diode laser radiation was focused into a spot of rather large diameter (~1.0 mm) so that its power density was up to $2.5 \cdot 10^5$ W/cm². A smaller di-
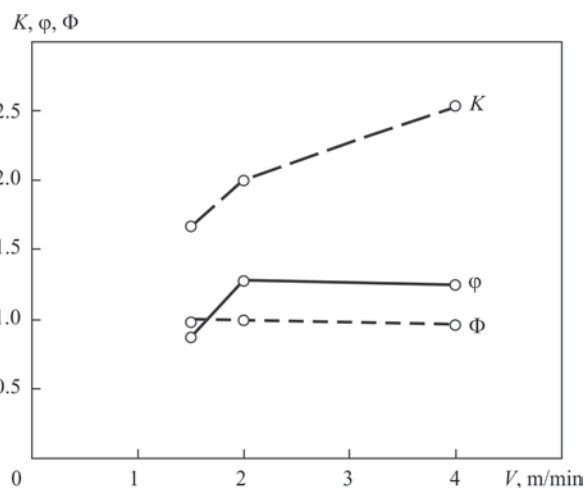
ameter of the radiation focal spot of a fiber laser (of the order of 0.05 mm) allows reaching a higher power density (up to 10^8 W/cm^2) and much greater penetration depth, compared to the diode laser. In all the other aspects, the effect of both the types of laser radiation on the hybrid process is similar. A similar situation was observed in the case of application of Nd:YAG-laser radiation, which was focused into a 0.4 mm spot (power density up to $3.5 \cdot 10^6$ W/cm^2). Reduction of penetration depth, both at laser, and at hybrid welding by Nd:YAG-laser radiation is also promoted by a smaller radiation absorption coefficient (close to 50 %, in keeping with [18]).

In the case of application of CO_2-laser radiation, a fundamentally different mechanism of its impact on the hybrid process is in place. A significant part of such radiation is absorbed by the plasma component of the laser-plasma process, overheats it, directs it to the point of impact on the part being welded and provides the simultaneous action of the two heat sources. Due to that, the synergistic effect of the laser-plasma process at application of CO_2-laser radiation is more pronounced and increases the cross-sectional area of the welds up to 50 %, compared to the sum of the planes of welds produced by the laser and plasma components separately. However, due to smaller values of radiation power density (up to 10^7 W/cm^2) and its absorption coefficient (on the level of 20–40 % according to [19]), the penetration depth is smaller, compared to application of the fiber laser, both in laser, and in hybrid welding.

Investigations showed that in the case of close values of energy, applied to the samples being welded (radiation and plasma powers of ~2 kW each at process speed of the order of 1.5 m/min), application of diode laser radiation in the hybrid process allows welding stainless steel sheets of ~2 mm thickness, application of Nd:YAG laser — up to 3.5 mm, for CO_2-lasers it is ~3 mm, while application of a fiber laser allows joining more than 4 mm (tentatively 5 mm). In the case of laser welding at the same speed at 2 kW power the penetration depths will be equal to: for diode laser radiation – up to 1 mm, for Nd:YAG-laser — up to 3 mm, for CO_2-laser — up to 2 mm, and for fiber laser — more than 4 mm (tentatively 4.8 mm). It can be stated that application of the radiation of diode, Nd:YAG-, CO_2- and fiber lasers, allowing for the difference in power density and absorption coefficients in laser-plasma welding, increases the penetration depths by 100, 15, 33 and 4 %, respectively, compared to their laser welding. Here, the effectiveness of application of a fiber laser in the hybrid process exceeds the effectiveness of diode laser application by 60 %, Nd:YAG-laser — by 30 %,

Figure 10. Dependence of factor of plane ratio φ, weld geometry K and penetration depth Φ on speed V of hybrid welding of AISI 04 steel

CO_2-laser — by 40 %. Therefore, the general result of application of fiber laser radiation in laser-plasma welding can be regarded as the most effective in terms of penetration depth and improvement of the process effective efficiency.

CONCLUSIONS

1. Presence of the synergistic effect on laser-plasma welding with fiber laser application was confirmed by comparing the cross-sectional areas of penetrations made in a sheet of stainless steel of AISI 304 grade (δ = 4 mm) by laser, plasma and hybrid (laser-plasma) processes. It was found that the manifestation of this effect depends on welding speed. At the welding speed of 2 m/min at the power of laser radiation and plasma arc of ~2kW each the cross-sectional area of hybrid penetration (3.121 mm^2) is greater than the sum of cross-sectional areas, obtained by laser (2.383 mm^2) and plasma (0.046 mm^2) processes, by 30 %, and for the speed of 4 m/min the specified excess reaches ~20 %.

2. It was determined that the laser-plasma welding of stainless steel using a fiber laser differs from similar processes with application of diode, Nd:YAG-, CO_2-lasers, namely, it allows increasing the penetration depth at simultaneous reduction of its width. So, at application of laser and plasma power of ~2 kW each at the speed of ~1.5 m/min, the penetration depth with application of the fiber laser in the hybrid process increases, compared to the use of the diode laser by 60 %, Nd:YAG-laser — by 30 %, CO_2-laser — by 40 %.

3. Increase of penetration depth at hybrid laser-plasma welding, compared to the laser process, depends on radiation wave length, power density and absorption capacity of the welded surface. So, in stainless steel welding with application of laser and plasma power of ~2 kW each at the

speed of ~1.5 m/min the contribution of the plasma energy source increases the penetration depth at diode laser application by ~100 %, for Nd:YAG-laser — by 15 %, for CO_2-laser — by 33 %, and for fiber laser — by 4 % (compared to laser welding by the same radiation of ~2 kW at the speed of ~1.5 m/min).

4. Comparison of input energies of laser (E_{las}, J/mm) and hybrid (E_Σ, J/mm) processes of stainless steel welding showed that the difference between them depends on the welded sheet thickness (or penetration depth). E_Σ / E_{las} parameter first decreases from ~100 % for sheets with $\delta = 2$ mm to 50 % for sheets with $\delta = 6$ mm, and at further increase of penetration depth from 6 to 8 mm this value rises from 50 to 60 %.

5. Analysis of the behaviour of factor φ (ratio of the cross-sectional area of hybrid penetration to the sum of cross-sectional areas of plasma and laser penetrations), which characterizes the synergistic effect, shows its increase in 1.5–2.0 m/min speed range of AISI 304 steel welding with further slight decrease in the range of 2.0–4.0 m/min. Weld geometry parameter K (ratio of penetration depth to weld width) increases in the entire analyzed speed range (1.5–4.0 m/min). The penetration depth parameter Φ (ratio of penetration depth to blank thickness) somewhat decreases in this range. Comprehensive analysis of the behaviour of these three parameters allows recommending the speed range of 1.5–2.0 m/min for laser-plasma welding of stainless steel with application of fiber laser radiation, as more acceptable one by the criteria of the synergistic effect and penetration depth.

6. At hybrid welding with application of fiber laser radiation the plasma component promotes elimination of such defects of weld upper bead formation, characteristic for laser welding, as undercuts and ridge, and increases the radiation absorption coefficient due to heating of the welded part surface. In the range of speeds of 0.25–4.0 m/min at fiber laser power from 0.8 to 2.0 kW and welding current from 0 to 100 A a directly proportional increase of penetration depth from 2 to 8 mm (depending on laser power), and increase of upper bead reinforcement width from 1.5 to 5.5 mm (depending on plasma power) are in place.

REFERENCES

1. Khaskin, V.Yu., Korzhyk, V.M., Bernatskii, A.V. et al. (2020) Features of synergistic effect manifestation in laser-plasma welding of SUS304 steel, using disc laser radiation. *The Paton Welding J.*, **4**, 29–33. DOI: https://doi.org/10.37434/as2020.04.04

2. Thomy, C., Seefeld, T. (2006) Basics and applications of laser-GMA hybrid welding. *Ibid.*, **6**, 28–32.

3. Simões, L.M.C. (2010) Design, fabrication and economy of welded structures. *Structural and Multidisciplinary Optimization*, 40(**1**), 629–629. DOI: https://doi.org/10.1007/s00158-008-0356-y

4. Kah, P., Salminen, A., Martikainen, J. (2010) Laser-arc hybrid welding processes (Review). *The Paton Welding J.*, **6**, 32–40.

5. Hu, B., Ouden, G. den. (2005) Laser induced stabilization of the welding arc. S*ci. and Technol. of Welding and Joining*, 10(**1**), 76–81. DOI: https://doi.org/10.1179/174329305X29537

6. Seyffarth, P., Krivtsun, I. (2002) *Laser-arc processes and their applications in welding and material treatment.* London, Taylor and Francis Books, 1. DOI: https://doi.org/10.1201/9781482264821

7. (2018) *Physical processes in welding and processing of materials. Theoretical study, mathematical modeling, computational experiment.* In: Transact. of NANU. Ed. by V.I. Krivtsun. Kiev, IAW [in Russian].

8. Eriksson, I., Powell, J., Kaplan, A. (2013) Guidelines in the choice of parameters for hybrid laser arc welding with fiber lasers. *Physics Procedia*, **41**, 119–127. DOI: https://doi.org/10.1016/j.phpro.2013.03.059

9. Reisgen, U., Krivtsun, I., Gerhards, B., Zabirov, A. (2016) Experimental research of hybrid welding processes in combination of gas tungsten arc with CO_2- or Yb:YAG laser beam. *J. of Laser Applications,* **28**, 022402. DOI: https://doi.org/10.2351/1.4944096

10. Wetzig, A., Herwig, P., Hauptmann, J. et al. (2016) Latest developments of laser cutting. *Ibid., ICALEO 2016*, **103**. DOI: https://doi.org/10.2351/1.5119063

11. Jokinen, T., Vihervä, T., Riikonen, H. (2000) Welding of ship structural steel A36 using a Nd:YAG laser and gas–metal arc welding. *Ibid.*, **12**, 185–189. DOI:https://doi.org/10.2351/1.1309549

12. Sokolov, M., Salminen, A. (2014) Improving laser beam welding efficiency. *Physics Procedia*, 6(**09**), 559–571. DOI:https://doi.org/10.4236/eng.2014.69057

13. Sokolov, M., Salminen, A., Somonov, V., Kaplan, A.F.H. (2012) Laser welding of structural steels: Influence of the edge roughness level. *Optics & Laser Technology*, 44(**7**), 2064–2071. DOI: https://doi.org/10.1016/j.optlastec.2012.03.025

14. DuPont, J.N., Marder, A.R. (1995) Thermal efficiency of arc welding processes. *Welding J.*, 74(**12**), 406–416.

15. Hipp, D., Mahrle, A., Beyer, E. et al. (2019) Thermal efficiency analysis for laser-assisted plasma arc welding of AISI 304 stainless steel. *Materials (Basel)*, 12(**9**):1460, 1–14. DOI: https://doi.org/10.3390/ma12091460

16. Khaskin, V.Yu., Korzhik, V.N., Chizhskaya, T.G. et al. (2016) Effect of laser radiation absorption on efficiency of laser welding of copper and its alloys. *The Paton Welding J.*, **11**, 31–35. DOI: https://doi.org/10.15407/tpwj2016.11.05

17. Krivtsun, I.V., Shelyagin, V.D., Khaskin, V.Yu. et al. (2007) Hybrid laser-plasma welding of aluminium alloys. *Ibid.*, **5**, 36–40.

18. Fuerschbach, P.W., Eisler, G.R. (2002) Effect of laser spot weld energy and duration on melting and absorption. *Sci. and Technol. of Welding and Joining*, **7**, 241–246. DOI: https://doi.org/10.1179/136217102225004293

19. Fuerschbach, P.W. (1996) Measurement and prediction of energy transfer effi ciency in laser beam welding. *Welding J.*, **75**, 24–34. DOI: https://doi.org/AC04-94AL85000

ORCID
V.M. Korzhyk: 0000-0001-9106-8593,
V.Yu. Khaskin: 0000-0003-3072-6761,
A.A. Grynyuk: 0000-0002-6088-7980,
E.V. Illyashenko: 0000-0001-9876-0320,
A.V. Bernatskyi: 0000-0002-8050-5580,
S.I. Peleshenko: 0000-0001-6828-2110

CONFLICT OF INTEREST
The Authors declare no conflict of interest

CORRESPONDING AUTHOR
V.Yu. Khaskin
E.O. Paton Electric Welding Institute of the NASU
11 Kazymyr Malevych Str., 03150, Kyiv, Ukraine
E-mail: khaskin1969@gmail.com

CALCULATED-EXPERIMENTAL MODEL OF DISTRIBUTION OF NON-METALLIC INCLUSIONS IN THE METAL OF WELDS BY SIZES

L.A. Taraborkin, **V.V. Holovko**

E.O. Paton Electric Welding Institute of the NASU
11 Kazymyr Malevych Str., 03150, Kyiv, Ukraine

ABSTRACT

There is a large number of investigations on the impact of distribution of non-metallic inclusions in the weld metal on its structure and mechanical properties. However, the authors of these works do not describe the kinetics of forming such a distribution. The results of the development of a distribution model in the weld metal of non-metallic inclusions by sizes are presented. Formation of the calculation part of the model is based on the processing of experimental data on the sizes of non-metallic inclusions in the metal of welds, deposited by the methods of submerged arc welding and in shielding gas. Generalization and analysis of experimental data showed that the final distribution of inclusions in the metal of the studied welds is submitted to the law of gamma-distribution (probability is > 95 %). To describe the evolution of the distribution of non-metallic inclusions during weld formation, the authors proposed to apply a probabilistic model in the form of gamma-distribution with time-dependent parameters.

KEY WORDS: low-alloy steel, welding, weld metal, non-metallic inclusions, distribution

INTRODUCTION

Non-metallic inclusions are an integral component of the weld metal structure. Their characteristics such as chemical composition, sizes, distribution density in a solid solution have a significant impact on mechanical properties of weld metal, which determines the relevance of the possibility of their forecasting. In connection with the ever-increasing volume of low-alloy high-strength steels in the manufacture of metal structures, in recent years a lot of attention is paid to the study of the possibilities of providing mechanical properties of welded joints on steels of this type at the level of the base metal. A significant influence on the conditions for the microstructure formation and mechanical properties of weld metal from non-metallic inclusions was shown [1–4], that affect the processes of crystallization, formation of primary and secondary microstructure. But at the same time, in parallel, a change in the parameters of their size, distribution density, composition and surface compounds is observed. In the weld metal, the final result of the processes of forming non-metallic inclusions (deoxidation of liquid metal, crystallization of weld pool, diffusion in a solid solution) was recorded, which occurs in different temperature ranges. The intensity of the development of each of the stages of these processes affects the final distribution of non-metallic inclusions. Thus, for example, in [5] it was shown that the time of existing a liquid phase during cooling of the metal has a significant impact on the sizes of inclusions. Therefore, to predict the characteristics of

inclusions, it is necessary to take into account not only the chemical composition of the weld pool, but also the time of its existence. It should be noted that despite a large number of works, in which the influence of the composition, morphology and sizes of non-metallic inclusions on the structure and mechanical properties of weld metal, insufficient attention was paid to the issue of the effect of the distribution of inclusions, depending on their size.

STATE-OF-THE-ART OF THE PROBLEM

The distribution of non-metallic inclusions in metals by sizes is numerically characterized by means of the function of the distribution density, which is generally determined by solving the Smoluchowski equation [6]. However, since the processes of coarsening non-metallic inclusions are rather complicated in any metallurgical system, then for such a solution it is necessary to introduce additional assumptions regarding the conditions and characteristics of the relevant process that are not always equipped with the necessary numerical values of parameters or not subjected to checking at all. For example, in the mentioned work [6], a list of the mentioned assumptions has 19 points. Therefore, another calculation and experimental approach is used, namely: based on a large array of accumulated experimental data, researchers are trying to approximate experimentally observed distributions of non-metallic inclusions by sizes by certain known mathematical functions of distributions.

In particular, in [7, 8] it is noted that distribution of non-metallic inclusions by sizes for some non-stationary metallurgical processes can be considered as

a constant exponential distribution and described by the formula

$$n(r) = n_0 \exp(-\lambda r), \quad r_0 < r < r_{max}, \qquad (1)$$

where the parameters n_0, λ depend on specific conditions and equipment, and inclusions have a shape of the sphere with the current radius r.

Formula (1) is suitable in the case of such metallurgical processes of steel production as a circulating vacuuming, vacuum refining, continuous pouring and ladle treatment. For these processes, the values λ are in the range from 0.44 to 0.75 for the radii of non-metallic inclusions from 1 to 30 μm [7].

It is known, that both the sizes of non-metallic inclusions themselves, as well as the density of their distribution by sizes depends on duration of the processes of inclusion formation [8–10].

The process of forming non-metallic inclusions in the welding pool is significantly different both as to its thermodynamic as well as to physico-chemical characteristics from the corresponding processes of a "large" metallurgy. Certain attempts on numerical evaluation of trends in changing the density of non-metallic inclusions depending on their sizes [11] can be noted, but in general, in scientific and technical literature, descriptions of models for calculating the distribution of inclusions in the weld metal by sizes are absent, which would allow performing the corresponding numerical forecasts, although the urgency of possibility of such forecasts is undoubted.

PROCEDURE OF WORK

Digital images of the surface of non-etched sections were obtained in the NEOPHOT-30 optical microscope with the use of a high-resolution digital camera. Further images were processed in order to increase the accuracy of a further recognition of non-metallic inclusions by means of the special software (Gaussian filter was used [12]). The size of each image amounts to 2592 by 1944 pixels. Processed images were subjected to recognition with the use of the special software (trial version of Media Cybernetics ImagePro, available on the site of the manufacturer http://www.mediacy.com/). According to this methodology, the volumetric content ($V_{nm.inc}$) and distribution of non-metallic inclusions in the weld metal was determined.

Consideration of the nature of distribution of non-metallic inclusions was started from the model (1), found for the processes of steel making. The value of the parameter n_0 for the conditions of weld pool existence can be determined based on the law of conservation of a substance based on such considerations:

The amount of oxygen in the inclusion of radius r and density ρ_{inc} is equal to $\frac{4}{3}\pi r^3 \rho_{inc} X_O$, where X_O is the mass fraction of oxygen in the inclusion. Then, according to the expression (1), the amount of oxygen in the inclusions of radius r is equal to

$$\frac{4}{3}\pi r^3 \rho_{inc} X_O n(r) = \frac{4}{3}\pi \rho_{inc} X_O n_0 e^{-\lambda r} r^3.$$

Consequently, the total amount of oxygen contained in the inclusions with the radius ranging from r_{min} to r_{max} is determined by the integral

$$\frac{4}{3}\pi \rho_{inc} X_O n_0 \int_{r_{min}}^{r_{max}} r^3 e^{-\lambda r} dr. \qquad (2)$$

On the other hand, having marked density of molten steel by ρ_s, and the content of oxygen in the inclusions for the unit of a molten metal mass by w_O, the mentioned amount of oxygen in the inclusions can be evaluated by the product $\rho_s w_O$, which, according to the law of conservation of a substance, should be equated to the expression (2):

$$\frac{4}{3}\pi \rho_{inc} X_O n_0 \int_{r_{min}}^{r_{max}} r^3 e^{-\lambda r} dr = \rho_s w_O.$$

From the last equality we obtain an expression for the parameter n_0:

$$n_0 = \frac{3\rho_s w_O}{4\pi \rho_{inc} X_O \displaystyle\int_{r_{min}}^{r_{max}} r^3 e^{-\lambda r} dr}. \qquad (3)$$

In order to simplify the work with the expression (3), following [12], w_O can be replaced in it by [O%], i.e., the total amount of oxygen in molten metal. Such a replacement means that further results on the number of inclusions will actually provide the upper limit of numerical evaluation.

In addition, the integral in the denominator of the fraction from the expression (3) can be calculated exactly, as far as according to [13]

$$\int x^3 e^{ax} dx = e^{ax}\left(\frac{x^3}{a} - \frac{3x^2}{a^2} + \frac{6x}{a^3} - \frac{6}{a^4}\right),$$

from which it follows that

Table 1. Chemical composition and content of non-metallic inclusions in the weld metal

Weld number	Mass fraction (%) in the weld metal												V_{nmincl}, %
	C	Si	Mn	S	P	Cr	Ni	Mo	Cu	Al	Ti	O	
NN1	0.034	0.212	1.51	0.023	0.021	0.41	3.74	0.44	0.12	0.022	0.009	0.078	0.62
NN2	0.038	0.417	1.57	0.025	0.022	0.33	3.50	0.52	0.13	0.034	0.044	0.070	0.58
NN3	0.034	0.321	1.38	0.023	0.015	0.39	3.83	0.51	0.12	0.020	0.005	0.067	0.55
NN4	0.050	0.290	1.32	0.024	0.014	0.16	2.19	0.27	0.36	0.039	0.019	0.061	0.47
NN5	0.049	0.298	1.39	0.023	0.015	0.15	2.26	0.25	0.44	0.039	0.008	0.072	0.58

$$\int_{r_{min}}^{r_{max}} r^3 e^{-\lambda r} dr =$$

$$= \frac{1}{\lambda}\left[\exp\left(-\lambda r_{max}\right) r_{max}^3 - \exp\left(-\lambda r_{min}\right) r_{min}^3\right] -$$

$$-\frac{3}{\lambda^2}\left[\exp\left(-\lambda r_{max}\right) r_{max}^2 - \exp\left(-\lambda r_{min}\right) r_{min}^2\right] + \quad (4)$$

$$+\frac{6}{\lambda^3}\left[\exp\left(-\lambda r_{max}\right) r_{max} - \exp\left(-\lambda r_{min}\right) r_{min}\right] -$$

$$-\frac{6}{\lambda^4}\left[\exp\left(-\lambda r_{max}\right) - \exp\left(-\lambda r_{min}\right)\right].$$

Taking into account the fact that the values of the smallest and largest radii of inclusions differ by at least an order of value, it is possible to obtain a simple approximate numerical evaluation by a further replacement of a finite integral to an infinite one in the interval (from 0 to ∞) in the expression (3), then, according to [13]:

$$\int_0^{\infty} r^3 e^{-\lambda r} dr = \frac{6}{\lambda^4}$$

and, therefore

$$n_0 = \frac{1}{8\pi} \frac{\rho_s}{\rho_{inc}} \frac{[O\%]}{X_O} \lambda^4. \quad (5)$$

The relative error of calculation according to the formula (5) is lower than 2.4 % as compared to the calculation by exact quadrature (4).

OBTAINED RESULTS

In order to check the suitability of the distribution modeling according to the formula (1), experimental studies were performed, where the characteristics of non-metalic inclusions in the weld metal were determined, which differed in the time of existence of the liquid metal of the welding pool depending on the input energy of the process as well as its chemical composition. The specimens of the deposited metal, produced in submerged arc welding of butt joints of low-alloy steel 10KhSND of 14 mm thickness with an input energy of 36 kJ/cm (welds NN-1, NN-2, NN-3), as well as in a shielding gas with an input en-

ergy of 21 kJ/cm (welds NN-4, NN-5), were subjected to examination. The parameters of the welding mode meet the requirements of the standards ISO 14171 (submerged arc welding) and ISO 26304 (welding in a shielding gas). The chemical composition of the metal of welds and their content of non-metallic inclusions ($V_{nm.inc}$) are given in Table 1. Other features of the procedure of experimental investigations are presented in [13].

Our experimental study of distribution of non-metallic inclusions in the metal of welds produced by the methods of submerged arc and flux-cored wire welding (Figure 1) showed that experimental distributions are not exponential with a reliable probability of at least 95 % according to Pearson and Kolmogorov-Smirnov criteria.

Analytical analysis showed that the available experimental data can be described by the gamma-distribution function with a set reliable probability.

To analyze the distribution of non-metallic inclusions, the density function of the gamma-distribution probability was used, which has the form [13]

$$f\left(x;\alpha,\beta\right) = \frac{x^{\alpha-1}\exp\left(-\dfrac{x}{\beta}\right)}{\beta^{\alpha}\Gamma\left(\alpha\right)}, \quad (6)$$

$$\alpha,\beta > 0; \quad 0 < x < \infty,$$

where $\Gamma(\alpha)$ is the gamma function; parameters α and β are called shape and scale parameters, respectively.

This distribution is characterized by the fact that many other distributions are its partial cases. In particular, as is seen from the formulas (6) and (1), provided that the parameter of the shape $\alpha = 1$, the gamma-distribution is converted into an exponential distribution. Moreover, in the case of increase in the value of the shape parameter, the distribution behaviour changes qualitatively (Figure 2).

Analysis of the behaviour of the probability density functions of exponential and gamma-distribution, as well as the physical phenomenon of coarsening non-metallic inclusions due to coagulation leads to the following model description of the distribution of non-metallic inclusions in the weld metal.
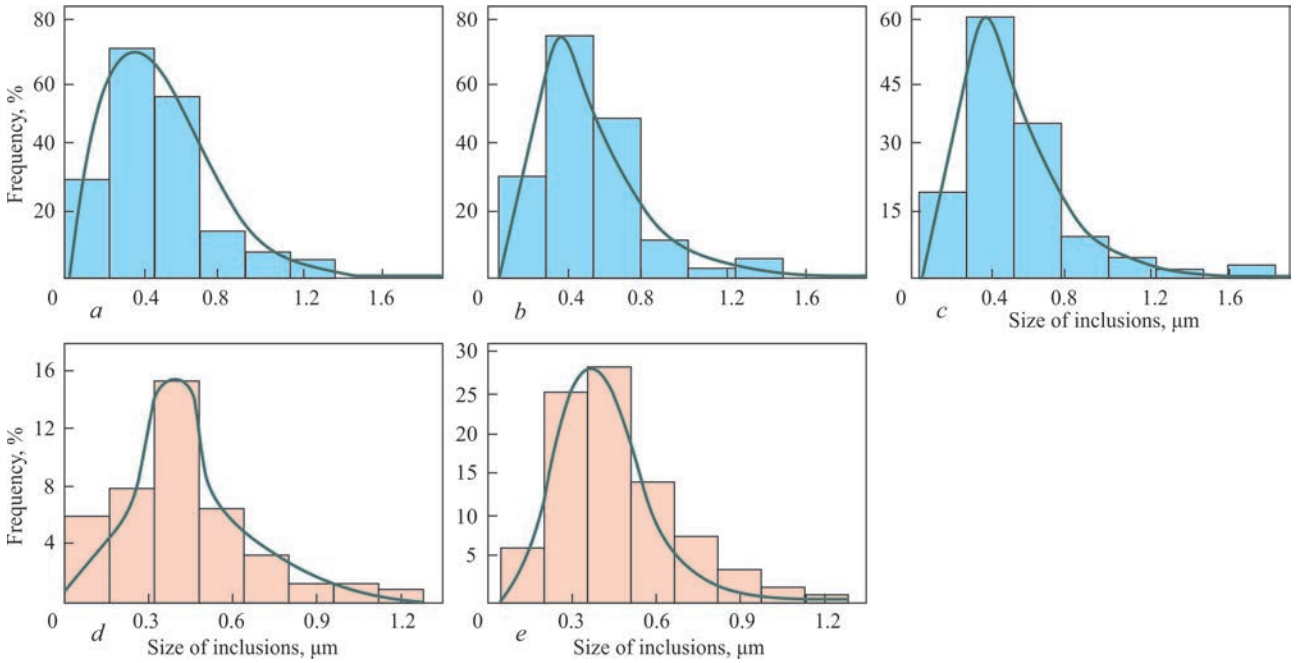
Figure 1. Histograms of distribution of non-metallic inclusions by sizes according to the results of submerged arc welding and corresponding calculated curve of probability density function according to the gamma-distribution: *a–c* — input energy of welding 36 kJ/cm; *d, e* — 21; *a* — weld NN1; *b* — NN2; *c* — NN3; *d* — NN4; *e* — NN5

At the beginning of the process of coarsening non-metallic inclusions, their distribution by sizes is subjected to the exponential law, since the vast majority of them have small radii close to the critical.

In the process of coarsening due to coagulation, a relative number of inclusions of small radii decreases, and large — increases, which leads to the change in the shape of the distribution function from a monotonically descending one, corresponding to the exponential distribution by sizes, to a single-modal one (with the maximum), corresponding to the gamma-distribution.

Thus, at the moment of beginning of the process (time variable $t = 0$), the shape parameter $\alpha = 1$, and at the end of the process, according to our experimental and calculation data, it acquires a value from the range of 2.33–4.15 (Table 2).

Denoting the final value of the shape parameter by α_k and considering the shape parameter as a linear function of time $\alpha(t)$, we obtain the following dependence of the shape parameter on time:

$$\alpha(t) = \frac{\alpha_k - 1}{t_k} t + 1,$$
(7)

where t_k is the final value of time.

Therefore, for further evaluation calculations to analyze the distribution of non-metallic inclusions by the size in submerged arc welding, the value $\alpha_k = 3$ can be set, which is approximately the average point of the interval of changing the shape parameter in this case.

Let us assume the duration of the process under the specified welding conditions as $t_k = 3.5$ s, which follows from the results of modeling the growth of non-metallic inclusions in the weld pool metal.

Then, from the equation (7) the following equation follows to describe the dependence of the shape parameter on time:

$$\alpha(t) = \frac{4}{7} t + 1.$$
(8)

As far as the nucleus of the formed non-metallic inclusions are the nuclei of refractory oxides of the chemical composition Al_2O_3, we should further use the following values: density of steel $\rho_s = 7.15 \cdot 10^3$ kg/m³; density of non-metallic inclusion (equal to the density of alumina) $\rho_{inc} = 3.97 \cdot 10^3$ kg/m³; $X_O = 47.1$ % of the total amount of oxygen in the molten metal $[O\%] = 0.055$.
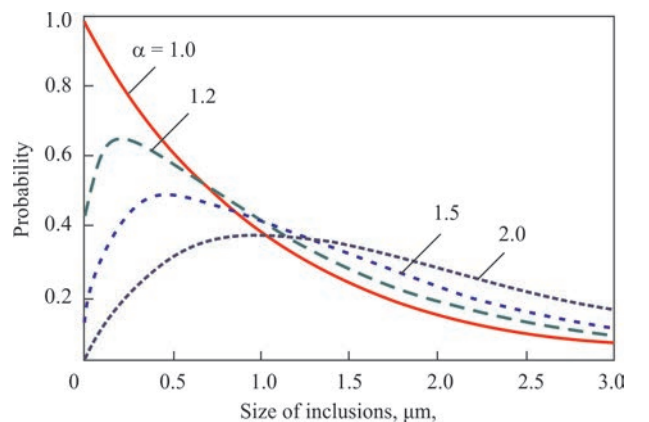
Figure 2. Change in behaviour of the gamma-distribution probability density function depending on the value of shape parameter α

Table 2. Experimental values of shape and scale parameters for submerged arc welding

Measurement code	NN1-1	NN1-2	NN1-3	NN1-4	NN1-5
Shape parameter	3.52979	2.90481	3.00837	2.81644	2.66076
Scale parameter, 10^{-6} m	7.40262	6.53177	6.51605	5.73114	4.94883
Measurement code	NN2-1	NN2-2	NN2-3	NN2-4	NN2-5
Shape parameter	2.99376	3.25676	3.19255	3.41001	2.68183
Scale parameter, 10^{-6} m	5.39726	5.99253	6.24691	6.57369	4.99286
Measurement code	NN3-1	NN3-2	NN3-3	NN3-4	NN3-5
Shape parameter	2.65562	3.30154	3.63677	3.4343	3.17487
Scale parameter, 10^{-6} m	5.12298	6.35464	6.36239	6.75384	5.51374
Measurement code	NN4-1	NN4-2	NN4-3	NN4-4	NN4-5
Shape parameter	3.94454	2.88799	2.74705	3.44743	2.33062
Scale parameter, 10^{-6} m	8.89796	5.50171	6.3869	7.40532	4.2632
Measurement code	NN5-1	NN5-2	NN5-3	NN5-4	NN5-5
Shape parameter	2.60281	4.14994	3.6945	3.54269	3.40696
Scale parameter, 10^{-6} m	548739.	8.26347	7.54531	7.70252	7.81811

Note. Shape and scale parameter was calculated by the formulas (7) and (13), respectively.

Then, the expression (5) takes the form

$$n_0 = \frac{1}{8 \cdot 3.1415926} \cdot \frac{7.15 \cdot 10^3 \cdot 0.02}{3.97 \cdot 10^3 \cdot 47.1} \lambda^4 =$$
$$= 0.83677 \cdot 10^{-4} \lambda^4. \tag{9}$$

Obviously, the value inverse to λ in the expression (1) is exactly a scale parameter. Therefore, let us rewrite $\beta = 1/\lambda$ in the entered symbols and the equation (1)

$$n(r) = n_0 \exp\left(-\frac{r}{\beta}\right) = n_0 \beta \frac{1}{\beta} \exp\left(-\frac{r}{\beta}\right) =$$
$$= n_0 \beta f(x;1,\beta), \tag{10}$$

from which it follows for the set values of parameters:

Figure 3. Change in distribution of non-metallic inclusions in time t in the conditions of lack of the formation of new nuclei of inclusions during the process

$$n(r) = 0.30428 \cdot 10^{-4} \lambda^3 f(x;1,\lambda^{-1}) =$$
$$= 0.83677 \cdot 10^{-4} \beta^{-3} f(x;1,\beta). \tag{11}$$

Dependence (11) describes the initial distribution of non-metallic inclusions in submerged arc welding by size. It is naturally that the dependence of the desired distribution on time is given in the form:
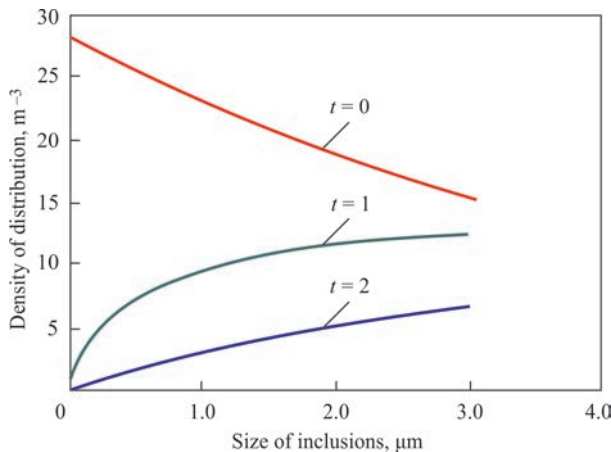
$$n(r,t) = 0,83677 \cdot 10^{-4} \beta^{-3} f(x;\alpha(t),\beta(t)), \tag{12}$$

where we will also consider the scale parameter as a linear function on time with finite values, corresponding to the values of the shape parameter from Table 1:

$$\beta(t) = \beta_0 + \frac{\beta_k - \beta_0}{t_k} t. \tag{13}$$

The obtained formulas allow using a tool of electron tables to calculate the distribution of non-metallic inclusions in a discrete volume of metal by sizes depending on time (Figure 3). The results shown in the diagram correspond to the data of [11].

Considering the real process, it is necessary, as is noted in [9], to take into account the formation of nuclei of non-metallic inclusions at a certain temperature depending on the rate of their formation and time spent in a set temperature range. Thus, the evaluation of the distribution density of non-metallic inclusions is obtained as the sum of products of the mentioned rates by the corresponding values of the time variable.

The final result is presented in Figure 3. It is seen that the gamma-distribution provides an objective description of the density function of the probability of distribution of non-metallic inclusions by sizes independent of the time of existence of the liquid metal in the welding pool and the chemical composition of the molten metal.

CONCLUSIONS

1. It was established that processing of experimental data on the sizes of non-metallic inclusions in the metal of welds deposited by submerged arc and shielding gas welding, showed that the final distribution of the studied inclusions by sizes is subjected to the law of gamma-distribution (probability is > 95 %).

2. It is shown that to describe the evolution of distribution of non-metallic inclusions during weld formation, it is advisable to use a probability model in the form of gamma-distribution with time-dependent parameters.

3. At the beginning of the process, the distribution of non-metallic inclusions in the proposed model is exponential due to the fact that the value of the shape parameter is equal to one. The values of the shape and scale parameters, calculated from the experimental data, are 2.6–3.9 and 4200–8900, respectively, regardless of the type of welding.

REFERENCES

1. Oh, Y.J., Lee, S.Y., Byun, J.S. et al. (2000) Non-metallic inclusions and acicular ferrite in low carbon steel. *Materials Transact., JIM*, 41(**12**), 1663–1669.
2. Quintana, M.A., McLane, J., Babu, S.S., David, S.A. (2001) Inclusion formation in self-shielded flux cored arc welds. *Welding J.*, **4**, 98–105.
3. Babu, S.S. (2004) The mechanism of acicular ferrite in weld deposits. *Current opinion in solid state and materials science*, **8**, 267–278.
4. Lee, T.K., Kim, H.J., Kang, B.Y., Hwang, S.K. (2000) Effect of inclusion size on the nucleation of acicular ferrite in welds. *ISIJ Int.*, 40(**12**), 1260–1268.
5. Zhang, J., Lee, H.G. (2004) Numerical modeling of nucleation and growth of inclusions in molten steel based on mean processing parameters. *Ibid.*, 44(**10**), 1629–1638.
6. Kwon, Y.-J., Zhang, J., Lee, H.-G. (2008) A CFD-based nucleation-growth-removal model for inclusion behavior in a gas-agitated ladle during molten steel deoxidation. *Ibid.*, 48(**7**), 891–900.
7. Njzawa, H., Kato, Y., Sorimachi, K., Nakanishi, T. (1999) Agglomeration and flotation of alumina clusters in molten steel. *Ibid.*, 39(**5**), 426–434.
8. Zinngrebe, E., Van Hoek, C., Visser, H. et al. (2012) Inclusion population evolution in Ti-alloyed Al-killed steel during secondary steelmaking process. *Ibid.*, 52(**1**), 52–61.
9. Hong, T., Debroy, T., Babu, S.S., David, S.A. (2000) Modeling of inclusion growth and dissolution in the weld pool. *Metallurgical and Materials Transact.: B., 20B*, **2**, 161–169.
10. Zhang, L., Thomas, B.G. (2003) Inclusion nucleation, growth, and mixing during steel deoxidation. UIUC. *Continuous Casting Report*, **200206**, 1–19.
11. Zhang, B.W., Li, B.W. (2007) Growth kinetics of single inclusion particle in molten melts. *Acta Metallurgica Sinica*, 20(**2**), 129–138.
12. *Lucas J.* van Vliet, Ian T. Young, Piet, W. (1998) Verbeek Recursive Gaussian Derivative Filters Fac. of Appl. Phys., Delft Univ. of Technol. DOI: 10.1109/ICPR.1998.711192. Conference: Pattern Recognition. In: *Proc. of Fourteenth Int. Conf.*, Vol. 1.
13. Gradshtejn, I.S., Ryzhik, I.M. (1971) *Tables of integrals, sums, series and products*. Moscow, Nauka [in Russian].
14. Golovko, V.V., Pokhodnya, I.K. (2013) Effect of non-metallic inclusions on formation of structure of the weld metal in high-strength low-alloy steels. *The Paton Welding J.*, **6**, 2–10.

ORCID

V.V. Holovko: 0000–0002–2117–0864

CONFLICT OF INTEREST

The Authors declare no conflict of interest

CORRESPONDING AUTHOR

V.V. Holovko
E.O. Paton Electric Welding Institute of the NASU
11 Kazymyr Malevych Str., 03150, Kyiv, Ukraine
E-mail: v_golovko@ukr.net

DECEMBER 22, 2007 French carrier rocket Ariane 5 launched the first ever African satellite. To create Ariane 5, the engineers supervising welding of the fuel tank for the rocket, made it from aluminium 3 mm thick. The welding unit was rotating inside the tank that allowed conducting seamless welding. The weld integrity is of critical importance, as cryogenic tanks form the load-carrying structure of the carrier rocket first stage. In addition, KUKA welding robots were used to build the rocket, which also ensured seamless welding.

STABILITY OF THE PROCESS OF ELECTROSLAG WELDING WITH BIFILAR POWER CIRCUIT WITHOUT EQUALIZING WIRE

Yu.M. Lankin, V.G. Soloviov, V.G. Tyukalov, I.Yu. Romanova

E.O. Paton Electric Welding Institute of the NASU
11 Kazymyr Malevych Str., 03150, Kyiv, Ukraine. E-mail: hhsova@gmail.com

Electroslag welding (ESW) by wire electrodes with bifilar circuit of power connection without equalizing wire is not applied now. There is reason to believe that bifilar ESW without the equalizing wire has certain advantages over bifilar electroslag remelting (ESR) without equalizing wire. Therefore, additional studies of the process of bifilar ESW without equalizing wire are required. Investigations were performed and the range of parameters of a stable process of ESW with bifilar power circuit without equalizing wire was determined, using a mathematical experiment. The causes for process unbalance can be temporary violation of the feed rate of one of the electrodes, local change of electrode cross-section, asymmetrical arrangement of the electrodes in the slag pool, etc. The notion of "resistance to external factors (REI) was introduced. It was proposed to use as the measure of resistance, the maximum value of REI parameter, above which the process goes into an unstable mode. REI nomogram was obtained, depending on welding voltage and electrode feed rate, which allows selection of the mode of bifilar ESW with the highest resistance to external disturbances. A mathematical model was used to show that the process of bifilar ESW without equalizing wire can run in a stable manner in a certain zone of values of the technological mode parameters.

KEY WORDS: electroslag welding, bifilar circuit, slag pool, metal pool, electric conductivity

INTRODUCTION

In 1960s PWI developed a new process of electroslag remelting (ESR) — so-called bifilar electroslag remelting. The essence of the process consists in that in a bifilar furnace two consumable electrodes are connected is series to the secondary winding of a single-phase transformer. It was proved that bifilar electroslag remelting has more advantages over the canonical two-electrode monofilar ESR [1], as the units operating by this scheme consume less power, are more efficient and have a higher power factor. Their advantages are especially great in production of slab ingots and plate ingots. However, alongside the advantages (such as favourable position of the zones of the main heat evolution in the slag pool, reduction of reactance of furnace loading), a bifilar ESR furnace without equalizing wire turned out to be operationable only in a certain range of remelting modes, as a result of ineffective self-regulation. That is, the process became unstable at certain short-term external distances acting on it. To eliminate this drawback with preservation of ESR bifilar circuit advantages, the secondary winding of the supply transformer is made with a midpoint, connected to the workpiece to be welded by equalizing wire.

As regards bifilar ESW with wire electrodes without equalizing wire, such a technology has not been used up to now. There is ground to believe that bifilar ESW without equalizing wire has certain advantages over bifilar ESR without equalizing wire. As the

sectional area of consumable electrodes in ESW and ESR differs considerably, the thermophysical processes causing their melting also differ essentially. Analysis of the pattern of current spreading in the slag pool of ESR bifilar furnace without equalizing (zero) wire [1] was performed by a simplified two coordinate (2D) electric circuit. Here, current spreading along the workpiece edges and shoes was not taken into account. The proposed ratio of current flowing through the slag and the metal pool (10–30 %) and current, flowing only between the electrodes in the slag pool (90–70 %), requires more precise determination in 3D dimension. Therefore, additional studies of the process of bifilar ESW without equalizing wire are required. New data will result in corrections in the range of parameters for a stable ESW process.

The objective of this work is study and determination of the parameter range of a stable process of ESW with bifilar power circuit without equalizing wire, using mathematical experiment.

The mathematical experiment was performed with application of an earlier developed model [2]. In the mentioned work mathematical experiments were conducted with two-electrode ESW, connected to a power source by monofilar and bifilar circuits with equalizing wire. In order to study the distribution of the electric field, current and potential in the slag pool, workpiece being welded, the forming weld, and the shoes, as well as heat distribution in the studied zone volume, its finite element model was used, which consisted of a slag and metal pools, two shoes, two electrodes, immersed into the slag pool, as well as fragments of the

workpiece and the weld. In connection with the fact that the circuit of welding equipment connection to the power source creates external conditions for the model and does not change either graphic, or physical characteristics of the model of the studied ESW zone, a decision was taken to use this model for conducting a mathematical experiment in the study and determination of the parameters of a stable ESW process with bifilar power circuit without equalizing wire. Here, the cables of the transformer secondary winding are insulated from the grounding terminal of the power source. ESW power supply circuit is shown in Figure 1.

With bifilar power circuit of ESW without equalizing wire, the current in the slag pool flows in two generalized circuits: "electrode e1 – slag pool – electrode e2"; "electrode e1 – slag pool – workpiece – slag pool – electrode e2". It is understood that the current flowing in the workpiece, is the current passing through the metal pool, workpiece edges and shoes. The current in each of the above-mentioned circuits depends on their electric conductivity, which, in its turn, depends on the flux composition, used metal grades, as well as on the temperature state of each elementary volume of this zone of the welding process, through which the current flows. The potential of both the workpiece edges, shoes, weld and metal pool is of practically equal importance, in view of their low specific resistance, compared to higher specific resistance of the slag pool. More over, for the purpose of electrical safety of service personnel, the ESW unit and the workpiece are grounded.

At the change of ESW supply voltage and/or rate of electrode feeding into the slag pool, the depth of electrode immersion and their melting rate are also changed. Here, the conductivity of each of the above-mentioned circuits and the distribution of the amount of heat, evolving in the slag, are changed. In connection with the fact that the same current flows in both the electrodes in the bifilar circuit, a feedback forms between the processes of self-regulation of melting rate of each of them. Therefore, for the bifilar circuit it is important to maintain a balance between the electrode melting rates, as the change of self-regulation feedback in the electrodes from the negative to the positive one can lead to instability of ESW process. The causes for the unbalance can be temporary violation of the feed rate of one of the electrodes, local change of electrode section, asymmetrical arrangement of the electrodes in the slag pool, etc. Figure 2 gives an example of asymmetrical running of ESW process.

In order to understand the nature of the change of electrical characteristics of the electroslag process
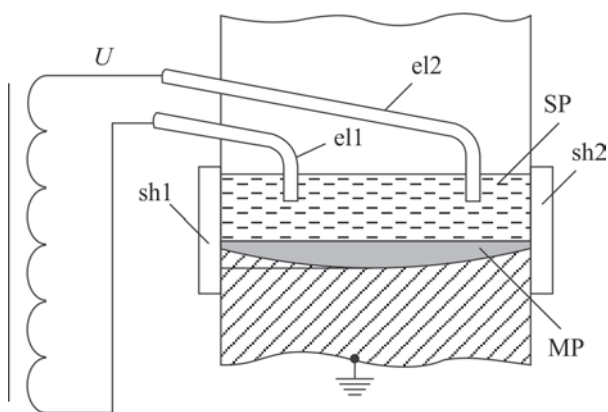

Figure 1. ESW two-electrode bifilar power circuit without equalizing wire (U — power source voltage; e1 and e2 — consumable electrodes; sh1 and sh2 — water-cooled shoes; SP, MP — slag and metal pools)

when different disturbances are introduced into it, for instance, at the change of the rates of electrode feeding into the slag pool, a physical experiment on bifilar ESR into a graphite casting mould was conducted in the laboratory conditions at PWI using AD-381Sh machine [3]. Remelting was performed with bifilar circuit of power source connection without equalizing wire with a grounded stand. Technological parameters of experimental remelting were as follows: mould internal dimensions of 80×30 mm, electrode spacing of 40 mm (at symmetrical arrangement of the electrodes relative to each other); slag pool depth of 50–70 mm; electrode wire diameter of 3 mm; number of electrodes — 2.

The testing objective was to perform continuous saving on electronic carrier of such parameters as feed rate of electrode e1 – V_{f1}, feed rate of electrode e2 – V_{f2}, voltage between the nozzle of electrode e1 and workpiece U_1, voltage between the workpiece and nozzle of electrode e2 – U_2, as well as power source current I_w, while changing the feed rate of electrode e2 in a certain range during the remelting process (at
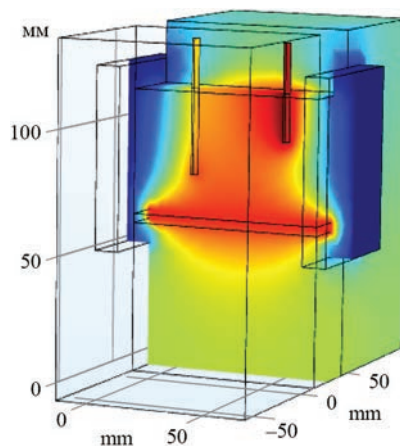
Figure 2. Fragment of the graphic part of the model (sectional view) at the developed asymmetry of ESW process
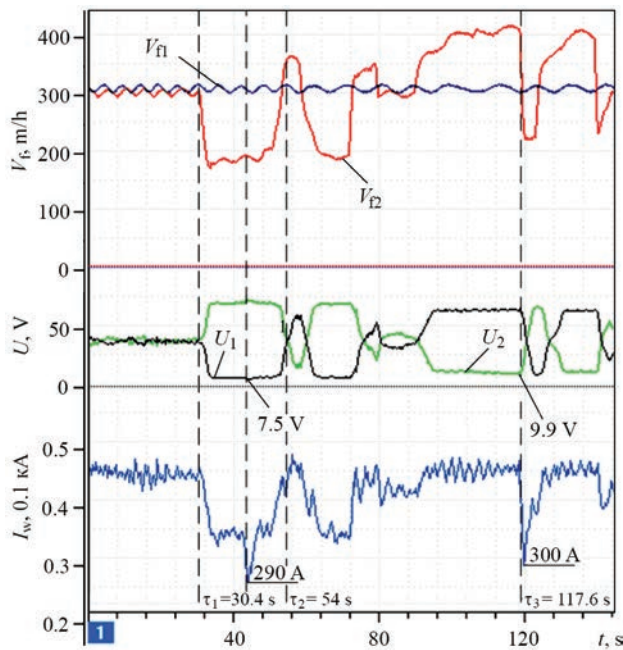
Figure 3. Dependencies of the change of ESW parameters in time with simulation of external disturbances

unchanged feed rate of electrode e1) at supply voltage $U = 85$ V (Figure 3).

One can see in Figure 3 how the voltage between the electrodes and workpiece U_1 and U_2 changes at the change of V_{f2}. The sum of these voltages is equal to power source voltage of 85 V. In the range of $\tau_1 - \tau_2$, V_{f2} is smaller than V_{f1}, resulting in shallower immersion of electrode e2 (Figure 2), lower conductivity of "electrode e2 – workpiece" channel, lower power source current, and higher voltage U_2 between electrode e2 and workpiece. Voltage between electrode e1 and workpiece $U_1 = U - U_2$ decreases accordingly. In this time range at low V_{f2}, voltage U_1 reaches a critically small value of 7.1 V. Here, electrode e2 reaches minimum immersion into the slag pool and current I_w drops abruptly from 350 to 290 A. A similar situation is observed at moment of time τ_3, when electrode e1 reaches a minimum of immersion into the slag pool at critical value of voltage $U_2 = 9.9$ V. Here, current I_w drops abruptly from 460 to 300 A.

This physical experiment showed that violation of the process stability can occur at certain combinations

of the values of electroslag process parameters and external disturbances. For a technologist, developing the melting process, it is important to know the working zone of parameter values and the level of process resistance to external disturbances. We will introduce the notion characterizing the electroslag process with bifilar power circuit without equalizing wire — "resistance to external factors". It is recommended to use as the measure of resistance, the maximum value of REI parameter, above which the process goes into unstable mode. REI is determined as follows:

$$\Delta U = \left| U_1 - U_2 \right|; \; rei = \left| \frac{\Delta U}{U} \right| \cdot 100 \, \%,$$

where rei is the intermediate value of the external factor, %; REI = max (rei) is the limit of the mode of stable running of the process. A stable mode is found in the range of $0 \le rei < REI$.

At bifilar ESW any external action, leading to unbalance of electrode melting rates, always leads to value $\Delta U > 0$. Therefore, in the computational experiment the unbalance can be assigned in the model by changing ΔU, as a source of unbalance, which is universal.

For the computational experiment the following model parameters were taken: $U = 85$ V; $V_{f1} = 280$ m/h; workpiece thickness of 80 mm; gap width of 30 mm; slag pool depth of 50 mm; electrode spacing of 40 mm; workpiece material was 09G2S steel; electrode wire was Sv.08G2S steel; flux was AN-8; forming shoes were from copper. Physical properties of the materials are given in the Table 1 [4].

Parameters $C\rho[T]$, $\rho[T]$, $k[T]$, $\alpha[T]$, $\sigma_{st}[T]$, $\sigma_{sh}[T]$ were set by the respective approximating dependencies on temperature T, K (not given in the paper).

Computational experiment yielded maximum values of short-term disturbance. The limit was found, at which the feedback between the processes of self-regulation of melting rates of both the electrodes changes from the negative to positive one (Figure 4).

Maximum value of disturbance, above which the process goes into an unstable condition, is equal to $\Delta U = 14.4$ V. At $U = 85$ V the stability value should be:

Table 1. Physical properties of materials used in the model

Parameter	Workpiece	Electrodes	Slag	Shoes	Weld
Heat capacity ($C\rho$), J/(kg·K))	$C\rho[T]$	$C\rho[T]$	1400	385	$C\rho[T]$
Relative dielectric permeability (ε)	1	1	2.5	1	1
Density (ρ), W/(m·K)	$\rho[T]$	$\rho[T]$	2600	8960	$\rho[T]$
Thermal conductivity (k), W/(m·K)	$k[T]$	$k[T]$	295	400	$k[T]$
Thermal expansion coefficient (α), l/K	$\alpha[T]$	$\alpha[T]$	–	17E-6	$\alpha[T]$
Specific electric conductivity (σ) S/m	$\sigma_{st}[T]$	$\sigma_{st}[T]$	$\sigma_{sh}[T]$	6E7	$\sigma_{st}[T]$
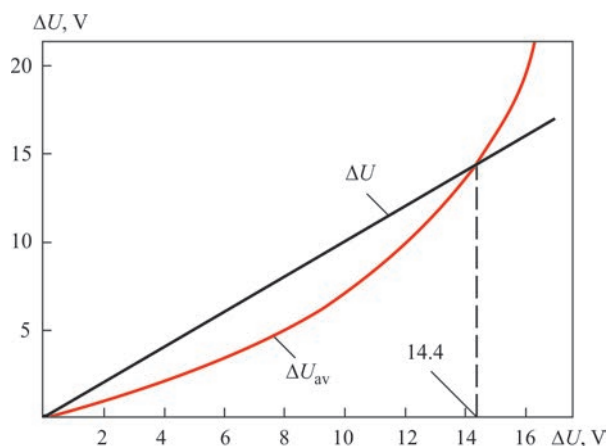
Figure 4. Result of self-regulation of electrode melting rates (ΔU — disturbance value, V; ΔU_{av} — respective reaction of the process as a result of self-regulation of electrode melting rates, V)

$$\text{REI} = \frac{14.4}{85} \cdot 100\,\% = 19.9\,\%.$$

At long-term action of an external factor, the value of which is smaller than REI, the process will go into a stable mode with different depth of electrode immersion into the slag pool, leading to thermal field asymmetry and may lead to violation of the uniformity of workpiece edge penetration.

The created model was used for computation of REI for different combinations of U and V_f values. REI = $F[U, V_f]$ nomogram was derived (Figure 5), which allows selection of the mode of bifilar ESW without equalizing wire with the highest resistance to the action of external disturbances. During REI computation, the following constraints were set for the model, at which the process of bifilar ESW should, probably, be more stable:

• temperature of lower electrode faces does not go beyond 1500–2000 °C;

• electrode immersion depth stays within 2–48 mm;

• presence of negative feedback between the processes of self-regulation of both the electrodes is mandatory.

Study of the conditions of current spreading in the slag pool and the workpiece, conducted using the model, showed that, depending on ESW mode (voltage, electrode feed rate, welding zone geometrical parameters, electrode arrangement in the slag pool) from 33 to 85 % of current flows between the electrodes through the slag pool, while the other part of current (15–67 %) passes through the slag and the workpiece, including the shoes. It leads to the assumption that for modes of bifilar ESW without equalizing wire, characterized by considerable currents, flowing through the workpieces, the influence of feedback between self-regulation of each of the electrodes will be reduced, and it will allow
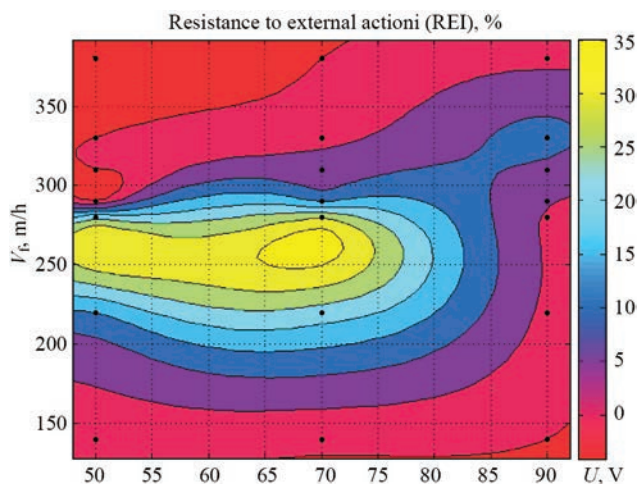
Figure 5. Nomogram of resistance of bifilar ESW process

widening the range of ESW process stability. It can be the subject of further studies.

CONCLUSIONS

1. For ESW bifilar circuit it is important to keep a balance between the processes of melting of both the electrodes. The causes for unbalance can be temporary violation of feed rate of one of the electrodes, local change of electrode cross-section, asymmetrical arrangement of electrodes in the slag pool, etc.

2. The notion of "resistance to external factors" for bifilar ESW without equalizing wire was introduced. As the measure of resistance, it is proposed to use the maximum value of REI parameter, above which the process goes into an unstable mode.

3. REI nomogram depending on welding voltage and electrode feed rate was derived, which allows selection of bifilar ESW mode with the greatest resistance to the action of external disturbances.

4. Using the mathematical model, it was shown that the process of bifilar ESW without equalizing wire can run in a stable manner in a certain zone of technological mode parameters.

5. The developed model can be used to predict the parameters of a stable process of bifilar ESW after physical model testing.

REFERENCES

1. (1976) *Electroslag furnaces. Ed. by B.E. Paton, B.I. Medovar.* Kiev, Naukova Dumka [in Russian].
2. Lankin, Yu.M., Soloviov, V.G., Tyukalov, V.G., Romanova, I.Yu. (2021) Comparison of electroslag welding processes at power connection with two-electrode conventional and bifilar diagram. *The Paton Welding J.*, **11**, 40–43. DOI: https://doi.org/10.37434/as2021.11.05
3. Lankin, Yu.N., Moskalenko, A.A., Tyukalov V.G. et al. (2008) Application of electroslag welding in construction and repair of metallurgical installations. *Svarshchik*, **1**, 6–9 [in Russian].
4. (1989) *Grades of steels and alloys*. Ed. by V.G. Sorokin. Moscow, Mashinostroenie [in Russian].

ORCID
Yu.M. Lankin: 0000-0001-6306-8086,
V.G. Soloviov: 0000-0002-1454-7520,
V.G. Tyukalov: 0000-0003-3491-193X,
I.Yu. Romanova: 0000-0001-7154-1830

CONFLICT OF INTEREST
The Authors declare no conflict of interest

CORRESPONDING AUTHOR
Yu.M. Lankin
E.O. Paton Electric Welding Institute of the NASU
11 Kazymyr Malevych Str., 03150, Kyiv, Ukraine
E-mail: lankin.y.n@gmail.com

JOURNAL HOME PAGE
https://pwj.com.ua/en

PRODUCING AND PROPERTIES OF DETONATION COATINGS BASED ON FeMoNiCrB AMORPHIZING ALLOY WITH ADDITION OF STRENGTHENING PHASES

Yu.S. Borysov, A.L. Borysova, T.V. Tsymbalista, A.I. Kildiy, K.V. Yantsevych, Z.G. Ipatova

E.O. Paton Electric Welding Institute of the NASU
11 Kazymyr Malevych Str., 03150, Kyiv, Ukraine

ABSTRACT

The structure and properties of amorphizing composite detonation coatings based on FeMoNiCrB alloy were studied. FeMoNiCrB + ZrB_2, FeMoNiCrB + (Ti, Cr)C, FeMoNiCrB + $FeTiO_3$ composite powders were used for coatings deposition, which were produced from a mixture of the composition powders by mechanical alloying. It is found that as a result of detonation spraying of all the powder compositions, the formed coatings have dense, lamellar, multiphase structure. The coating composition includes Fe(Ni, Cr) solid solutions, Mo_2FeB_2 and Fe_2B borides, dispersed inclusions of alloying additives (ZrB_2, (Ti, Cr)C, $FeTiO_3$) and oxides (ZrO_2 and $FeCr_2O_4$ or Fe_2O_3, or Fe_3O_4), as well as an amorphous phase, the amount of which in the coating structure has increased, as a result of the detonation spraying process. The values of microhardness, corrosion resistance, fatigue life and wear resistance of the composite detonation coatings are given.

KEY WORDS: detonation spraying, composite powders, amorphizing iron alloy, zirconium boride, titanium-chromium carbide, iron titanate, coating, corrosion resistance, wear resistance

INTRODUCTION

The complex of special physicochemical and mechanical characteristics found in materials with amorphous structure, opened broad prospects for their practical use for development of protective coatings operating in the conditions of higher wear and corrosion, as well as for coatings with special properties (magnetic, resistive, radiation resistant, etc.) [1–3].

One of the methods of producing coatings with amorphous structure is thermal spraying of coatings [3].

An important advantage of thermal spraying (TS) in the production of metallic materials with amorphous structure (MMA) over other methods (melt spinning, melt extrusion, producing of thin layers of MMA using laser, evaporation in vacuum, magnetron spraying, etc.), which allow producing foils, strips with a thickness of not more than 10–150 μm, is the possibility of forming layers of coating material with an amorphous structure of up to several mm thickness. The basis of the technology of TS coatings with amorphous structure consists in providing the cooling rate of the melt particles of the sprayed material at the moment of forming the coating on the surface of the base of not lower than the critical value that is characteristic of each amorphizing alloy. Most of such Ni-, Fe- and Co-based alloys have the following characteristics in the range of 10^5–10^6 K/s [1, 3], which is possible to provide in TS conditions by appropriate selection of sizes of the sprayed particles, parameters of the spraying process and cooling system of a product on which the coating is sprayed, when using almost all TS methods (flame, plasma and detonation).

However, in flame and plasma spraying, the direct effect of a high-temperature gas jet on the sprayed surface requires the development of special cooling conditions of the spraying zone to avoid reduction in the rate of temperature drop of the sprayed particles below the required one. In this regard, the conditions of detonation spraying are more favorable to provide the cooling rates of the melt of the sprayed particles, necessary for the formation of the amorphous state of the sprayed coating structure. On the other hand, higher velocities of melt particles during detonation spraying at the moment of their hitting against the surface of the base, lead to the formation of deformed weave particles of smaller thickness, which provides higher cooling rates of the sprayed material and promotes amorphization of the coating material.

The accumulated experience of detonation spraying of amorphous coatings showed the prospects and effectiveness of their practical application for restoration of parts of internal combustion engines (ICE) $Fe_{69}B_{15}C_{10}Si_6$, $Fe_{70}Cr_{10}B_{20}$, $Fe_{70}Cr_{10}P_{13}C_7$), strengthening of parts of metal-cutting machines and the stamp tool ($Fe_{61}B_{37}C_2$, $Fe_{67}Ti_7B_{24}C$, Ni_3B), for protection of parts of chemical mechanical engineering against wear and corrosion ($Fe_{70}Cr_{10}P_{13}C_7$, $Ni_{40}Ti_{40}Si_{20}$) [3]. One of the directions of further development of technologies of detonation spraying of coatings with amorphous structure, which can lead to increase of their service properties and expansion of areas of application, is the development of detonation composite coatings on the basis of alloys with amorphous structure.

The aim of the work was to study the process of structure formation and to determine the properties of detonation coatings from composite powders based

Table 1. Characteristics of source powders

Powder	Particles size, μm	Density ρ, g/cm³	Microhardness, MPa	Phase composition
FeMoNiCrB, (Fe – 36.2; Mo – 29.9; Ni – 23.6; Cr – 7.6; B – 2.7)	63–100	7.84	6170 ± 1170	Solid solution Fe(Ni, Cr), Mo_2FeB_2, Fe_2B, Cr_2B
FeMoNiCrB + ZrB_2	<80	7.42	6020 ± 1280	Solid solution Fe(Ni, Cr), Mo_2FeB_2, ZrB_2, APh
FeMoNiCrB + (Ti, Cr)C	<40	7.283	5650 ± 1100	Solid solution Fe(Ni, Cr), Mo_2FeB_2, (Ti, Cr)C, Cr_3C_2, APh
FeMoNiCrB + $FeTiO_3$	<80	7.52	5050 ± 660	Solid solution Fe(Ni, Cr), Mo_2FeB_2, $FeTiO_3$, APh

on FeMoNiCrB alloy with ZrB_2, (Ti, Cr)C and $FeTiO_3$ additives, produced by mechanical alloying.

OBJECTS OF STUDIES AND PROCEDURE OF EXPERIMENT

For detonation spraying of coatings, composite powders produced by mechanical alloying from a mixture of powder of amorphizing FeMoNiCrB alloy with 30 vol.% of refractory compounds ZrB_2, (Ti, Cr)C and $FeTiO_3$ were used. The method of producing composite powders is described in detail in [4], and their characteristics are presented in Table 1.

Detonation spraying of coatings was performed in the installation "Perun-S" using propane-butane as a detonating mixture (50 % C_3H_8 + 50 % C_4H_{10}) with oxygen in a ratio of 1:3 with the addition of air. As a transporting gas, air was used (Table 2). The spraying distance was constant — 110 mm, the frequency of cycles was 6.6 s^{-1}.

To study the structure and phase composition of the coatings, methods of metallography (microscope Neophot-32, equipped with the attachment for digital filming) were used; X-ray diffraction phase analysis (XDPA) was performed in a DRON-3 diffractometer in CuK_α radiation with a graphite monochromator at a step movement of 0.1° and exposure time at each point of 4 s with the subsequent computer processing of the obtained digital data. Phase identification was performed using the ASTM database.

Corrosion resistance of detonation coatings in the 10 % H_2SO_4, 3 % NaC1 and 5 % NaOH solutions was investigated by the potentiostatic method in the potentiostat P-5827 M at a scanning rate of 2 mV/s using a specially designed clamping cell that provides a one-sid-

ed access of the electrolyte to the coating and does not require protection of nonoperating surfaces. As a reference electrode, a silver chloride electrode filled with a saturated solution of potassium chloride was used, and as an auxiliary electrode, platinum served. Preparation of specimens before the corrosion tests was performed according to GOST R 9.905–2007 [5].

According to the experimental values, cathode and anode polarization curves were constructed in the coordinates:

$$E_c = f(\lg i_c),$$

where E_c is the corrosion potential, V; i_c is the current density, A/cm^2 [6, 7].

The rate and corrosion potential of coatings was determined graphically by polarization curves by extrapolation of Tafel regions of cathode and anode curves to $E = E_c$.

Using the values of corrosion currents determined according to the polarization curves, the weight and depth value of corrosion was calculated by the formulas [6]:

$$K_w = \frac{iA \cdot 1000}{nF},$$

where K_w is the weight index of corrosion, $g/m^2 \cdot h$; i is the current density, A/cm^2; A is the atomic weight of metal, g/mol; n is the valence of the metal ion that passed into the solution; F is the Faraday number (26.8 A·h/mol).

$$K_d = K_w = \frac{8.76}{\rho},$$

where K_d is the index of corrosion depth, mm/year; ρ is the metal density, g/cm³; 8.76 is the conversion fac-

Table 2. Conditions of spraying detonation coatings

Powder	Consumption of detonation mixture, m³/h			Consumption of transporting gas (air), m³/h
	Propane-butane C_3H_8 + C_4H_{10}	Oxygen	Air	
FeMoNiCrB	0.5	1.55	0.5	0.65
FeMoNiCrB + ZrB_2	0.5	1.55	0.9	0.35
FeMoNiCrB + (Ti, Cr)C	0.5	1.55	0.9	0.35
FeMoNiCrB + $FeTiO_3$	0.5	1.55	0.9	0.35

tor for transition from the weight index of corrosion to the calculation per 1 h to the depth index of up to 1 year, calculated from the number of hours per year (24 h·365 = 8760 h) and divided by 1000.

For the comparative characteristics of corrosion resistance, ten-point evaluation scale was used (GOST 13819–69), based on the use of depth index of corrosion (K_d) [6].

Wear resistance of coatings was studied in the conditions of abrasive wear by friction against a loosely fixed abrasive (GOST 23.208–79) [8]*. As an abrasive material for tests SiO$_2$ sand with a hardness of 11 GPa and B$_4$C carbide with a microhardness of 45 GPa were used; the particle size of the powders was 250–300 μm.

The index of wear resistance of the coating was evaluated by the loss of mass of the specimen after the experiment with an accuracy of 0.0001 g. For each type of coating, three specimens were tested.

The relative wear resistance (K_i) was evaluated by the formula [8]

$$K_i = \frac{G_e}{G_i} \frac{\rho_i}{\rho_e},$$

where ρ_e, ρ_i are the densities, and G_e, G_i is the loss of mass of reference and test materials, g.

As a reference specimen, steel 30KhGSA with the hardness HV 212–248 was used.

EXPERIMENTAL RESULTS AND DISCUSSION

The study of the microstructure of detonation coatings (Figure 1) showed that during spraying of both powders of the amorphizing FeMoNiCrB alloy as well as composite powders, the coatings are formed which are dense, uniform by thickness and with a lamellar structure, where alternation of light and dark lamellae

is observed. The values of microhardness of both dark and light lamellae vary in wide ranges (Table 3), and in general, its higher values for dark lamellae can be noted, where, probably, oxide inclusions are concentrated. If we compare the averaged values of microhardness of coatings depending on the composition, their higher values for CP with (Ti, Cr)C carbide unlike ZrB$_2$ borides and FeTiO$_3$ oxide can be noted. The same pattern occurs in the case of source CP (Table 1). However, the microhardness of the sprayed coatings appeared to be lower than of the source powders. The reason for this difference probably consists in the different content of the amorphous phase [9].

X-ray structure phase analysis of detonation coatings shows that during spraying of CP of all compositions, an amorphous-crystalline structure is formed, which is evidenced by large areas of "halo" on the X-ray patterns (Figure 2).

The study of the kinetics of electrode potentials of detonation coatings (Figure 3) showed that their values stabilize within 15–40 min after immersion of the specimens in the electrolyte. Thus, in a 3 % NaCl solution with the introduction of additives ZrB$_2$, (Ti, Cr)C, FeTiO$_3$, the shift of the corrosion potential (E_c) occurs to the more positive direction from –0.35 to –0.28 V and the cathodic reaction of hydrogen evolution inhibits. If in the case of coatings from FeMoNiCrB powder, corrosion currents are in the range of 4·10^{-6} A/cm^2, then with the introduction of additives, they are reduced for almost all coatings to 2–3·10^{-6} A/cm^2. The absence of passivation of the coating in 3 % NaCl medium may be predetermined by the fact that this solution belongs to the aggressive media with a high content of Cl-, the presence of which gradually displaces oxygen from the protective film to the electrode surface. At the same time, the anode process of forming the pro-

Table 3. Characeristics of detonation coatings

XDPA	Composition	H_μ^*, MPa	Characteristics of structure
APh, solid solution Fe(Ni, Cr), Mo$_2$FeB$_2$, Fe$_2$B, Fe$_2$O$_3$	FeMoNiCrB	4855 ± 1023	Dense homogeneous structure with hardly noticeable lamellarity and small amount of dark tiny (probably oxide) inclusions (Figure 1, a)
APh, solid solution Fe(Ni, Cr), Mo$_2$FeB$_2$, ZrB$_2$, Fe$_2$B, ZrO$_2$, FeCr$_2$O$_4$	FeMoNiCrB + ZrB$_2$	3830 ± 570	Dense fine-lamellar structure with alternating light and dark gray lamellae, whose microhardness differs slightly (respectively, 3270–4500 and 3040–5590 MPa) (Figure 1, b)
APh, solid solution Fe(Ni, Cr), Mo$_2$FeB$_2$, (Ti, Cr)C, Fe$_2$B, Fe$_2$O$_3$	FeMoNiCrB + (Ti, Cr)C	4450 ± 700	Dense lamellar structure with light inclusions of rounded shape, microhardness of which changes within the range from 3800 to 5700 MPa (Figure 1, c)
APh, solid solution Fe(Ni, Cr), Mo$_2$FeB$_2$, FeTiO$_3$, Fe$_2$B, Fe$_3$O$_4$	FeMoNiCrB + FeTiO$_3$	3750 ± 620	Dense fine-lamellar structure with light ($H\mu$ = 2220–4350 MPa) dark gray ($H\mu$ = 3000–3980 MPa) lamellae with a large number of both light and dark gray inclusions (Figure 1, d)
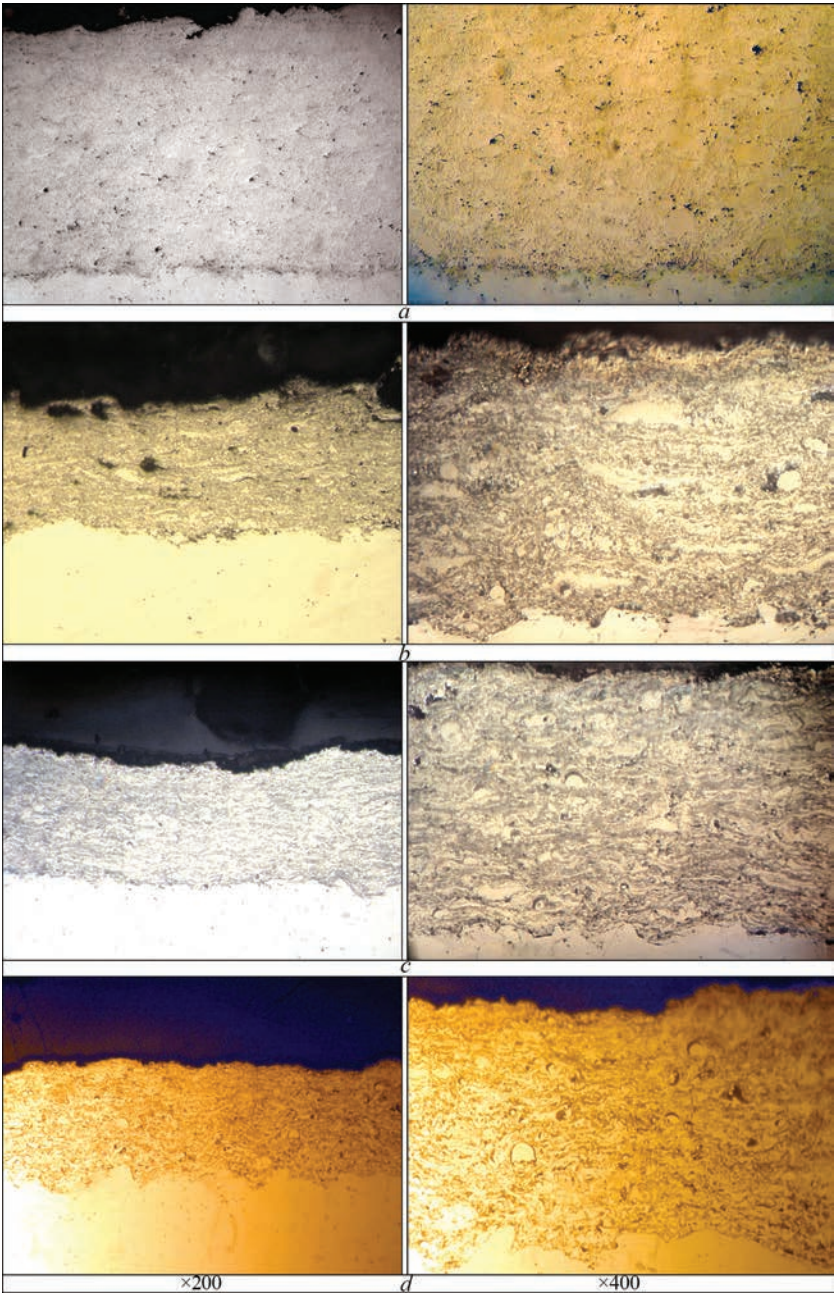
Figure 1. Microstructure of detonation coatings produced from powders FeMoNiCrB (*a*), FeMoNiCrB + ZrB$_2$ (*b*), FeMoNiCrB + (Ti, Cr)C (*c*), FeMoNiCrB + FeTiO$_3$ (*d*)

tective oxide is slowed down by the anodic process of formation of easily soluble compounds of metals with Cl- [10].

The study of the electrochemical behavior of detonation coatings in the 10 % solution of H$_2$SO$_4$ showed that the introduction of ZrB$_2$, (Ti, Cr)C, FeTiO$_3$ leads to the change of corrosion potential in a more positive direction from –0.12 to –0.044 V, corrosion processes occur with a hydrogen depolarization, corrosion currents are in the range of 1.6–1.8·10^{-5}A/cm^2. The obtained anode polarization curves indicate the absence of passivation of coatings in a wide range of potentials. Pure chromium and nickel in sulfuric acid are well passivated [11, 12], while in the coatings, whose source powder includes these metals, they do not

transfer into the passive state. This can be explained by the presence of the phases Mo$_2$FeB$_2$, ZrB$_2$, TiC in the layer structure, which are the cathodes relative to nickel and chromium. They prevent the formation of continuous oxide films on the surface of the coatings in the solution of sulfuric acid, as a result of which the system loses the ability to passivate.

Electrochemical studies of detonation coatings in the 5 % NaOH solution show that the introduction of additives ZrB$_2$, (Ti, Cr)C, FeTiO$_3$ shifts the corrosion potential in the positive direction from –0.48 to –0.34 V and reduces the corrosion currents from 5·10^{-6} to 2·10^{-6} A/cm^2.

Analysis of the results (Table 4) shows that for all the studied coatings, the maximum corrosion rate

Figure 2. X-ray patterns of detonation coatings produced from powders: FeMoNiCrB (*a*), FeMoNiCrB + ZrB$_2$ (*b*) FeMoNiCrB + (Ti, Cr)C (*c*), and FeMoNiCrB + FeTiO$_3$ (*d*)
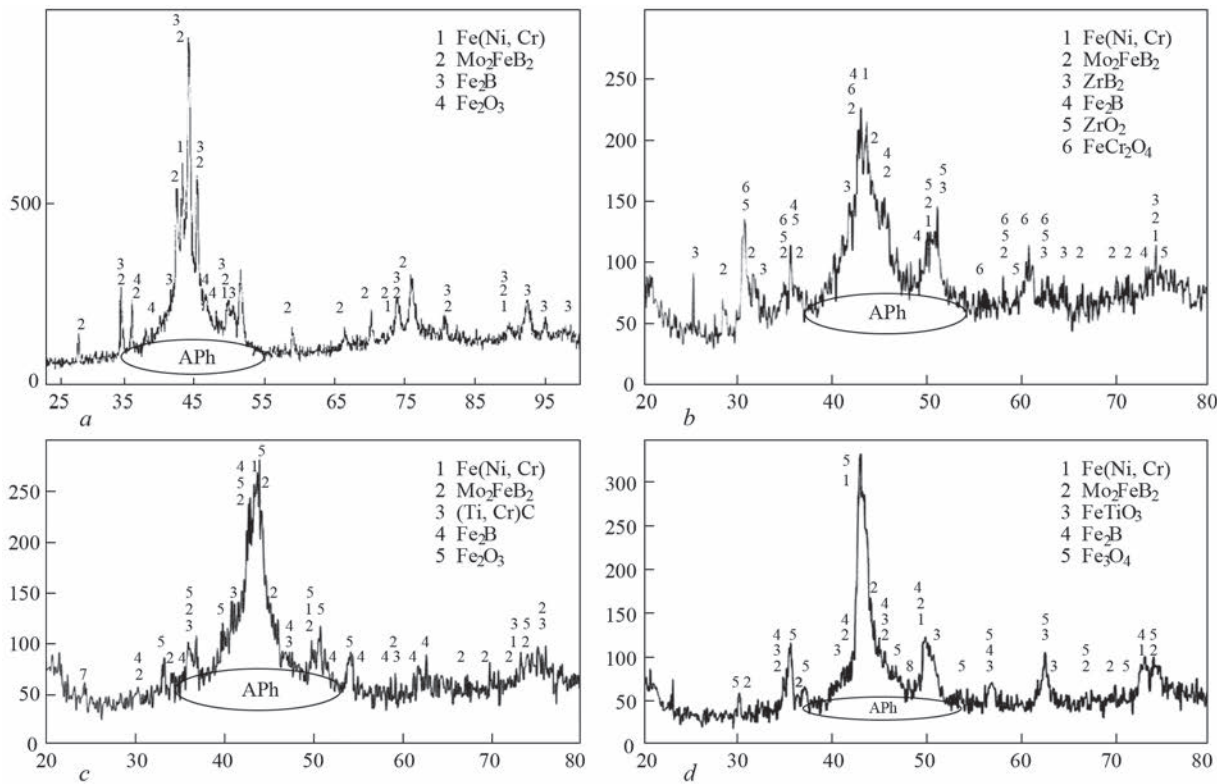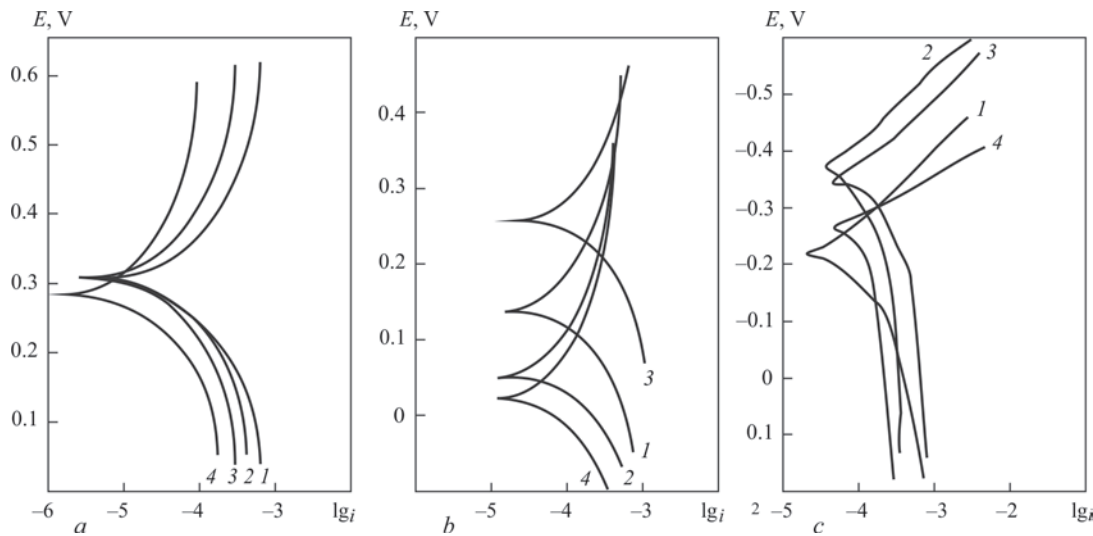

Figure 3. Polarization curves of detonation coatings: *a* — in 3 % NaCl; *b* — in 10 % H$_2$SO$_4$ solution; *c* — in NaOH (*1* — FeMoNiCrB; *2* — FeMoNiCrB + ZrB$_2$; *3* — FeMoNiCrB + (Ti, Cr)C; *4* — FeMoNiCrB + FeTiO$_3$)

Table 4. Results of electrochemical tests of detonation coatings (coating thickness is 500 μm)

Composition of coating	Electrolyte					
	3 % NaCl		5 % NaOH		10 % H$_2$SO$_4$	
	E_c, V	i_c, A/cm^2	E_c, V	i_c, A/cm^2	E_c, V	i_c, A/cm^2
FeMoNiCrB	−0.35	4·10^{-6}	−0.48	5·10^{-6}	−0.12	1.9·10^{-5}
FeMoNiCrB +ZrB$_2$	−0.31	2.5·10^{-6}	−0.34	2·10^{-6}	−0.24	1.5·10^{-5}
FeMoNiCrB + (TiCr)C	−0.33	3·10^{-6}	−0.33	3·10^{-6}	−0.08	1.6·10^{-5}
FeMoNiCrB + FeTiO$_3$	−0.28	3·10^{-6}	−0.44	3·10^{-6}	−0.04	1.8·10^{-5}

Table 5. Indices of corrosion resistance of detonation CP based on FeMoNiCrB

Composition of coating	Corrosion rate index		Service life, year	Point of corrosion resistance	Group of corrosion resistance
	K_w, g/м²h	K_d, mm/ year			
3 % NaCl					
FeMoNiCrB	0.042	0.047	10.6	4	Resistent
FeMoNiCrBi + ZrB₂	0.026	0.029	17.2	4	Same
FeMoNiCrBi + (Ti, Cr)C	0.031	0.035	14.3	4	»
FeMoNiCrB + FeTiO₃	0.031	0.035	14.3	4	»
5 % NaOH					
FeMoNiCrB	0.047	0.052	9.6	4	Resistent
FeMoNiCrBi + ZrB₂	0.033	0.038	13.1	4	Same
FeMoNiCrBi + (Ti, Cr)C	0.038	0.04	12.5	4	»
FeMoNiCrB + FeTiO₃	0.04	0.043	11.1	4	»
10 % H₂SO₄					
FeMoNiCrB	0.2	0.22	2.3	6	Low-resistant
FeMoNiCrBi + ZrB₂	0.156	0.174	2.8	6	Same
FeMoNiCrBi + (Ti, Cr)C	0.166	0.186	2.5	6	»
FeMoNiCrB + FeTiO₃	0.182	0.21	2.4	6	»

Table 6. Test results of detonation coatings based on FeMoNiCrB on abrasion resistance by friction against a loosely fixed abrasive

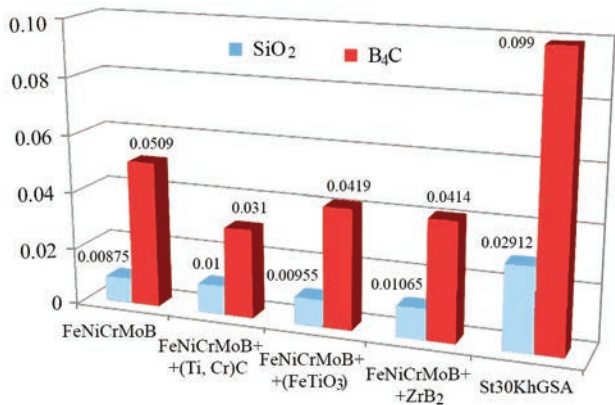| Composition of coating	SiO₂ abrasive		B₄C abrasive	
	Given wear, g/km	Relative wear resistance	Given wear, g/km	Relative wear resistance
FeMoNiCrB	0.00875±0.00075	3.3	0.0509±0.002	1.9
FeMoNiCrB + ZrB₂	0.01065±0.00015	2.6	0.0419±0.0003	2.3
FeMoNiCrB + (Ti, Cr)C	0.01±0	2.7	0.031±0.001	3.0
FeMoNiCrB + FeTiO₃	0.00955±0.00595	2.9	0.0414±0.0003	2.3
Steel 30KhGSA	0.0291±0.00145	–	0.099±0.0002	–

occurs in a sulfuric acid solution, the minimum is in 3 % NaCl, i.e. the corrosion rate correlates with the pH value of the solution and decreases in the range from weakly acidic to neutral and alkaline solutions. Therefore, the corrosion rate in the 10 % H_2SO_4 solution (pH is 1) is higher than in the neutral 3 % NaCl (pH is 8.0) and in the alkaline 5 % NaOH solution (pH is 13).

Figure 4. Test results of coatings on friction wear against SiO_2 and B_4C abrasives, g/km

Thus, electrochemical tests in the studied solutions showed that in detonation coatings with CP FeMoNiCrB + (ZrB₂, (Ti, Cr)C, FeTiO₃), corrosion current decreases from 2·10⁻⁶ in the 3 % NaC1 and 5 % NaOH to 1.5·10⁻⁵ A/cm₂ in the 10 % H_2SO_4. Introduction of ZrB2, (Ti, Cr)C, FeTiO₃ in all the coatings leads to a decrease in the corrosion current by 1.5–3.0 times as compared to the material of the base FeMoNiCrB depending on the type of additive in the direction FeTiO₃ → (Ti, Cr))C → ZrB₂.

On the basis of the received experimental data, the comparative evaluation of fatigue life of the studied coatings of identical thickness in the considered corrosion media was carried out. The results of the calculation of the evaluated service life of the studied coatings at a thickness of 500 μm are given in Table 5.

The results of tests of wear resistance of detonation coatings are presented in Table 6 and in Figure 4.

When using the SiO_2 abrasive, the highest wear resistance is observed in the coatings produced from FeMoNiCrB powder, and in the case of B_4C abrasive, among the developed composite coatings, the coat-

ing produced from FeMoNiCrB composite powder +30 vol.% (Ti, Cr)C is the the most wear-resistant. This correlates with the average microhardness of the coatings (see Table 3), which in the case of FeMoNiCrB + (Ti, Cr)C amounts to 4450 MPa against ~3800 MPa in CP FeMoNiCrB + FeTiO$_3$ and FeMoNiCrB + ZrB$_2$.

CONCLUSIONS

1. The coatings deposited by detonation spraying of composite powders (CP) FeMoNiCrB – ZrB$_2$, (Ti, Cr) C, FeTiO$_3$, and FeMoNiCrB powder, have a dense lamellar multiphase structure. The microhardness of FeMoNiCrB coating is 4855 ± 1023 MPa, and in the composite coatings FeMoNiCrB + (ZrB$_2$, (Ti, Cr), FeTiO it is 3830 ± 570 MPa, 4450 ± 700 (20 MPa and 3750 ± 620 MPa, respectively).

2. All the produced coatings have an amorphous-crystalline structure. The composition of all the coatings includes solid solutions based on Fe and (Fe, Ni) and boride phases Mo$_2$FeB$_2$, Fe$_2$B, oxides, as well as the amorphous phase, the content of which in the spraying process grows as compared to the powder.

3. The carried out electrochemical studies showed that the corrosion resistance of detonation coatings depends on pH of the solution. In alkaline and neutral media, the corrosion resistance of coatings is by an order higher than in acidic medium, which is predetermined by the presence of SO$_4^{-2}$ anions. The introduction of additives ZrB$_2$, (Ti, Cr)C and FeTiO$_3$ into the coating reduces the corrosion rate by 2–3 times in the 3 % NaCl solution and 5 % NaOH and has a weak effect on the corrosion rate in H$_2$SO$_4$. Detonation coatings, which were investigated in the 3 % NaCl and 5 % NaOH solutions are classified in accordance with GOST 308–85 at a thickness of 500 μm as resistant with a service life of 14–17 years and 11–13 years, respectively, and in the 10 % H$_2$SO$_4$ as low-resistant with a service life of 2.4–2.8 years.

4. The studies of wear resistance of the detonation coatings FeMoNiCrB and CP FeMoNiCrB under wear conditions in unfixed abrasives SiO$_2$ and B$_4$C showed that the relative wear resistance in relation to the reference "steel 30KhGSA" amount to 2.6–3.3 in SiO$_2$ medium and 1.9–2.9 in B$_4$C medium. The highest wear resistance 2.7–3.0 was achieved in the case of FeMoNiCrB + (Ti, Cr)C coating, having a microhardness of 4450 ± 700 MPa.

REFERENCES

1. Suzuki, K., Fujimori, H., Hashimoto, K. (1987) *Amorphous metals*. Moscow, Metallurgiya [in Russian].
2. Lyuborskij, F.E. (1987) *Amorphous metal alloys*. Moscow, Metallurgiya [in Russian].
3. Kunitskij, Yu.A., Borisov, Yu.S., Korzhik, V.N. (1989) *Non-crystalline metal materials and coatings in engineering*. Kiev, Tekhnika [in Russian].
4. Borisov, Yu.S., Borisova, A.L., Burlachenko, O.M. (2021) Composite powders based on FeMoNiCrB amorphizing alloy with additives of refractory compounds for thermal spraying of coatings. *The Paton Welding J.,* **11**, 44–53. DOI: https://doi.org/10.15407/tpwj2021.11.07
5. (2007) GOST R 9.905–2007: *Unified system of corrosion and ageing protection. Corrosion test methods. General requirements.* Moscow, Izd-vo Standartov [in Russian].
6. Zhuk, N.P. (2006) *Lectures on theory of corrosion and metal protection.* Moscow, Alyans [in Russian].
7. Semenova, I.V., Florionovich, G.M., Khoroshilov, A.V. (2002) *Corrosion and protection from corrosion.* Moscow, Fizmatlit [in Russian].
8. (1981) GOST 23.208–79: *Ensuring of wear resistance of products. Wear resistance testing of materials by friction against loosely fixed abrasive particles.* Moscow, Izd-vo Standartov [in Russian].
9. Grigorenko, G.M., Borisova, A.L., Adeeva, A.I., Sladkova, V.N. (1995) Application of method of quantitative X-ray structure analysis at investigation of phase composition of thermal coatings. *Problemy Spets. Elektrometallurgii*, **2**, 63–71 [in Russian].
10. (1999) GOST 9.909–86: *Metals, alloys, metal and nonmetal inorganic coatings.* Moscow, Izd-vo Standartov [in Russian].
11. Gerts, I. (1979) Passivation of wrought nickel in sulfuric acid. *Zashchita Metallov*, 15(**1**), 29–33 [in Russian].
12. Tulskyi, G.G., Artemenko, V.M., Deribo, S.G. (2019) *Theoretical electrochemistry*. Kharkiv, KhPI [in Ukrainian].

ORCID

Yu.S. Borysov: 0000-0002-6019-8464,
A.L. Borysova: 0000-0002-7376-3370,
T.V. Tsymbalista: 0000-0001-9569-7776,
A.I. Kildiy: 0000-0001-8133-8705,
K.V. Yantsevych: 0000-0002-3975-7727,
Z.G. Ipatova: 0000-0003-2209-408X

CONFLICT OF INTEREST

The Authors declare no conflict of interest

CORRESPONDING AUTHOR

Yu.S. Borysov
E.O. Paton Electric Welding Institute of the NASU
11 Kazymyr Malevych Str., 03150, Kyiv, Ukraine
E-mail: borisov@paton.kiev.ua

JOURNAL HOME PAGE

https://pwj.com.ua/en

CHEMICAL WELDING OF POLYURETHANES AND THEIR COMPOSITES

A. Vashchuk[1]**, M. Iurzhenko**[1]**, M. Korab**[1]**, E. Privalko**[2]

[1]E.O. Paton Electric Welding Institute of the NASU
11 Kazymyr Malevych Str., 03150, Kyiv, Ukraine
[2]O.O. Bogomolets National Medical University
13 Shevchenko Blvd, 01601, Kyiv, Ukraine

ABSTRACT

Chemical welding as an attractive alternative to classical joining techniques occurs through the formation of new chemical bonds between neighboring molecules at the contacting surfaces to be joined. This review paper presents the current state of the chemical welding of polyurethanes and their composites via dynamic covalent bonds. The strength of welded joints obtained by different welding technologies was compared. Different processing parameters affecting the joint quality, namely welding time and welding temperature were summarized. The future perspectives of chemical welding of polyurethanes and their composites were discussed in the paper.

KEY WORDS: polyurethanes, composites, chemical welding

INTRODUCTION

Polymeric materials have been widely used in various fields of advanced technology, including transport, defense, civil industries due to low weight, specific stiffness, corrosion resistance, and high fatigue life. In advanced technologies, manufacturing large parts requires a complex mold, which consequently means a substantial increase in the cost. However, such a complex part can be manufactured through the assembling of small parts by using different joining techniques. Thus, there is a growing need for a fast and effective way of joining polymer structures.

Welding technology serving as an exceedingly good tactic to save materials and provide an excellent bonding strength in the field of metal processing is also extensively applied in thermoplastic polymer materials. High-quality welding could be obtained when thermoplastic polymers are heated to their viscous flow state in the contact area. Thermosetting polymers are quite advantageous in comparison to thermoplastics since they have higher thermal stability, fixation ability, and can perform higher levels of mechanical work. Moreover, they cannot be replaced by thermoplastics in a wide range of engineering applications, especially those requiring high-performance such as the aircraft and automotive industry. However, due to the permanent molecular structure, thermosets could not melt or be dissolved once synthesized. As a consequence, the traditional diffusion welding technology cannot be simply applied to thermosets and their composites. Therefore, thermoset systems must rely on chemical welding only to join them.

Chemical welding refers to the process that occurred through the formation of new chemical bonds between neighboring molecules at the contacting polymer surfaces to be joined. In particular, vitrimers as a new class of polymers can rearrange their network topology via thermally triggered bond exchange reactions (BERs) at elevated temperatures without affecting the average crosslinking degree. Thus, when two separated vitrimer surfaces are brought into contact the reversible associations (bridges) are formed across the interface resulting in chemical welding (Figure 1). Polyurethanes represent a class of materials with important industrial applications that exhibit favorable mechanical, physical, and biocompatible properties [1–3]. Moreover, vitrimeric characteristics of polyurethanes have been already reported [4–5]. This review paper summarizes results on investigations of the current state of the chemical welding of polyurethanes and their composites.

RECENT WORK ON CHEMICAL WELDING

Recently, to tackle the obstacle the vitrimer polyurethanes have been easily synthesized by using the designed secondary amine (through the addition reaction of aziridines and lauric acid) and isophorone diisocyanate in the absence of any catalyst [6]. The long strip of the sample with a width of 4 mm and thickness of 2 mm was cut in half with a razor blade and then the two pieces were put together at 25 °C for 3 min, followed by welding at 120 °C for 60 min without external stress. The thermal-triggered mechanism of chemical welding via dynamic hindered urea bonds exchange under catalyst-free conditions is shown in Figure 2. It was found, that the welded joint can be stretched up to 200 % strain without tearing and can lift a weight of 0.5 kg without breaking at the welded part (Figure 3).
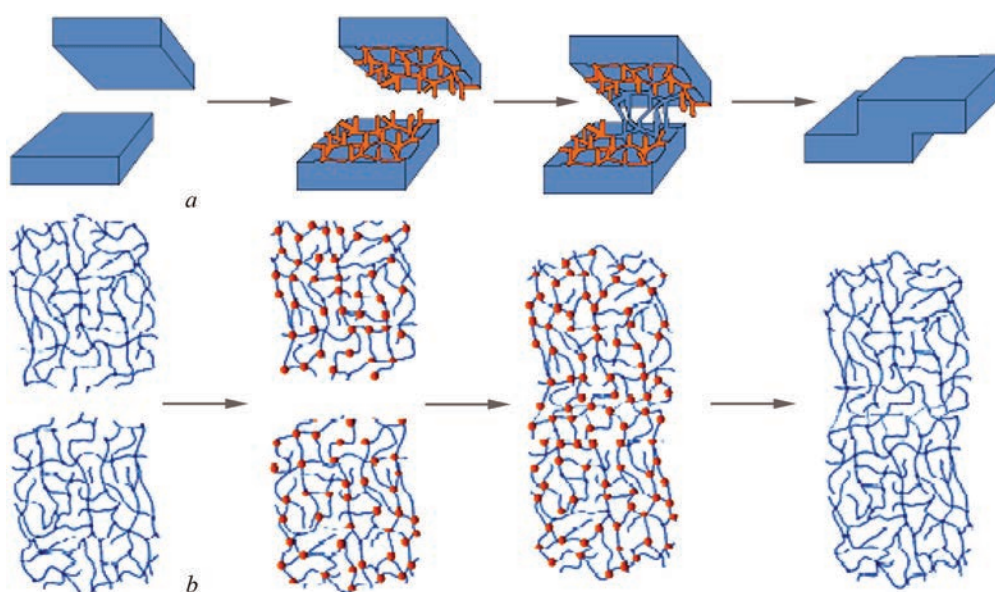
Figure 1. Chemical welding of two surfaces involves chemical reactions (*a*). Topological rearrangements occur via exchange reactions on a macromolecular chain during chemical welding (*b*)

In recent years with increasing attention on the environment and economy, various low-cost and sustainable biobased resources have been used as alternatives to petroleum-based materials. Fully biobased and recyclable polyurethane-vitrimers were designed via classical polyurethane chemistry: reaction of polyethylene glycol, castor oil, and hexamethylene diisocyanate, using dibutyltin dilaurate and ethyl acetate as catalyst and solvent, respectively [7]. The chemical welding through transcarbamoylation reaction of carbamate bonds was carried out (*i*) at 150 °C for different time (2, 5, 10, 20 and 30 min) and *(ii)* at different temperature (140 °C, 150 °C, 160 °C) for 5 min by keeping the other parameters constant. This study showed that the stress of chemically welded joints tended to increase with welding time at a fixed temperature (Figure 4, *a*). It is worth noting that the welded joints with welding time of 2, 5 min (Figure 4, $d^{①}$), and 10 min (Figure 4, $d^{②}$) all broke at the overlapped part and had relatively lower stress at break. However, the welded joints under the same temperature but with a longer welding time (20 and 30 min) had stress at

break higher than 2 MPa and broke at bulk material instead of the overlapped part (Figure 4, $d^{③}$) due to nearly complete transcarbomoylation reaction at the overlapped part. Welding temperature also plays an important role in weld quality. It can be seen in Figure 4 *b* that higher welding temperature promoted better recovery of the material strength across the interface with the same welding time. Importantly, samples chemically welded at 140 °C (Figure 4, $d^{①}$) or 150 °C (Figure 4d^{②}) were broken at the overlapped part and had relatively lower stress at the break, whereas the samples welded at 160 °C were broken at bulk material part (Figure 4, $d^{③}$). Thus, a facile strategy to select and optimize the processing conditions for chemical welding of films based on polyurethanes could be realized through changes in welding time and welding temperature.
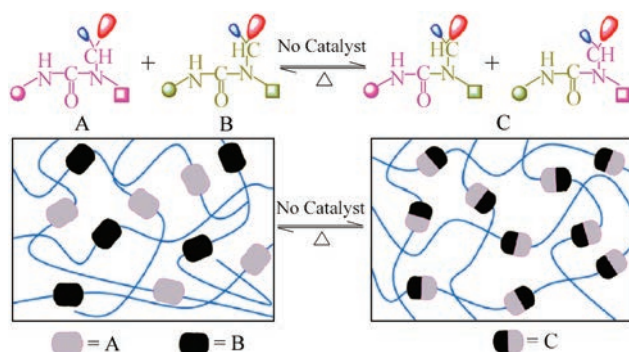
Figure 2. Thermal-triggered mechanism of dynamic hindered urea bonds exchange [6]
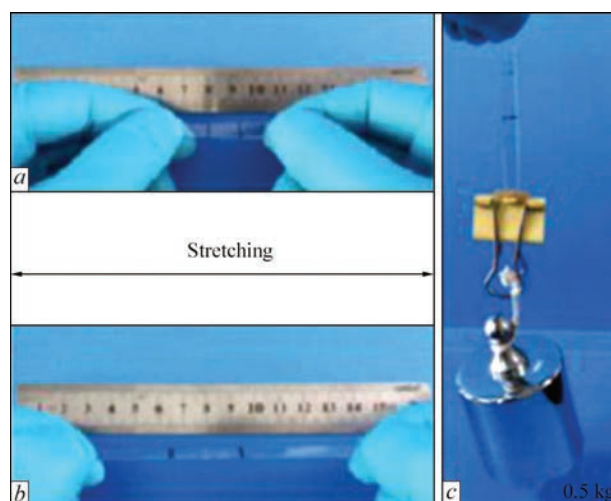
Figure 3. Photograph of film welded at 120 °C for 60 min before (*a*) and after (*b*) stretching. Photograph of welded joint with a 0,5 kg weight lifting test (*c*) [6]
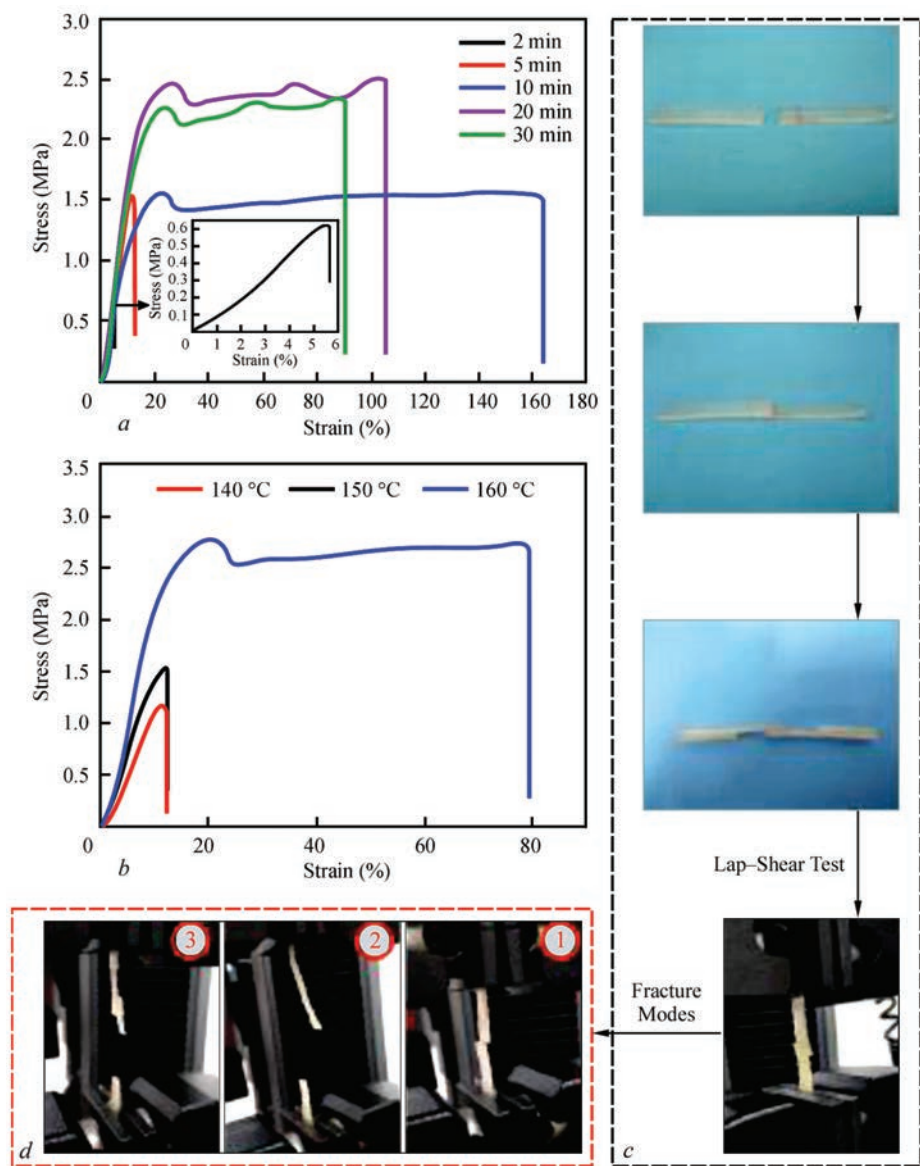
Figure 4. The mechanical properties of the welded joint at 150 °C at different times (*a*) and different temperatures for 5 min (*b*). Specimen of the lap-shear test (*c*). Fracture modes of the welded joints (*d*) [7]

The welding process is not limited to the film joints, and the thick samples can be chemically welded. Thus, a new type of vitrimers were prepared from commercially available monomers (trimethylolpropane tris(3-mercaptopropionate), hexamethylene diisocyanate) by an easy procedure using tert-butyl isocyanate and dibutyltin dilaurate as the catalysts [8]. The synthetic reaction has click characteristics, which assure a great homogeneity of the poly(thiourethane) network structure. These materials can be chemically welded at 180 °C for 40 min under pressure, as it is shown in Figure 5. The trans-thiocarbamoylation reaction, which has a non-dissociative mechanism, responsible for the welding ability of these vitrimers has been chemically assessed by the use of model compounds and gas chromatography coupled to mass spectrometry. The non-dissociative character of the trans-thiocarbamoylation process has been confirmed in the materials by FTIR spectroscopy.

In the above studies, the heating stimulus was utilized to activate the chemical welding. However, direct heating is unsuited for a heat-sensitive application like biomedicine, and it is also limited when the targeted locations could not be reachable in some special engineering environments. In comparison with heating, the near-infrared (NIR) light-responsive method possesses many distinctive advantages including (*i*) remote activation is available due to the travel characteristics of light; (*ii*) regional activation can be realized by regulating the spot size without intervening with the surrounding environment; (*iii*) light stimulus is immediate by turning the light source on or off [9]. A common approach to creating light-responsive chemical welding is to introduce photothermal fillers,
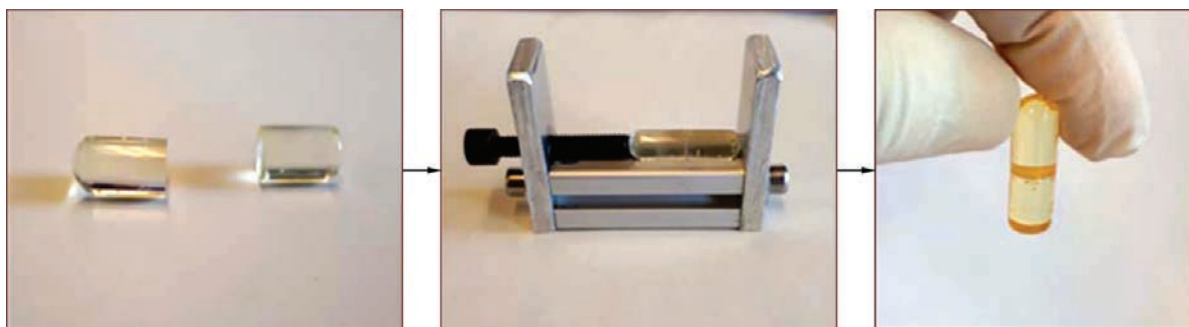
Figure 5. Visual demonstration of chemical welding of poly(thiourethane) vitrimer films at 180 °C for 40 min under pressure [8]

such as metal nanoparticles, conjugated polymers, rare earth organic complexes, carbon nanomaterials, photothermal fillers. Among them, carbon nanotubes (CNTs) as novel 1D nanomaterials have many excellent performances, namely high mechanical properties, electrical and thermal conductivity. Most important of all, CNTs can absorb NIR light and generate a large amount of heat [10 – 11]. Therefore, the addition CNTs to polyurethane-vitrimers may be a good option to carry out chemical welding induced by NIR light.
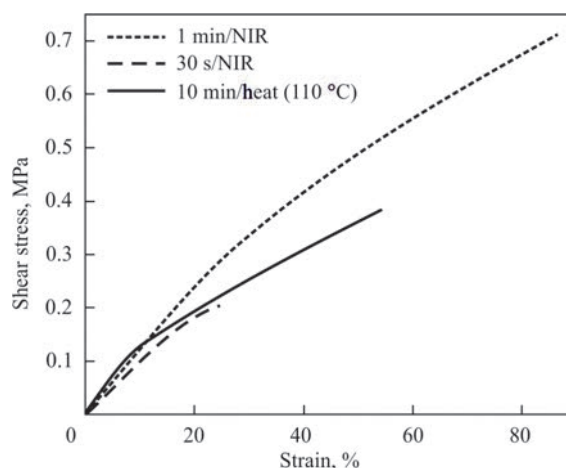
Recently, CNTs-polyurethane vitrimer nanocomposites were synthesized by chemical reaction of the hexamethylene diisocyanate with polyethylene glycol (M_n = 2000) and castor oil in the presence of dibutyltin dilaurate as a catalyst for transcarbamoylation, with different content of CNTs ranging from 0 to 1 wt.% [12]. Chemical welding of the nanocomposites induced by NIR light (980 nm) was conducted with an overlap area of 1.0×1.0 mm and irradiation

by a NIR light at different times. The light intensity of the NIR laser irradiation was 1.41 W·cm^{-2}. Although the shortest welding time was only 0.5 min, the shear strength has already reached 0.2 MPa, which was an amazing welding efficiency. As seen in Figure 6, *b–d*, the shear strengths of the welded joints gradually increased with the extension of welding time from 2 to 20 min proving that longer welding time enhances the welding effect. Beyond that, the effect of CNTs content on the welding efficiency was discussed as well. It was found that the composite with 0.5 wt.% CNTs has a higher thermal conductivity than that with 0.05 and 0.1 wt.% CNTs under the same welding conditions, which promotes transcarbamoylation and endows the sample with excellent welding performance.

Recently, the chemical welding of the nanocomposites induced by heat and NIR light was discussed separately, and the welding efficiency of the two methods was compared (Figure 7) [12]. It was found, that the two pieces of CNTs-polyurethane nanocomposites can never be chemically welded at 80 °C (T_v = 90 °C) due to the lack of adequate exchange reaction at this temperature. However, the specimens could be welded together at 110 °C for 10 min. It should be noted, that temperature of nanocomposites produced by the photothermal effect of CNTs has reached 90 °C 0.5 min or 110 °C at 1 min. It was surprising to find that the
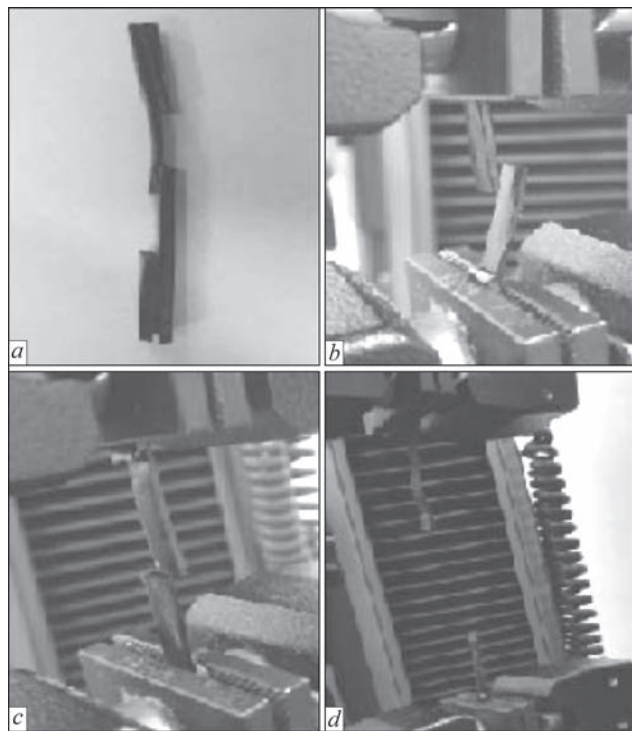
Figure 6. The sample of the lap-shear test (*a*). The photographs of the lap-shear test from the samples with different weld times: 2 (*b*), 5 (*c*), and 20 min (*d*) [12]

Figure 7. Comparison of welding effects of CNTs-polyurethane vitrimer nanocomposite induced by NIR and heat [12]

shear strength of the sample irradiated for 1 min by NIR was much stronger than that of the specimen heated at 110 °C for 10 min, which further proves that the NIR-welding technology possesses a higher efficiency. According to these results, chemical welding induced by NIR light would be beneficial for joining or repairing the CNTs-polyurethane nanocomposites.

CONCLUSIONS

Chemical welding is a relatively new welding approach that opens the way towards assembly of polyurethane materials without adhesives or molds. Thus, polyurethanes can be facilely welded by heat. The weld quality could be controlled by different welding parameters associated with the welding procedure such as welding time and welding temperature. Chemical welding of polyurethane nanocomposites could be induced by heat and NIR-light. The NIR-induced welding technology is not only convenient but also environmentally friendly and has higher efficiency compared with thermal technology. Moreover, the NIR-induced welding technology makes remote and spatial welding technology of nanocomposites possible. Although significant progress was made by researchers in the past years, their inputs are mostly based on observation of the weld with electron microscopic techniques and test data coming from mechanical tests. Work is left to be done to get high joining strengths with a reasonable welding time to enable the efficient transfer of new technologies to the industry in the close future.

REFERENCES

1. Privalko, V.P., Privalko, E.G., Shtompel, V.I. et al. (1999) Influence of the structure of soft and stiff chain fragments on properties of segmented polyurethanes. I. Phase morphology. *Polymer Engineering & Sci.*, **39**, 1534–1540.
2. Zdrahala, R.J., Zdrahala, I.J. (1999). Biomedical applications of polyurethanes: A review of past promises, present realities, and a vibrant future. *J. of Biomaterials Applications*, **14**, 67–90.
3. Georgoussis, G., Kyritsis, A., Pissis, P. et al. (1999) Dielectric studies of molecular mobility and microphase separation in segmented polyurethanes. *European Polymer J.*, **35**, 2007–2017.
4. Yan, P., Zhao, W., Fu, X. et al. (2017) Multifunctional polyurethane-vitrimers completely based on transcarbamoylation of carbamates: thermally-induced dual-shape memory effect and self-welding. *RSC Advances*, **7**, 26858–26866.
5. Zheng, N., Hou, J., Xu, Y. et al. (2017) Catalyst-free thermoset polyurethane with permanent shape reconfigurability and highly tunable triple-shape memory performance. *ACS Macro Letters*, **6**, 326–330.
6. Jiang, L., Liu, Z., Lei, Y. et al. (2019) Sustainable thermosetting polyurea-vitrimers based on a catalyst-free process with reprocessability, permanent shape reconfiguration and self-healing performance. *ACS Applied Polymer Materials*, **1**, 3261–3268.
7. Yan, P., Zhao, W., Fu, X. et al. (2017) Multifunctional polyurethane-vitrimers completely based on transcarbamoylation of carbamates: Thermally-induced dual-shape memory effect and self-welding. *RSC Advances*, **7**, 26858–26866.
8. Gamardella, F., Guerrero, F., De la Flor, S. et al. (2019) A new class of vitrimers based on aliphatic poly(thiourethane) networks with shape memory and permanent shape reconfiguration. *European Polymer J.*, **122**, 109361.
9. Habault, D., Zhang, H., Zhao, Y. (2013) Light-triggered self-healing and shape-memory polymers. *Chemical Society Reviews*, **42**, 7244–7256.
10. Yang, Y., Pei, Z., Li, Z. et al. (2016) Making and remaking dynamic 3D structures by shining light on flat liquid crystalline vitrimer films without a mold. *J. of the American Chemical Society*, **138**, 2118–2121.
11. Mizuno, K., Ishii, J., Kishida, H. et al. (2009) A black body absorber from vertically aligned single-walled carbon nanotubes. *Proc. of the National Academy of Sci.*, **106**, 6044–6047.
12. Yan, P., Zhao, W., Wang, Y. et al. (2017) Carbon nanotubes-polyurethane vitrimer nanocomposites with the ability of surface welding controlled by heat and near-infrared light. *Macromolecular Chemistry and Physics*, **218**, 1700265.

ORCID

A. Vashchuk: 0000-0002-4524-4311,
M. Iurzhenko: 0000-0002-5535-731X,
M. Korab: 0000-0001-8030-1468,
E. Privalko: 0000-0002-9893-5335

CONFLICT OF INTEREST

The Authors declare no conflict of interest

CORRESPONDING AUTHOR

A. Vashchuk
E.O. Paton Electric Welding Institute of the NASU
11 Kazymyr Malevych Str., 03150, Kyiv, Ukraine
E-mail: alina.vashchuk@i.ua

JOURNAL HOME PAGE

https://pwj.com.ua/en

PRODUCING Fe-BASED NANOPARTICLES IN NaCl MATRIX BY THE METHOD OF EB-PVD ON A ROTATING SUBSTRATE

Yu.A. Kurapov, V.O. Osokin, G.G. Didikin, L.A. Krushynska, S.E. Lytvyn, V.V. Boretskyi

E.O. Paton Electric Welding Institute of the NASU
11 Kazymyr Malevych Str., 03150, Kyiv, Ukraine

ABSTRACT

The paper gives the results on the features of formation of a microlayered structure of NaCl–Fe composite and the possibility of producing iron nanoparticles of different size on a rotating substrate by EB-PVD method with peripheral position of evaporation material sources relative to the substrate rotation axis. It is shown that the layer thickness is determined by the substrate rotation speed. It is found that Fe nanoparticles are present in NaCl matrix in the form of Fe_3O_4 oxide.

KEY WORDS: electron beam evaporation, condensation, EB-PVD, composite, nanoparticles, iron oxide, phase composition

INTRODUCTION

Investigations of the conditions of formation of composite materials based on iron nanoparticles, having a set of medicobiological characteristics, are required for development of nanostructured medicinal substances with the purpose of modification of the existing medical drugs by active nanoparticles. The nanoparticles have a well-developed active surface and, consequently, high sorption capacity. Due to their size (less than 15 nm) the iron nanoparticles can interact and bind with biological objects, the size of which is equal to 10–100 nm in the case of cells, 920–450 nm for viruses, 2 nm wide, 10–100 nm long for DNA [1]. Formation of nanoparticles in water-soluble matrices allows storing them while preserving their size for a long time.

Experimental data accumulated so far, confirm the possibility of obtaining NaCl-Fe composite materials with nanoparticles of iron oxide (Fe_3O_4, Fe_2O_3) on stationary substrates. The geometry of stationary substrate location relative to vapour flows of initial materials leads to formation of films with composition gradient up to almost 40 %, increases the inhomogeneity of NaCl–Fe materials and limits the technological process productivity [2–5].

EB-PVD process combines the possibilities of intensive controlled evaporation of various materials in vacuum with their subsequent condensation on a cooled rotating substrate, and it opens up broad possibilities of variation of application of diverse control schemes and automation of the parameters of this technological process performance [6–8]. Therefore, development of scientifically based electron beam technology of producing iron nanoparticles in NaCl matrix on a rotating substrate is an urgent task.

The work deals with the features of application of a technological procedure of conducting the EB-PVD process with the position of evaporation material sources peripheral relative to the substrate rotation axis to produce NaCl–Fe composites [9], and presents the results of experimental studies of the structure and some properties of the produced micro- and nanoscale materials.

INVESTIGATION MATERIALS AND PROCEDURES

Sodium chloride and Armco-iron were used as initial materials for evaporation. Material purity was 99.5 %. Sodium chloride cylinders of 49.8 mm diameter and 60–80 mm height were made by cold pressing. Iron ingots were produced by electron beam remelting of 60 mm diameter rods into a 52 mm crucible. Produced ingots were ground to finish size of 49.5 mm diameter and 150–200 mm length, which prevented their jamming in the crucible at vertical feed as they evaporated.

After complete depressurizing of the vacuum chamber, NaCl–Fe composite was separated from the substrate and stored in the initial state in air and in alcohol. In connection with the problem of making sections by a standard procedure from NaCl–Fe composites (NaCl matrix dissolves in H_2O), investigations were conducted on self-standing brittle chips of composites.

MICROSTRUCTURE

was studied on transverse (in the condensation direction) chips of the samples, using scanning electron microscopy Cam Scan 4D.

ELEMENTAL COMPOSITION

of the composites was determined using an X-ray spectral microanalyser — EDX attachment to Cam Scan 4D microscope. At application of INCA-200 Energy program for result processing, the measurement error was equal to 0.3 %.

X-RAY PHASE ANALYSIS (XPA)

Diffraction patterns of the samples were recorded in DRON-UM1 diffractometer in filtered cobalt (CoK_α) radiation in Bragg-Brentano filming geometry in the angle range of 10–85° with 0.05 step and exposure in 2 s point. They were saved in the digital form in a file of 2θ(degr.)-I(intensity, s^{-1}) format. Phase identification was conducted with application of X-ray data base PDF-2. Average crystallite size was calculated by Scherrer equation. Semi-quantitative phase analysis was performed using Match program.

STUDYING THE SIZE OF IRON POWDER PARTICLES OF Fe_2O_3–NaCl–H_2O) COLLOID SYSTEMS (CS)

Deionizer water was used to prepare Fe_3O_4–NaCl–H_2O CS. Not less than three measurements were taken in each sample to control the repeatability of the results. Higher degree of particle dispersion in the studied samples was achieved by heating the samples up to 80 °C temperature in a quartz cuvette. In DLS-method (Dynamic Light Scattering) the main parameters characterizing the particle size distribution are the average hydrodynamic diameter of particles (Z-average) and polydispersity index (PdI) — a dimensionless value characterizing the distribution width (this parameter is highly sensitive to the presence of aggregates in the sample). For monodispersed samples PdI parameter is not higher than 0.1.

PARTICLE SIZE DISTRIBUTION IN THE COLLOID SYSTEMS

was studied by the method of laser correlation spectroscopy (LCS) in laser correlation spectrometer "Zeta

Figure 1. Diagram of producing NaCl–Fe composites on a rotating substrate: *1, 2* — electron beam guns; *3* — rotating substrate; *4, 7* — water-cooled crucibles; *5* — Fe ingot; *6* — NaCl cylinder; *8* — graphite washer

Sizer-3" (Malvern Instruments, Great Britain) with "Multi 8 computingcorrelatetype 7032 ce" correlator. The instrument is fitted with helium-neon (He–Ne) laser with 633 nm wave length and 25 mW power. Instrument measurement range is from 1 nm to 20 μm. The function of size distribution of the nanoparticles was computed from experimentally derived autocorrelation function using PCS Size Mode v.1.61 program. Particles being in a suspended state in the liquid, at their irradiation by the laser beam scatter the light, which is focused at a certain angle and recorded by the photodetector. Scattered light registration angle was 90°. Particle size distribution was converted from intensity units into quantitative ones using Mie theory (Mie 1908).

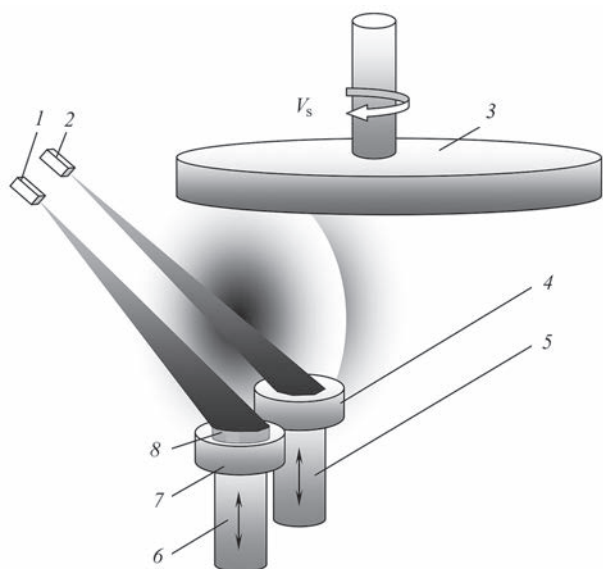## KINETICS OF OXIDATION OF MICROLAYERED NaCl–Fe COMPOSITES IN AIR

was studied in thermogravimetric analyzer (TGA) TGA-7 of Perkin Elmer Company (USA) at a stable fixed heating/cooling rate of 10 °C min^{-1} in the range of 20–650 °C. A sample of NaCl–Fe composite of up to 100 mg weight was placed on a platinum plate, which was hung on sensitive balance (up to 0.1 μg) and was heated or cooled, fixing all the weight changes in dynamics.

EXPERIMENTAL TECHNIQUE

Technological procedure of producing NaCl–Fe composites on a rotating substrate is shown in Figure 1. Evaporation materials *5*, *6* are placed into copper water-cooled crucibles *4*, *7* and they are transformed into vapour by electron beam guns *1*, *2,* and the mixed vapour flow is condensed on the rotating substrate *3* positioned above the crucibles.

Initial material evaporation was performed from crucibles *4*, *7* with inner diameter of 50 mm by electron beam guns *1*, *2* of 60 kW power. The gun accelerating voltage was 20 kV. Application of washer *8* with a system of inclined vapour channels at NaCl evaporation ensured uniform distribution of sodium chloride layer thickness in the produced composites along the rotating substrate radius.

Vacuum in the process chamber during evaporation was (1.2–2.4)·10^{-2} Pa. The total vapour flow was condensed on a rotating water-cooled copper substrate *3* of 400 mm diameter with pre-applied anti-adhesion layer of NaCl. Substrate temperature was equal to approximately 70 ± 10 °C. The distance from the crucibles to the substrate was equal to 230 mm, and the distance between the crucible axes was 115 mm. One composite layer (composite) — H which consisted of two NaCl- and Fe-enriched layers, h_{NaCl} and h_{Fe}, respectively, was produced in one cycle of substrate ro-

Таблиця 1. Characteristics of typical microlayered NaCl–Fe composites produced at different speeds of substrate rotation (V_s)

V_s. rpm·min^{-1}	t_{ex}. min	Number of layers	H. μm	h_{NaCl}. μm	h_{Fe}. μm	h_{Fe}/h_{NaCl}
2	11	22	3.89	3.25	0.64	0.2
20	12	240	0.68	0.56	0.12	0.2
25	20	500	0.55	0.46	0.09	0.2

Note. H — total thickness of an isolated NaCl composite; h_{NaCl} — thickness of NaCl-enriched layer in an isolated NaCl–Fe composite. h_{Fe} — thickness of the layer enriched in Fe in an isolated NaCl–Fe composite

tation on the path over the total vapour flow of ion-sodium chloride. The thickness of the composite layers and iron concentration in the composite was regulated by substrate rotation speed and intensity of initial material evaporation. The deposition rate of the total vapour flow (condensation rate V_c) was 6–9 μm·min^{-1}. The produced condensate thickness was 80–240 μm.

EXPERIMENTAL RESULTS

A feature of the produced NaCl–Fe composites at evaporation from two independent crucibles and deposition of mixed vapour flows on the rotating substrate is their layering. It is logical to assume that the main causes for appearance of layering are variations of the condensation flows and features of crystal growth. Generalized comparative characteristics of the studied NaCl composites produced on a rotating substrate, are given in Table 1.

As one can see from the presented data, a reduction of the total thickness of an individual NaCl layer by 14 % is noted with increase of the substrate rotation speed from 2 to 25 rpm·min^{-1}, here the ratio of layers enriched in iron and sodium chloride h_{Fe}/h_{NaCl} remains constant and equal to approximately 0.2.

Influence of the rotating substrate speed on thickness of the layers, enriched in Fe and NaCl in NaCl–Fe composite, is shown in Figure 2.

Thicknesses of the layers enriched in NaCl and Fe in NaCl–Fe composite depend on the rotating substrate speed (Figure 2). At the speeds of 25 rpm·min^{-1} the thicknesses of the layers enriched in NaCl and Fe, are equal to 0.46 ad 0.09 μm, respectively and are by 14 % lower, compared to speed V = 2.0 rpm·min^{-1}.
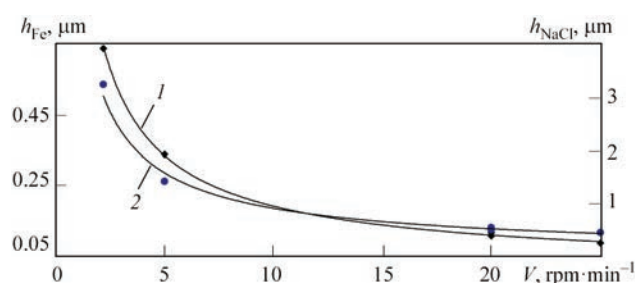
Figure 2. Dependence of the thickness of h_{Fe} — (*1*) and h_{NaCl} (*2*) layers of NaCl–Fe composite on the substrate rotation speed
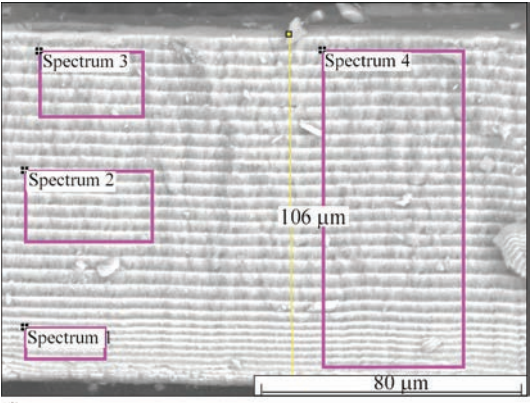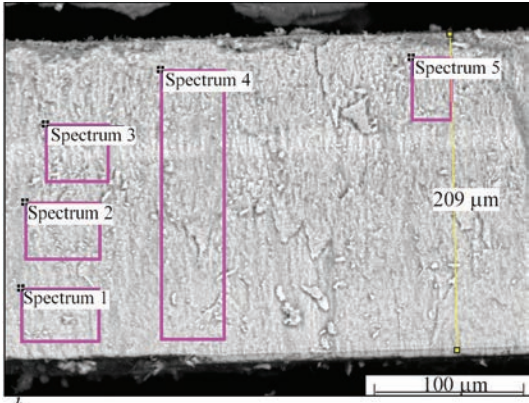
STRUCTURE OF CHIPS OF INITIAL NaCl–Fe COMPOSITE

Figure 3 shows the microstructure of the produced NaCl–Fe composites at condensation temperature of approximately 70 °C with different speed of substrate rotation of 2 and 20 rpm·min^{-1}. The composites consist of layers located parallel to the rotating substrate plane (Figure 3, *a*). The layers are made up of crystallites directed along the condensation flow, and have a weakly pronounced columnar structure across the condensate thickness. Columnar crystallites are oriented in the direction, normal to the rotating substrate surface and have NaCl and Fe-enriched alternating layers of different thickness (Figure 3, *b*). Such a growth pattern corresponds to the earlier established regularity, according to which columnar crystallites form in the range of the ratio of substrate temperature to metal melting temperature of 0.3–0.5 [10]. The maximum size of the crystallites calculated by Sherrer equation in NaCl-enriched layers, is close to 45 nm. Maximum size of crystallites in Fe-enriched layers, is
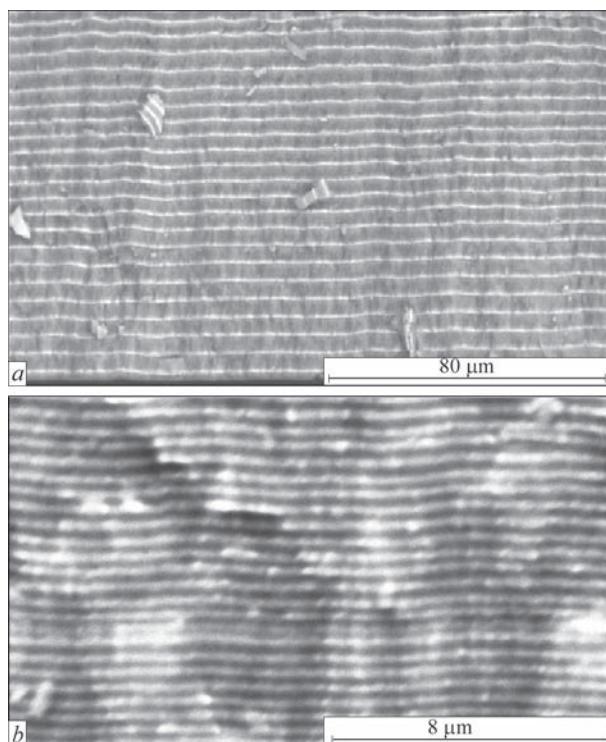
Figure 3. Typical microstructure of the transverse chip of NaCl–Fe composite samples, produced on a rotating substrate: *a* — 2; *b* — 20 rpm·min^{-1}

Table 2. Elemental composition of transverse chip of samples of NaCl–Fe composites, produced at different speed of substrate rotation, wt.%

Spectrum	Fe	O	Na	Cl
Substrate rotation speed $V_s \sim 2.0$ rpm·min^{-1} (a)				
1	27.85	13.96	28.05	30.14
2	16.46	18.00	30.39	35.15
3	14.22	17.36	30.68	37.73
4	18.38	15.43	29.49	36.69
Substrate rotation speed, $V_s \sim 25.0$ rpm·min^{-1} (b)				
1	19.75	5.64	29.40	45.21
2	18.06	6.28	28.79	46.87
3	19.93	7.22	28.74	44.12
4	23.43	4.80	25.18	46.60
5	16.75	8.78	27.48	46.99

within 8–10 nm. Certain differences in the crystalline structure of alternating layers (sodium chloride and iron) are due to the condensation features and are in accordance with the main regularities of direct electron beam evaporation of inorganic substances with subsequent condensation of the vapour flow at substrate temperature $T_s < 0.3T_m$ (T_m is the melting temperature), where condensates have an amorphous or nanosized structure [11].
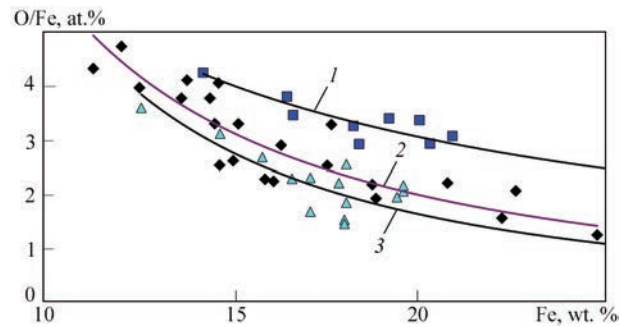
So, at $V_s = 20$ rpm·min^{-1} (Figure 3, b) the composite layering is preserved, but the intensity of reduction of the thickness of iron-enriched metal layers is more pronounced, compared with thicknesses of NaCl-enriched layers. More over, in metal layers h_{Fe} in the area of crossing the joint crystallite boundaries additional opening of the channels along intercrystalline

Figure 4. O/Fe ratio in NaCl–Fe composites produced on rotating substrate at V_s, rpm·min^{-1}: 1 — 2; 2 — 20; 3 — 25 depending on Fe content

boundaries is observed across the composite thickness. Presence of porosity in h_{Fe} layers stimulates this mechanism. At increase of substrate rotation speed, as a result of thinning of iron-enriched layers, the intensity of channel formation across the layer thickness is increased, leading to their fracture.

Investigations of element content on the transverse chip of NaCl–Fe composite showed a large amount of oxygen, adsorbed by Fe nanoparticles from the air, after depressurizing the vacuum chamber (Table 2). Here, the average percentage of oxygen decreases from 16.2 to 6.5 wt.% at increase of substrate rotation speed from 2 to 25 rpm^{-1}.

The value of the ratio of atomic fraction of oxygen to atomic fraction of iron depends on the quantity of iron, and decreases with increase of its content in NaCl–Fe composite (Figure 4). Lowering of the ratio of atomic percentage of oxygen to that of iron, depending on increase of the rotating substrate speed is attributable to reduction of average percent of oxygen in NaCl–Fe composites.

Indeed, the high adsorption capacity for oxygen is inherent in smaller nanoparticles, and the size of iron particles decreases with increase of iron content in the composite, leading to increase of the total area of nanoparticle surface, which results in decrease of the value of the ratio of atomic fraction of oxygen to that of iron.

Table 3. Influence of Fe content on phase characteristics of initial NaCl–Fe composites, stored in air and placed into containers with alcohol

Fe, wt.%	Air				Alcohol			
	Fe_3O_4		NaCl		Fe_3O_4		NaCl	
	$D_{av.\,cr}$, nm	F_{cr}, wt.%	$D_{av.\,cr}$, nm	F_{cr}, wt.%	$D_{av.\,cr}$, nm	F_{cr}, wt.%	$D_{av.\,cr}$, nm	F_{cr}, wt.%
14	–	~ 1	30	99	15	5	95	95
15	7	3	27	97	14	12	50	88
17	8	4	40	96	13	6	58	94
19	»	»	30	»	–	–	–	–
20	»	5	45	94	13	12	60	88
23	5	»	30	95	»	10	55	90
24	6	8	»	92	14	12	50	88
25	»	6	28	94	»	7	65	93

Note. $D_{av.\,cr}$ — average crystallite size, F_{cr} — crystalline phase content.

Metal phase content in NaCl–Fe composites was varied from 16 up to 25 wt.%. X-ray phase analysis (Table 3) showed that iron nanoparticles are present in the form of Fe_3O_4 in sodium chloride matrix. Oxidation of iron nanoparticles to Fe_3O_4 occurs at depressurizing of the vacuum chamber during composite separation from the rotating substrate, resulting in violation of the composite integrity and acceleration of the reaction of oxidation of the open surface of iron nanoparticles by oxygen in porous NaCl matrix. At interaction of iron nanoparticles with oxygen from the air an exothermal reaction with heat evolution takes place. In some cases, the temperature of condensate plates separated from the substrate exceeds 100 °C. Therefore, in order to preserve a stable state of the composite at separation from the substrate, fractures of NaCl–Fe composites were directly placed into a container with alcohol.
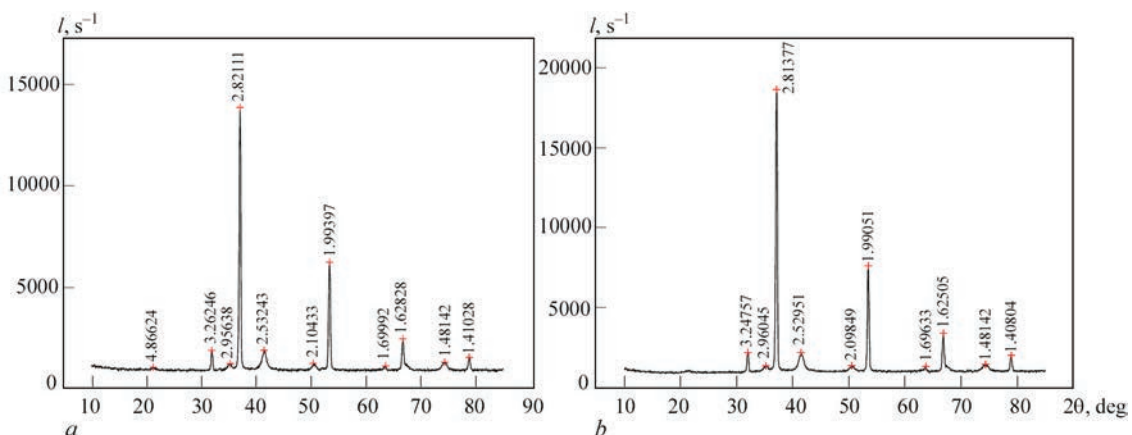
Phase composition and average crystallite size of (Sherrer equations) of initial NaCl–Fe composites, stored in air and in alcohol, are given in Table 3.

In samples of NaCl-14 wt.%Fe composite, stored in air, XRD records reflexes only from NaCl. It is obvious that the dimension of iron oxide phase particles (~ 1 wt.% Fe content in the composite) is beyond the
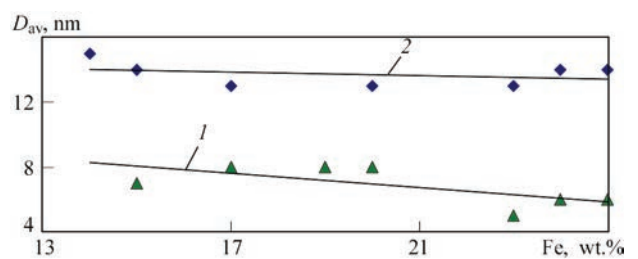
Figure 5. Dependence of average size of Fe_3O_4 crystallites on Fe content in NaCl–Fe composites, produced in air (*1*) and in alcohol (*2*)

limits of sensitivity of this method. Increase of the amount of iron leads to appearance of Fe_3O_4 oxide with average crystallite size (D_{av}) equal to 5–9 nm. Here, with increase of the content of crystalline phase F_{cr} the average size of crystallites (D_{av}) becomes smaller (Figure 5). Reduction of particle size leads to an increase in the role of surface energy and points to a high adsorption ability of small nanoparticles [11].

At formation of Fe_3O_4 nanoparticles in alcohol, their size practically does not change ($D_{av} = 13 \pm 1$ nm) depending on Fe content from 14 to 25 wt.% (Figure 5). Increase of average size of Fe_3O_4 nanoparticles in alcohol is probably related to better protecting properties of alcohol at the stage of oxygen sorption, but this requires further studies.

Figure 6. X-Ray diffraction patterns of NaCl–Fe composite powders: *a* — 25; *b* — 17 wt.% Fe

45

Table 4. Phase composition of NaCl–Fe composites

Sample	Fe, wt.%	Phase composition	Average crystallite size, nm	Crystalline phase content, wt.%
1	17	NaCl JCPDS # 75-306	68	94
		Fe_3O_4 JCPDS # 88-315	13	6
2	25	NaCl JCPDS # 75-306	65	93
		Fe_3O_4 JCPDS # 88-315	14	7

Samples of Fe_3O_4–NaCl–H_2O colloid systems (CS) with iron content of 17 to 25 wt.% were studied in the work. In keeping with X-ray data, the samples were single-phase Fe_3O_4. Material dispersion was determined by X-ray diffraction methods (XRD) and dynamic light scattering (DLS). Figure 6 and Table 4 show the results of analysis, performed by X-ray diffraction method.

In keeping with the calculations, the size of Fe_3O_4 oxide crystallites in the studied powders was in the range of 13–14 nm (Table 4).

Data presented in Figure 7 and in Table 5 show that heating of the studied samples up to the temperature of 80 °C leads to stabilization of powder dispersion. For each of the samples, a monomodal distribution with a maximum in the range of 106.3–115.6 nm (for different compositions) and 60.5 nm for a sample washed from salt (not given in the paper) is in place. A large value of distribution width (PdI ≥ 0.252) is indicative of presence of agglomerates of particles of different size in the dispersion. Maximum part of the particles is represented by 90 and 170 nm fractions, and the size of the smallest particles is close to 40 nm.

In the studied CS the value, corresponding to the distribution maximum (Table 5) can be regarded as characteristic average value of particle size. These values are higher than the average size of the crystallites determined by X-ray diffraction method. It means that the studied samples contained aggregates, which do not break down at heating to 80 °C.

Data given in Table 6 show that for dispersions of CS samples at temperatures of 25 and 80 °C the parameters of average particle size (Z-average) and distribution width (PdI) had high values and scatter that characterizes the samples as polydispersed with presence of aggregates.

NaCl–20 wt.% Fe composite, produced at substrate rotation with maximum speed of 25 rpm·min⁻¹, was selected to study the kinetic characteristics, as the condensate with maximum possible uniform distribution of iron across its thickness and optimum iron content (up to 20 wt.%) [8]. X-ray phase analysis of
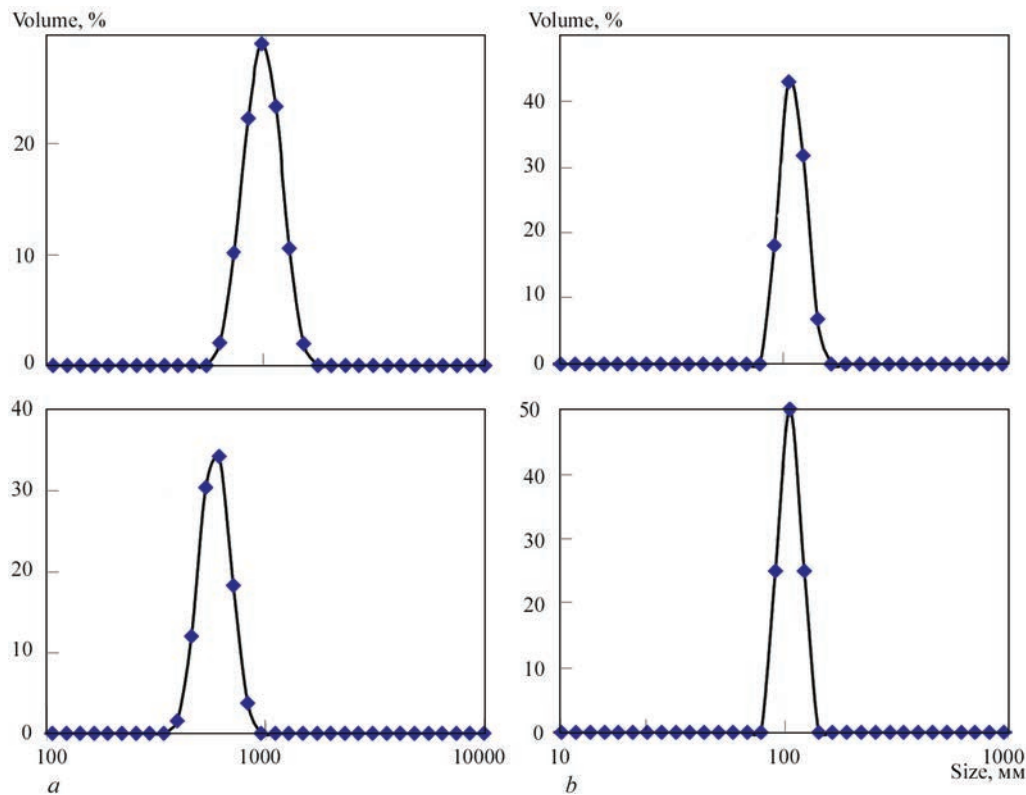
Figure 7. Particle size distribution (abscissa is given by the logarithmic scale) of NaCl–Fe composite powders at measurement temperature, °C: *a* — 25; *b* — 80, samples 1 and 2

Table 5. Average size of CSA* measured by XRD method, and of particles measured by DLS method, for NaCl–Fe powders

Sample	Fe, wt.%	DLS (maximum of particle size distribution, nm)		XRD (CSA size, nm)
		T, °C		
		25	80	
1	17	796.5	110.9	13
2	25	593.2	106.3	14
*Coherent scatter area.				

Table 6. Estimated values of the quality of dispersion of NaCl–Fe powders

Sample	Fe, wt.%	T, °C			
		25		80	
		Z-average	PdI	Z-average	PdI
1	17	894.1	0.889	2893	1.000
2	25	1182	0.663	2578	»

Table 7. X-Ray phase analysis of NaCl–20 wt.% composites after storing in air and in alcohol for 30 days

Phase	Fe_3O_4		NaCl	
Dimension	nm	%	nm	%
Air	10	3	30	97
Alcohol	13	12	60	88

the initial NaCl–20 wt.% Fe composites after storage in air and in alcohol for 3-days is indicative of the presence of Fe_3O_4 phase with 8 and 13 nm nanoparticles in them (Table 7).

Figure 8, *a* shows kinetic curves of the initial sample, stored in air for a day (curve *1*) and in alcohol (curve *2*). Sample, stored in air (Figure 8, *a*, curve *1*) is characterized by 4.5 % reduction in mass at heating to 430 °C [12], that is attributable to desorption of adsorbed moisture (differential curve *1*, Figure 8, *b*). Further increase of temperature to 650 °C is accompanied by increase of sample mass due to additional oxidation of Fe_3O_4 phase to Fe_2O_3 [13]. The sample stored in alcohol (Figure 8, *a,* curve *2*) is characterized by 3 % reduction of mass at heating to 650 °C, that is also attributable to desorption of adsorbed moisture (differential curve *2*, Figure 8, *b*). However, a smaller percentage of sample mass decrease can be accounted for by better protective properties of alcohol at the stage of moisture sorption. It is possible that storing in alcohol prevented the start of additional oxidation of Fe_3O_4 to Fe_2O_3 (12 % of Fe_3O_4 phase instead of 3 %, Table 7), and formation of a more stable Fe_3O_4, although it still requires additional studies.
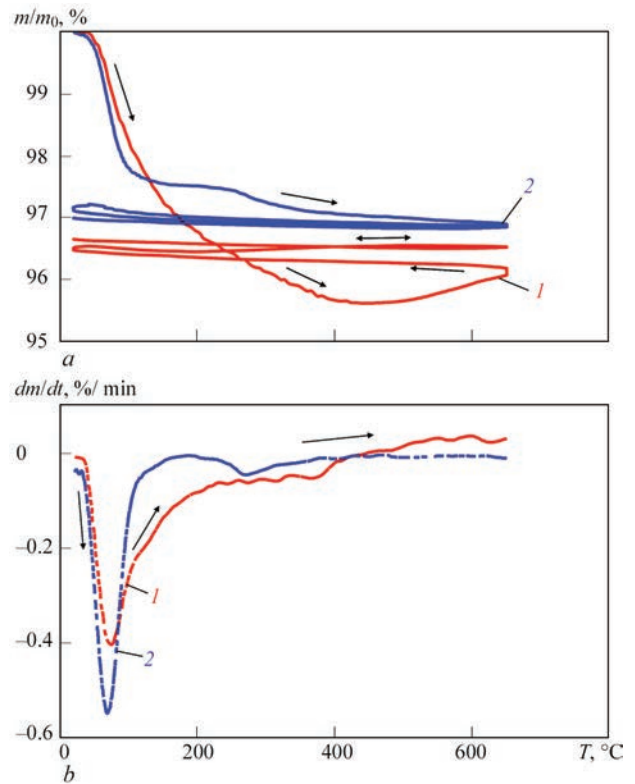
Figure 8. Thermogravimetric analysis (*a*) and differential thermogravimetric (*b*) analysis in air of NaCl–20wt.% Fe composites after storing for 24 h in air (*1*) and in alcohol (*2*)

Assessment of magnetic characteristics showed that the sample stored in alcohol (with greater mass of Fe_3O_4), has better magnetic properties.

CONCLUSIONS

1. NaCl–Fe composites, produced by the procedure with arrangement of evaporation material sources peripheral relative to the substrate rotation axis, have a layered structure.

2. The total thickness of the layers depends on substrate rotation speed and is equal to 3.89 to 0.55 μm for V_s = 2 and 25 rpm·min^{-1}, respectively.

3. The ratio of the thickness of layers enriched in iron and sodium chloride, remains constant and is equal to approximately 0.2, irrespective of the substrate rotation speed; thickness of Fe- and NaCl-enriched layers in an isolated composite for V_s = 25 rpm. min^{-1} is equal to h_{Fe} = 0.09 and h_{NaCl} = 0.46 μm, respectively.

4. It was found that oxidation of iron nanoparticles to Fe_3O_4 oxide occurs at depressurizing of the vacuum chamber during the condensate separation from the substrate.

5. Average size of Fe_3O_4 crystallites, depending on Fe content in NaCl–Fe condensate, is determined by the method of its storage: in air or in alcohol. In 14 to 25 wt.% range of iron concentration the average size

of Fe_3O_4 particles, stored in air is 5–10, and in alcohol — 13 ± 1 nm.

6. It was found that nanoparticles, produced in NaCl–17–24 % Fe composites, have a monomodal distribution with a maximum in the range of 106.3–115.6 nm. Minimum size of the nanoparticles is equal to 40 nm.

7. Investigations on the transverse chip of the composite confirmed the presence of oxygen, adsorbed by Fe nanoparticles from the air. Depending on substrate rotation speed, the average percentage of oxygen decreases from 16.2 to 6.5 wt.% at V_s increase from 2 to 25 rpm·min^{-1}, respectively.

8. Value of the ratio of atomic fraction of oxygen to atomic fraction of iron depends on the amount of iron, decreases with increase of its content in NaCl–Fe composite and increase of substrate rotation speed.

9. Storing NaCl–Fe composites in alcohol protects them from saturation by moisture and iron oxidation, and, consequently, leads to more stable physical properties in time.

REFERENCES

1. Salata, O.V. (2004) Applications of nanoparticles in biology and medicine. *J. of Nanotechnology*, **2**, 3–8. http://www.na-nobiotechnology.com/content/2/1/3

2. Movchan, B.A., Kurapov, Yu.A., Didikin, G.G. et al. (2011) Regulation of composition and structure of Fe–O system nanoparticles in electron beam evaporation of Fe_3O_4. *Porosh-kovaya Metallurgiya*, 50(**3–4**), (478), 56–63 [in Russian]. doi.org/10.1007/s11106-011-9314-0.

3. Kurapov, Yu.A., Litvin, S.E., Romanenko, S.M. (2013) Structure and thermal stability of Ti–NaCl condensates deposited from the vapour phase in vacuum. *Nanostructured Materials Sci.*, **1**, 55–62. http://www.materials.kiev.ua/science/edition_view.jsp?id=2

4. Kurapov, Yu.A., Litvin, S.E., Didikin, G.G., Romanenko, S.M. (2011) Structure of two-phase condensates Cu–NaCl deposited from vapor phase in vacuum. *Sovrem. Elektrome-tall.*, **2**, 19–22 [in Russian]. https://patonpublishinghouse.com/eng/journals/sem/2011/02/05

5. Kurapov, Yu.A., Romanenko, S.M., Didikin, G.G., Oranska-ya, E.I. (2017) Controllable synthesis of iron oxide nanoparticles in porous NaCl matrix. *Materials Research Express*, 4(**3**), 035031. doi.org/10.1097/01.rli.0000221321.90261.09

6. Paton, B.E., Movchan, B.O., Kurapov, Yu.A., Yakovchuk, K.Yu. (2010) *Method of producing of metal-oxygen system nanoparticles with specified composition by electron beam evaporation and condensation in vacuum.* Pat. 92556, Ukraine [in Ukrainian]. http://base.ukrpatent.org/searchINV/search.php?action=viewdetails&IdClaim=151646

7. Grechanyuk, M.I., Osokin, V.O., Afanasiev, I.B. et al. (2002) *Method of producing of porous materials*. Pat. 46855, Ukraine [in Ukrainian].

8. Grechanyuk, N.I., Osokin, V.A., Grechanyuk, I. N. et al. (2006) Composite materials on base of copper and molybde-num condensed from vapor phase, for electric contacts. Pt 2: Fundamentals of electron beam technology for producing materials for electric contacts. *Advances in Electrometallurgy*, **2**, 8–17.

9. Osokin, V.O., Kurapov, Yu.A., Boretsky, V.V. et al. (2021) Producing of Fe, Cu, Ag nanoparticles in NaCl matrix on rotating substrate by EB-PVD method. In: *Abstr. of Pap. of Int. Conf. on Modern Technologies of Joining of Materials.* Ed. by L.M. Lobanov. Kyiv, IAW [in Russian]. https://patonpublish-inghouse.com/proceedings/stzm2021.pdf

10. Movchan, B.A. (2006) Inorganic materials and coating produced by EBPVD. *Surf. Eng.*, **22**, 35–46.

11. Movchan, B.A., Demchishin, A.V. (1969) Study of structure and properties of thick vacuum condensates of nickel, titanium, tungsten, aluminium oxide and zirconium dioxide. *Fizika Metallov i Metallovedenie*, 28(**4**), 653–660 [in Russian].

12. Kurapov, Y.A., Vazhnichaya, E.M., Litvin, S.E. et al. (2019) Physical synthesis of iron oxide nanoparticles and their biological activity in vivo. *SN Applied Sci.*, 1(**1**), 1–102. https://doi.org/10.1007/s42452-018-0110-z

13. Kurapov, Yu.A., Movchan, B.A., Litvin, S.E. et al. (2011) Effect of iron concentration on the adsorptive capacity of iron oxide nanoparticles in the porous NaCl matrix in relation to atmospheric oxygen. *Advances in Electrometallurgy*, 9(**1**), 29–32. http://pwi-scientists.com/pdf/journals/aiem201101.pdf

ORCID

Yu.A. Kurapov: 0000-0003-3460-1712,
V.O. Osokin: 0000-0002-0632-7739,
S.E. Lytvyn: 0000-0001-6113-5038

CONFLICT OF INTEREST

The Authors declare no conflict of interest

CORRESPONDING AUTHOR

V.O. Osokin
E.O. Paton Electric Welding Institute of the NASU
11 Kazymyr Malevych Str., 03150, Kyiv, Ukraine
E-mail: 4osokin@gmail.com

SUGGESTED CITATION

JOURNAL HOME PAGE

https://pwj.com.ua/en

NON-DESTRUCTIVE TESTING OF ELEMENTS OF TITANIUM HONEYCOMB PANELS BY SHEAROGRAPHY METHOD USING VACUUM LOAD

L.M. Lobanov, V.V. Savytskyi, I.V. Kyianets, O.P. Shutkevich, K.V. Shyian

E.O. Paton Electric Welding Institute of the NASU
11 Kazymyr Malevych Str., 03150, Kyiv, Ukraine

ABSTRACT

The use of the modern method of non-destructive quality testing — electron shearography in combination with vacuum load for the study of elements of titanium honeycomb panels is considered. The effectiveness of the procedure for detecting inner defects of different location in the honeycomb panels, size and configuration is shown.

KEY WORDS: non-destructive quality testing, honeycomb panels, electron shearography, vacuum load

INTRODUCTION

Manufacture of modern products and structures, characterized by high quality and reliability, is associated with the use of new structural materials with set physical and mechanical properties. They mostly operate in the conditions of a complex mechanical load and temperature gradients. At the same time, even a slight concentration of stresses, that occurs in the zone of defects of structural elements, may lead to loss of their serviceability.

Providing high quality of created structures is one of the most important scientific and technical problems. In this regard, it is important to improve the well-known and develop new modern automated methods and means of quality testing of mechanisms and structures.

At present, in order to detect defects in materials and structures, a group of non-destructive methods is used, that include: radiological, acoustic, luminescent, method of eddy currents, etc. [1, 2]. Each of these methods has its own disadvantages and advantages, but none of them is universal and does not satisfy all the requirements for means and methods of non-destructive testing.

The group of the abovementioned testing methods successfully complement the methods of laser interferometry, especially speckle-interferometry. For engineering applications, the method of shear speckle-interferometry (shearography) is perspective [3, 4]. This method allows directly obtaining the value of derivatives from displacements and is effective in the analysis of deformations. The shearography method is not sensitive to displacement of the object as a whole, since such a displacement does not cause deformation and also does not require special protection against vibrations.

An intense development of computer and computational technology allowed a substantial improvement of the shearography method and development of the method of digital shearography [5–10]. An important characteristic feature of the method of digital shearography is the fact, that it allows observing a dynamic pattern of interference fringes in a real-time mode. The relative simplicity of this method allows applying it to solve significantly more complex problems associated with the analysis of deformations and quality testing of structures in laboratory and industrial conditions.

At present, digital shearography is intensively developing and has such advantages as visualization, contactlessness, high sensitivity, possibility of performing studies of objects of a complex shape and significant sizes in a real-time mode. In addition, an important advantage, as was mentioned above, is insensitivity to vibrations.

SHEAROGRAPHY SYSTEM FOR NON-DESTRUCTIVE QUALITY TESTING

Shearography quality testing is based on registration of difference during deformation while loading a defect-free element and an area with a defect, since in the defect zone, a decrease in rigidity is typical.

At the E.O. Paton Electric Welding Institute (PWI), an automated shearography system based on a modified Michelson interferometer with a variable inclination angle of the mirror in one of the optical arms was developed. The block-diagram of this system for non-destructive quality testing is shown in Figure 1.

Shearographic system (Figure 2) includes the following main components: laser illumination system (*1*, *2*), lens (*3*), interferometer (*4*), digital camera (*12*), laptop or computer with monitor (*13*), phase-shifting
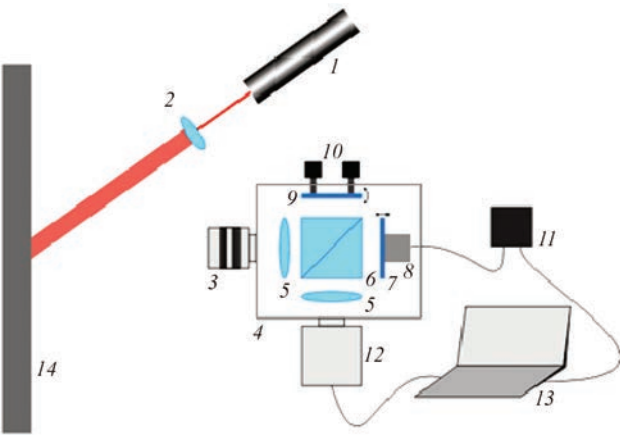
Figure 1. Block-diagram of shearography system: *1* — source of coherent radiation; *2* — laser beam expanding device; *3* — lens; *4* — shearography interferometer, which includes lenses *5*, dividing cube *6*, mirror *7*, fixed on piezoelement *8*, mirror *9*, which creates displacement of image using screws *10*; *11* — controller for piezoelement control *8*; *12* — digital camera; *13* — laptop; *14* — investigated specimen

system (*7*, *8*, *11*). The piezoelectric phase-shifting element with the power source provides the required phase shift between the two wavefronts as a result of the mirror displacement in one of the optical arms of the interferometer to the value $\lambda/2$, λ, $3\lambda/2$, where λ is the length of the laser radiation wave. Shearography mirror *9* serves to create a shear. Varying the inclination angle of the mirror in the interferometer with the use of screws *10*, it is possible to set the required displacement value. In this case, the value of a shear affects the sensitivity of the measurement of the testing system. The laser is intended to illuminate the objects of investigations and the formation of speckle-structure on it. The replaceable lens *3*, mounted on the shear-module *4*, allows receiving and focusing the obtained speckle-patterns on the array of a digital camera *12* for their further digital processing. Replacing lenses, it is possible to adjust interferometer for studying regions of objects with a different area.

Figure 2. Appearance of shearography interferometer with laser modules

Studying the quality of objects requires specifying exactly what kind of surface deformations is better for registration — plane or out-of-plane, since different types of loading the specimen used in the process of shearography control causes different types of deformation. For example, during the use of thermal load or inner pressure, in the object out-of-plane deformations of its surface, and in the case of mechanical tension — plane deformations occur.

To obtain the sensitivity of the interferometer to different types of deformation (in the plane or out-of-plane) is possible by changing the mutual location of an object, illuminating laser radiation and observation direction through the interferometer lens. In order to achieve the maximum sensitivity of the optical scheme of the interferometer to out-of-plane deformation, it is necessary that the angle between the directions of illumination and observation was minimal. Therefore, lasers are fixed directly on the shearography interferometer.

The developed automated shearography system operates according to the following algorithm. A wave front from the laser, reflected from the surface of the investigated object, passes through the interferometer and focuses on the array of a digital camera, by means of which it is transmitted to the computer for further digital processing. Then the object is loaded (as a result of which it is deformed) and again the image of the studied surface is recorded. The images obtained before and after the load are processed before obtaining a shearogram with the use of the software developed by the PWI. Such a shearogram represents a pattern of alternating light and dark areas (fringes) that requires a further processing, namely, reducing the level of speckle-noise, intensifying contrast of fringes and some other. The software allows building a phase distribution field and a three-dimensional image of the deformation surface of the tested object, as well as recording the results in the form of documents.

The parameters of computer processing, except for standard operations (obtaining interference patterns, filtration and stitching) include additional filtration, since the pattern of interference fringes may be "noisy" and insufficiently contrasting. Too large number of interference fringes leads to a decrease in image contrast, which increases the time and reduces the efficiency of computer processing. A number of interference fringes is selected for a rapid and efficient processing of a shearogram. The change in a number of interference fringes is also possible by adjusting the value of the shear, i.e., by the change in the sensitivity of the interferometer.

Non-destructive quality testing of the elements of titanium honeycomb panels was carried out using

the developed software, which allowed obtaining the interference fringe patterns of tested objects, filtering the received images, building phase fields and a three-dimensional representation of deformation surface of an object and recording the results into the file.

The developed software is used: to enter speckle-images from the digital camera to the computer; control the voltage supply on the piezoelement placed in one of the arms of the shearography interferometer; elaborate the shearography speckle-images for calculation and a three-dimensional visualization of the fields of the surface deformation of investigated objects; construction of diagrams of change in derivatives in a set direction along the selected cross-sections; storage of obtained results in the form of a file; outputting of shearography testing results to the printing device.

CHOICE OF OPTIMAL LOAD

In order to obtain a shearogram, it is necessary to record a reflected light wave in two states of an investigated object — in the initial and loaded one. Therefore, it is important to choose a method of loading, since the effectiveness and reliability of shearography control depends on it. The concept of an optimal loading of an object at shearography non-destructive testing consists in choosing such method of loading, which would allow causing stress concentration in the zone of a probable defect. In this case, researchers are trying to create such a stressed state that causes the largest difference in the distribution of deformation along the surface of a studied object on defective and defective-free areas.

The optimal value of load is selected depending on mechanical properties of the material from which a studied object is manufactured. For example, if an object is made of the polymer material, the load temperature should not cause plastic deformation. In the process of shearography quality testing in most cases it is enough to create a small (several degrees) difference between the temperature of a studied object before and after heating.

During the use of mechanical load, pressure or vacuum, for all types of materials, the value of the load is selected in such a way that caused deformations remained elastic and did not reach the yield strength of the material. Usually a method of load and its parameters are selected experimentally.

NON-DESTRUCTIVE QUALITY TESTING OF HONEYCOMB PANELS

During the manufacture of modern structures of aerospace engineering, honeycomb panels (Figure 3) are widely used, which provides a significant reduction in the weight of products. Such panels consist of two outer skins, between which a honeycomb filler is located. In its turn, the filler is joined with outer sheets using welding, brazing or adhesion. Outer sheets can be manufactured both from metals and plastics or composites. A honeycomb structure has a high rigidity during bending and strength. Defects of a honeycomb structure, which reduce the strength during bending and compression strength include damages to the filler, surface defects, lack of continuity and incorrectly formed joint.

To use vacuum load during shearography non-destructive quality testing of honeycomb panels at the PWI, the equipment was designed consisting of a vacuum detachable chamber, compressor, by means of which vacuum is created, and pressure regulator in the chamber (Figure 4). The sizes of a vacuum detachable chamber can be changed according to the desired sizes and curvature of an investigated area of structural elements. An investigated area of the specimen is loaded uniformly, the process of experiments is automated and takes up to 2 min.

The elements of honeycomb panels, in which defects were detected by the shearography method, were made of titanium alloy. The panel skin had a thickness of 1 mm, the thickness of the sheet, from which the filler was made, amounted to 0.5 mm, and the diam-
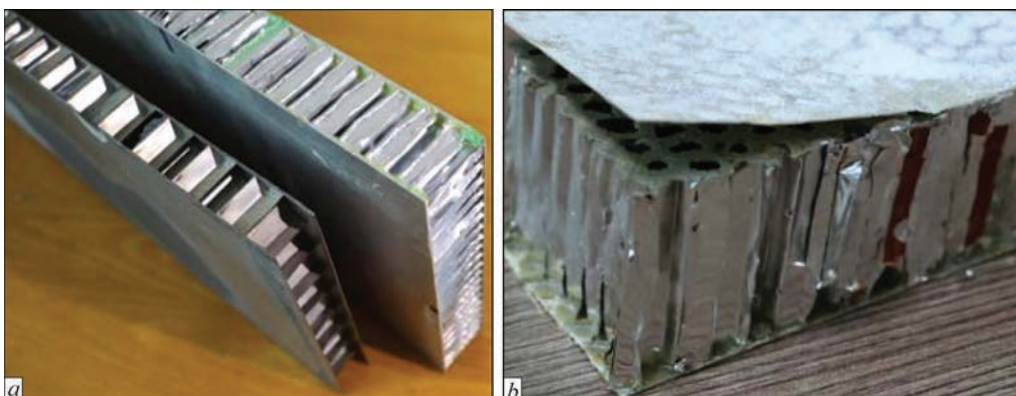
Figure 3. Appearance of honeycomb panels: *a* — brazed-adhesive of aluminium and titanium alloys; *b* — destroyed panel

Figure 4. Appearance of vacuum detachable chamber (*1*) and compressor (*2*)

eter of the honeycomb cell was 6 mm. The skin and filler were joined with each other by brazing. During such a method of joining, adjacent edges are sometimes in a state of adhesion, which leads to arising of defective zones in the form of lack of brazing. In the conditions of static or dynamic loads, on the area of such a defect, an opening of edges occurs that can lead to destruction of assembles and structural elements in the process of their operation.

During tests of elements of titanium honeycomb panels, vacuum load was used, which, unlike the thermal method, allows providing a uniform and automated load of the entire investigated area of the specimen, as well as reduction in the time for diagnostics. During the experiment, a special chamber was applied to the surface of the investigated area and a vacuum of up to 0.7 atm was created and the initial state of the surface (speckle-pattern of the surface of the studied panel was recorded). Then, pressure in the chamber

was reduced or increased by the value of 0.1–0.3 atm and the state of the honeycomb panel was recorded after loading. A reduction or increase in pressure caused a surface deformation, which allowed revealing and visualizing the deformation of each honeycomb cell. In the areas, where bonds between honeycombs are weakened (presence of a crack, absence of a welded joint, etc.), or other types of surface defects are present, a local abnormal deformation of the surface of studied elements appears.

During testing elements of honeycomb panels, a shear in the interferometer along a horizontal, vertical and diagonal directions was used. A shear determines the direction of optical differentiation of values of shears of the investigated surface and allows obtaining parameters of its deformation that arose under the action of applied load.

Figure 5 shows the results of shearography testing of the element of the titanium honeycomb panel using vacuum load and a shear in a diagonal direction. The images show a visualized honeycomb filler with approximately the same periodicity of change in defromation amplitude and a local defective area was determined, where violation of this periodicity in the form of "dumbbell" (indicated by arrows) is present, which characterizes the absence of a joint between the skin and filler.

The use of a shear in a vertical direction also allows visualizing the honeycomb filler and determining the defective local area (Figure 6). However, in this case, anomalous zones are manifested
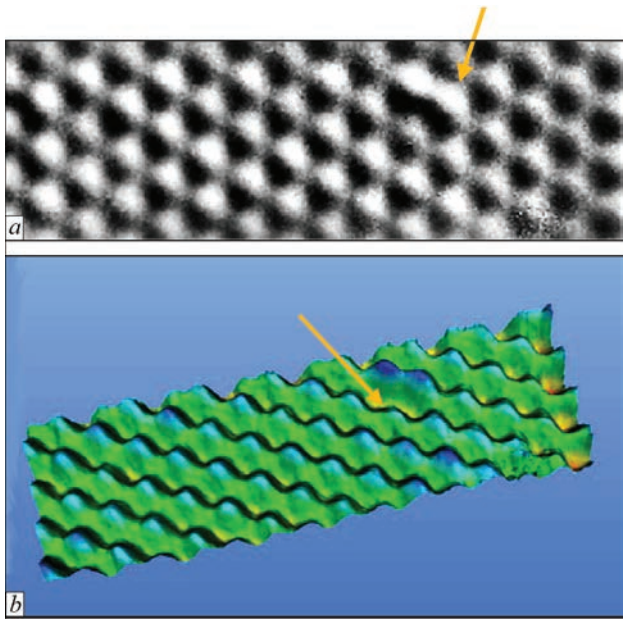
Figure 5. Quality testing of honeycomb panel element manufactured of titanium alloy, under vacuum load when using shear in a diagonal direction: *a* — shearogram of the investigated area; *b* — three-dimensional image of deformation of the investigated area
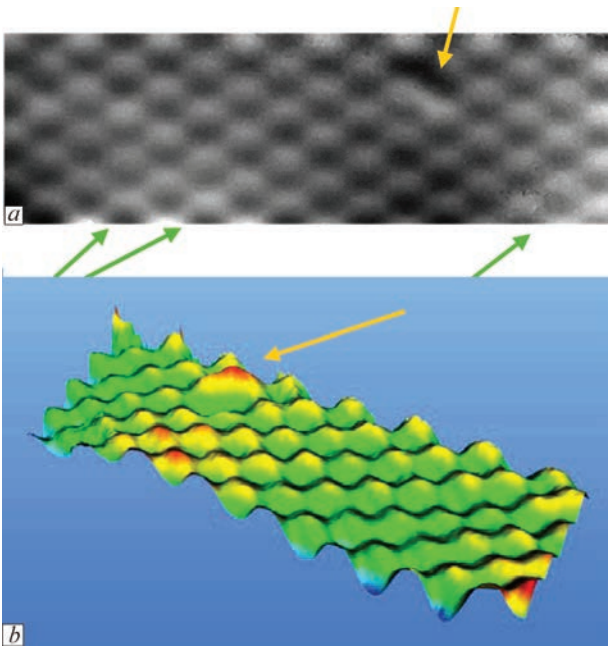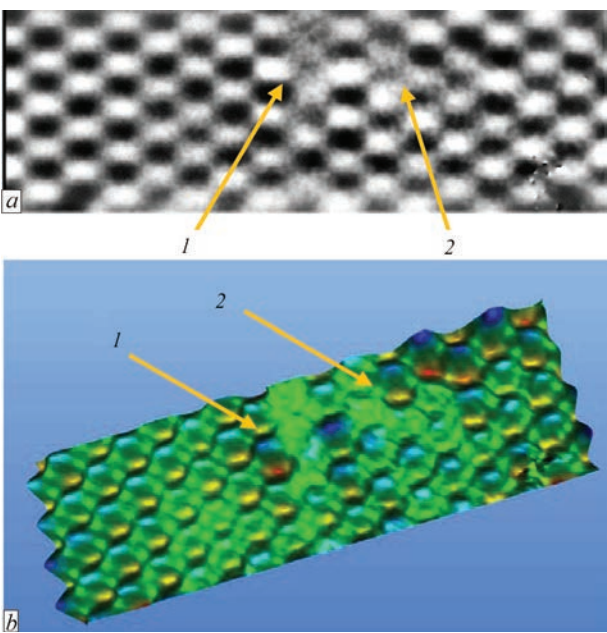

Figure 6. Quality testing of honeycomb panel element under vacuum load when using shear in a vertical direction: *a* — shearogram of the investigated area; *b* — three-dimensional image of deformation of the investigated area
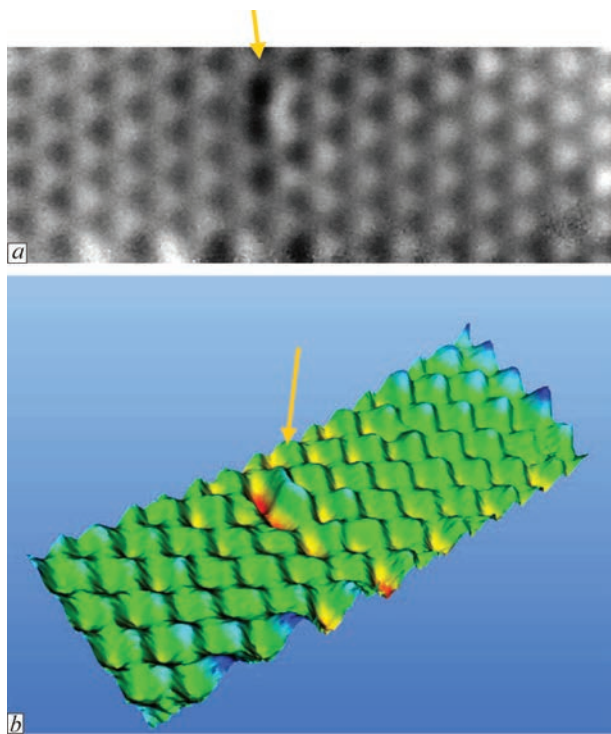
Figure 7. Quality testing of honeycomb panel element under vacuum load: shearogram (*a*) and a three-dimensional image of deformation of the investigated area (*b*) when using shear in a horizontal direction
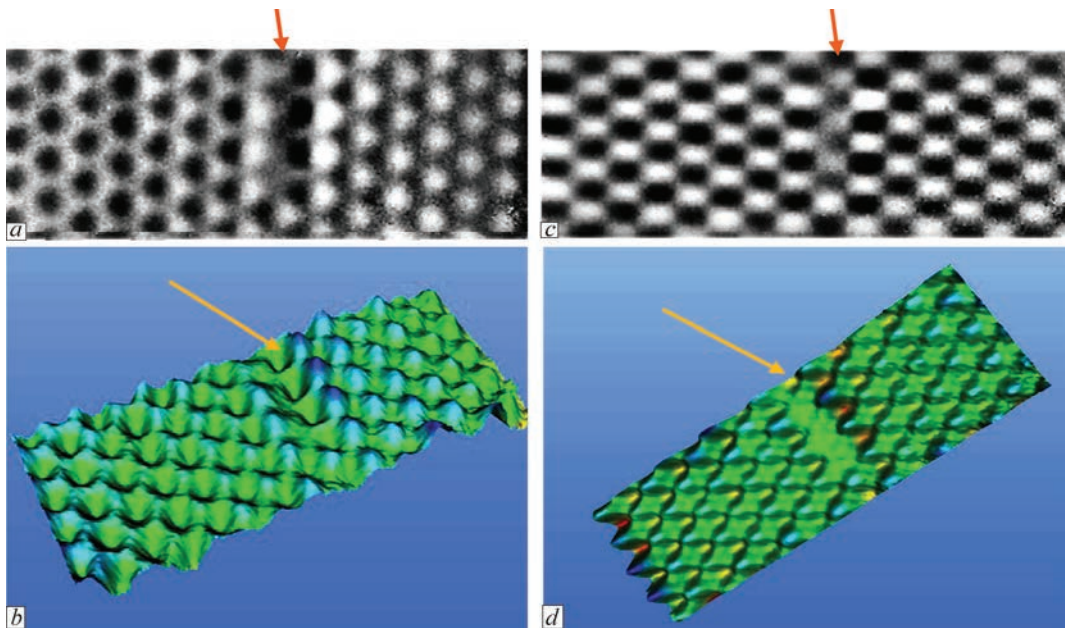

Figure 9. Quality testing of honeycomb panel element under vacuum load when using a shear in a vertical direction: shearogram (*a*) and a three-dimensional image of deformation (*b*) of the investigated area

along the edges of the surface of the honeycomb element, which is associated with the boundary effect of loading the vacuum chamber (indicated by green arrows in Figure 6, *a*).

Figure 7 shows the results of non-destructive quality testing of the honeycomb panel element by the shearography method using vacuum load and a shear in a horizontal direction. The local defective zone in the form of a "vertical dumbbell", indicated by ar-

rows, is clearly seen on the background of a visualized honeycomb filler.

The results of shearography control of defective areas, including more than two honeycomb cells, are shown in Figures 8, 9. On the images, local zones of the abnormal deformation of the studied surface on the background of a visualized honeycomb filler are visible, which makes it possible to evaluate the number of damaged honeycomb cells.

In Figure 8, *a* significantly reduced deformation amplitude along four vertically placed cells is observed. Such detection of features is usually asso-

Figure 8. Quality testing of honeycomb panel element under vacuum load: shearogram and a three-dimensional image of deformation of the investigated area using shear in a horizontal (*a*, *b*) and vertical (*c*, *d*) direction

ciated with a higher rigidity of the local area of the specimen as compared to other areas. This defective zone is well visualized both in horizontal as well as in vertical direction of a shear.

Figure 9 shows the results of testing another area of the element of a honeycomb panel, where except of a vertical defective zone *1*, a defective zone *2* is present, which is indicated by a decrease in the amplitude of deformation of a larger area of the studied surface.

The use of a vacuum cover plate allows preserving the same conditions during experiments, which increases the repeatability of the obtained results and increases their reliability unlike a widely used thermal load, which requires testing of ambient temperature and heating and cooling time.

The obtained results showed that a defective zone is revealed the most clearly in the case when its area is less than 20 % from the total area of the tested area of the studied element surface.

CONCLUSIONS

The method of electronic shearography in combination with vacuum load is effective to detect inner defects of different sizes and configuration in the elements of honeycomb panels.

The created shearography equipment and vacuum load allowed increasing the efficiency of investigations by automizing experiments and reducing the time required to conduct them. The use of vacuum load allowed improving the repeatability of obtained results and increasing their reliability.

REFERENCES

1. (2001) *Non-destructive testing and technical diagnostics*. Ed. by Z.T. Nazarchuk. Lviv, PMI [in Ukrainian].
2. (2000) *Trends in optical non-destructive testing and inspection.* Ed. by P.K. Rastorgi, D. Inaudi. Oxford, Elsevier Sci. B.V.
3. Lobanov, L.M., Pivtorak, V.A., Oleinik, E.M., Kiyanets, I.V. (2004) Procedure, technology and instrumentation of shearographic non-destructive testing of materials and elements of structures. *Tekh. Diagnost. i Nerazrush. Kontrol*, **3**, 25–28 [in Russian].
4. Hung, Y.Y., Ho, H.P. (2005) Shearography: An optical measurement technique and applications. *Materials Sci. and Eng.*, **R49**, 61–87.
5. Lobanov, L.M., Znova, V.A., Pivtorak V.A., Kiyanets, I.V. (2016) Diagnostics of composite elements of aircraft structures by electron shearography method. *Tekh. Diagnost. i Nerazrush. Kontrol*, **2**, 19–27 [in Russian].
6. Lobanov, L.M., Pivtorak, V.A., Tkachuk, G.I. et al. (2005) Express control of quality and stressed state of welded structures using methods of electron shearography and speckle-interferometry. *The Paton Welding J., 8, 39–44.*
7. Zhao, Q., Dan, X., Sun, F. et al. *(*2018) Digital shearography for NDT: Phase measurement technique and recent developments. *Appl. Sci.*, **8**, 2662.
8. ASTM E2581-14 (2019) *Standard practice for shearography of polymer matrix composites and sandwich core materials in aerospace applications.* ASTM International, West Conshohocken, PA, www.astm.org.
9. Feng, H.J., Zhang, J., Liu, X.K. (2011) Studies on digital shearography for testing of aircraft composite structures and honeycomb-based specimen. *Applied Mechanics and Materials*, **121–126**, (October 2011), 1264–1268. https://doi.org/10.4028/www.scientific.net/amm.121–126.1264.
10. Schuth, M., Buerakov, W., Vössing, F. et al. (2014) Shearographic inspections by an interferoscope. In: *Proc. SPIE 9302, Int. Conf. on Experimental Mechanics, 2014, 93020C (4 March 2015).* https://doi.org/10.1117/12.2080807.

ORCID

L.M. Lobanov: orcid.org/0000-0001-9296-2335

CONFLICT OF INTEREST

The Authors declare no conflict of interest

CORRESPONDING AUTHOR

O.P. Shutkevich
E.O. Paton Electric Welding Institute of the NASU
11 Kazymyr Malevych Str., 03150, Kyiv, Ukraine
E-mail: shutkevich1996@gmail.com

SUGGESTED CITATION

JOURNAL HOME PAGE

https://pwj.com.ua/en
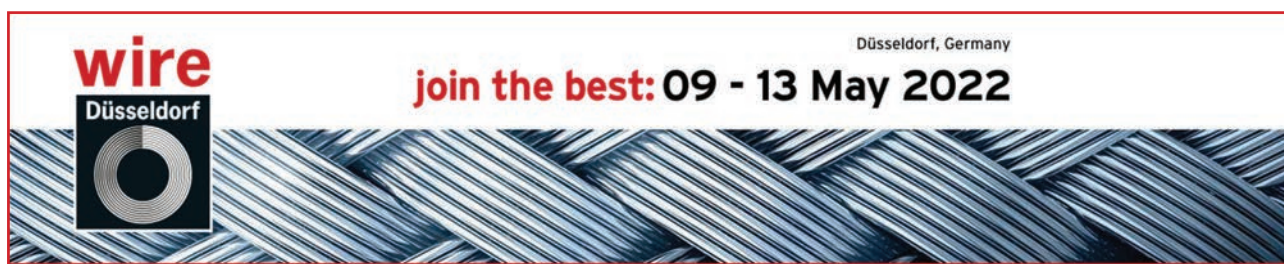
OPENING OF HIGH-RELIEF MEMORIAL BOARD TO ACADEMICIAN B.E. PATON

On November 11, 2021 a solemn opening of high-relief memorial board to academician B.E. Paton, Director of the Institute, President of the National Academy of Sciences of Ukraine took place at the E.O. Paton Electric Welding Institute of the National Academy of Sciences of Ukraine. Employees of PWI, National Academy of Sciences of Ukraine, Kiev enterprises, and media were present in the meeting on the occasion of this event. The meeting was opened by I.V. Krivtsun, academician of the NAS of Ukraine, Director of the Institute.

In his speech I.V. Krivtsun noted that Borys E. Paton is an outstanding Ukrainian scientist in the field of welding, metallurgy and technology of materials, materials science, prominent public figure and talented organizer of scientific research. Together with his father, Evgen O. Paton, he created the world-renowned Paton scientific school. B.E. Paton gained international prestige due to his versatile and extremely fruitful scientific and engineering activity, and desire to direct fundamental research to solving the problems of society.

He had a profound understanding of the role of science in society, its goals and objectives, and successfully combined active scientific and social-political work. Under his leadership Ukrainian science received a new powerful impulse in its development. After disintegration of the Soviet Union and formation of independent Ukraine under the conditions of an acute economic crisis Borys Paton managed to preserve the Academy, its main scientific schools, principles of academic self-management, perform restructuring of the Academy in accordance with the new conditions, and direct fundamental and applied research to solving urgent tasks of creating a young state.

Borys Paton was not only an outstanding scientist and organizer of science, but also an excellent educator and teacher with a capital letter. He brought up a whole galaxy of scientists in the field of welding, metallurgy and materials science. Borys Paton always was democratic, well-wishing, open to communication, ready to help in solving not just the scientific, but urgent social and everyday problems of the staff of the Institute and the Academy.

Borys E. Paton was a true leader, creative personality, highly respectable and kind person, who had fantastic energy and working capacity, and deep

knowledge in many fields. He had a generous nature, keen analytical mind and excellent sense of humour. Bright memory of this outstanding person, talented scientist, organizer of science and public figure will forever remain in our heats.

Academician A.G. Zagorodnyi, President of the National Academy of Sciences of Ukraine, noted that opening of the memorial high-relief board to B.E. Paton is an important event. He was a distinguished scientist and engineer, and outstanding organizer of Ukrainian science. B.E. Paton had two most important things in his life — NAS of Ukraine and PWI, which he cared for as though these were his children. During the period of his leadership, Ukrainian science was developing fruitfully, new institutes opened, and new directions of research emerged. There is fundamental

and applied science, but B.E. Paton is a vivid example of how purpose-oriented research can be developed and how these directions can be united. During the period of his leadership, PWI gained worldwide recognition as a leading scientific center. With this high-relief board opened today B.E. Paton will continue to live in our hearts.

Kind words about Borys Paton were also shared by academician L.M. Lobanov, PWI Deputy Director, V.O. Shapovalov, Corresp. Memb. of NASU, academician K.A. Yushchenko, PWI Department Head, academician V.V. Petrov, Director of the Institute of Information Registration and academician A.G. Naumovets, Head of NASU Commission on perpetuating the memory of academician B.E. Paton.

At the end of the meeting I.V. Krivtsun thanked all those present and emphasized that the memory of B.E. Paton will remain forever in our hearts and the best guarantee for it will be our fruitful work in modern science, following the example of the distinguished scientist.

The author of the high-relief board is V.G. Koren, a well-known sculptor, member of the Union of Artists of Ukraine. The bronze high-relief board was made in the classic style of the traditional portrait genre. The installation in the form of a welding flash symbolizes emergence of new ideas, of which B.E. Paton had a lot. The high-relief board was created with voluntary contributions of PWI employees.

Editorial board